Quantification et réduction d'incertitudes liées à la modélisation de la turbulence dans les écoulements de turbomachines par méthodes multi-modèles bayésiennes

Maximilien de Zordo-Banliat

HESAM UNIVERSITÉ

Arts et Métiers Sciences et Technologies

ÉCOLE DOCTORALE SCIENCES ET MÉTIERS DE L'INGÉNIEUR
[Laboratoire Dynfluid - Campus de Paris]

THÈSE

présentée par : **Maximilien DE ZORDO-BANLIAT**
soutenue le : **17 février 2022**

pour obtenir le grade de : **Docteur d'HESAM Université**

préparée à : **École Nationale Supérieure d'Arts et Métiers**
Spécialité : **Mécanique et Matériaux**

Quantification and reduction of turbulence modeling uncertainties in turbomachinery flows using Bayesian multi-model ensembles

THÈSE dirigée par :
[Mme Paola CINNELLA]

et co-encadrée par :
[M. Xavier MERLE, M. Grégory DERGHAM]

Jury		
M. Jean-Camille CHASSAING	Professeur, Sorbonne Université	Président
M. Richard DWIGHT	Associate Professor, T.U. Delft	Rapporteur
M. Gael POETTE	Ingénieur de recherche HDR, CEA	Rapporteur
M. Heng XIAO	Associate Professor, Virginia Tech	Examinateur
M. Hervé BEZARD	Ingénieur de recherche, ONERA	Invité
Mme. Paola CINNELLA	Professeur, Sorbonne Université	Directrice
M. Xavier MERLE	Maitre de Conférences, ENSAM Paris	Co-encadrant
M. Grégory DERGHAM	Ingénieur de recherche, SAFRAN TECH	Co-encadrant

THÈSE

Remerciements

En premier lieu, je tiens ici à remercier mes encadrants qui m'ont permis de me consacrer à ce sujet en me laissant une grande liberté, évidemment très appréciable. Je voudrais d'abord remercier ma directrice de thèse Paola Cinnella, pour ses précieux conseils et pour avoir su donner les grandes orientations qui ont permis à ce travail d'aboutir. J'aimerais ensuite remercier Xavier Merle pour sa patience et son exigence scientifique sans lesquelles ce travail n'aurait pas eu la même rigueur. Enfin, j'aimerais exprimer ma reconnaissance sincère à Gregory Dergham pour sa disponibilité tout au long de la thèse. Nos réunions étaient toujours riches de pistes ou remarques pertinentes pour la suite et presque trop nombreuses à explorer en une seule thèse. Votre implication à tous les trois ainsi que la confiance que vous m'avez témoignée, ont certainement beaucoup joué dans la réussite de cette thèse. Merci.

Je tiens ensuite à remercier les membres de mon jury, qui ont accepté de relire et de juger ce travail. Merci d'abord à Jean-Camille Chassaing, pour avoir accepté de faire partie de mon comité de suivi de thèse, avant de présider ce jury. Je remercie ensuite Richard Dwight et Gael Poette d'avoir accepté la charge de rapporteur de ce manuscrit, ainsi que d'avoir enrichi notre réflexion par la discussion que nous avons pu avoir ensemble. Merci à Heng Xiao d'avoir permis, par ses remarques pertinentes, d'améliorer la précision de la description de la base de régression utilisée dans le sixième chapitre. Enfin j'aimerais remercier Hervé Bézard pour son intérêt porté tout au long de la thèse, ainsi que pour ses conseils sur le choix d'éventuelles nouvelles features.

Je voudrais maintenant exprimer ma sincère gratitude pour le pôle MS de Safran Tech, et plus particulièrement à l'ensemble de l'équipe CFD, dont l'aide m'a été précieuse dans la maîtrise des outils de calculs et de post-traitement CFD. Merci donc à Emma, David, Alexandre, Dimitri, Michael et Sophie. J'aimerais aussi remercier Sébastien da Veiga pour son aide et son investissement à nos cotés.

J'aimerais bien sûr remercier les membres du laboratoire DynFluid qui m'ont accompagné pendant ces trois années. Nos discussions étaient toujours riches et variées; je crois qu'elles m'ont permis de mieux comprendre le monde, aussi bien scientifiquement que politiquement. Parmi eux, j'aimerais tout particulièrement remercier mes collègues et amis doctorants grâce à qui ces trois années m'ont parues presque trop courtes. Merci d'abord à mes camarades de promotion Enza et Camille, mais aussi à ceux qui sont venus avant nous et qui nous ont guidé sur ce chemin, Jean-Christophe, Lucien, Léo, Cosimo et Aldo. Je remercie aussi ceux qui ont arrivés après nous -Ricardo, Antoine, Gabriele, Ismaïl, Aurélien, Soufiane et Alessandro- et leur souhaite le meilleur pour la suite de leurs travaux.

J'aimerais naturellement terminer en remerciant l'ensemble de mes proches de leur soutien inconditionnel pendant ces trois années. Merci à mes amis du Mesnil, de Montigny, de Versailles et de Châtenay de m'avoir accompagné jusqu'à la fin de ce long "stage de fin d'étude". Merci à ma famille dont le soutien m'a depuis toujours été essentiel. J'aimerais remercier tout particulièrement ma mère pour nous avoir transmis sa curiosité et le goût de l'effort, sans lesquels je ne me serais jamais lancé dans cette aventure.

J'aimerais ici vous témoigner à tous ma plus sincère et profonde gratitude.

Abstract

Certification requirements and the constant pursuit of performance pushes aerospace manufacturers to thoroughly monitor the uncertainties inherent in their products. For this reason, Uncertainty Quantification (UQ) methods must now be integrated as early as possible in the design process, in order to guarantee reliability and performance. In this thesis, we focus on the numerical simulation of turbomachinery flows, and we present two methods for the quantification and reduction of epistemic uncertainties associated with turbulence closure models for the Reynolds Averaged Navier-Stokes (RANS) equations. These arise both from model-form inadequacy and from imperfect knowledge of model parameters.

To make robust predictions under RANS model uncertainty, and to estimate and reduce uncertainties on the resulting solution, we investigate Bayesian multi-model ensembles techniques and, more specifically, Bayesian Model Averaging (BMA). This approach consists in using a set of competing model to make separate predictions of a turbulent flow of interest. Such predictions are then averaged together by using their posterior marginal probabilities, and the resulting model mixture is used to estimate expectancy and confidence intervals of the predicted flow properties. The first method, named Bayesian Model-Scenario Averaging (BMSA), extends BMA to account for the uncertainty in the choice of the flow configurations used to calibrate the model parameters. The second method, named space-dependent BMA (XBMA), produces space-dependent combinations of models by leveraging local information about the flow. Both methods demonstrate good generalization properties when predicting an unseen flow, while retaining the benefit of being non-intrusive, easy to implement, computationally affordable and general. Numerical examples focus on the quantification and reduction of turbulence modeling uncertainties for flows through a compressor cascade at various operating conditions.

Keywords: Uncertainty Quantification, RANS models, BMA, turbomachinery flows.

Résumé

Les exigences des autorités de certification ainsi que la recherche constante de performances élevées poussent les industriels aéronautiques à maîtriser toujours plus finement les incertitudes propres à leurs produits. Pour cette raison, les méthodes de Quantification d'Incertitudes (UQ) sont désormais intégrées dès que possible dans le processus de conception d'une pièce, afin de garantir sa fiabilité ainsi que sa performance. Dans cette thèse, nous nous concentrons sur la simulation numérique d'écoulements dans des turbomachines et nous présentons deux approches pour la quantification et la réduction des incertitudes épistémiques associées aux modèles de turbulence pour la fermeture des équations de Navier-Stokes moyennées à la Reynolds (RANS). Ces incertitudes découlent à la fois de l'inadéquation de la forme du modèle et d'une connaissance imparfaite des paramètres du modèle.

Pour réaliser des prédictions robustes des écoulements en présence d'incertitudes de modèle RANS, et pour estimer et réduire les incertitudes sur la solution obtenue, nous étudions des techniques d'ensembles multi-modèles bayésiens et, plus spécifiquement, les mélanges bayésiens de modèles (BMA). Ce derniers utilisent un ensemble de modèles concurrents pour effectuer des prédictions distinctes d'un écoulement turbulent d'intérêt. Ces prédictions sont ensuite moyennées ensemble en utilisant leurs probabilités marginales *a posteriori*, et le mélange de modèles ainsi obtenu est utilisé pour estimer l'espérance et les intervalles de confiance des propriétés de l'écoulement. La première méthode étudiée, nommée Bayesian Model-Scenario Averaging (BMSA), étend la BMA pour prendre en compte l'incertitude dans le choix des configurations d'écoulement utilisées pour calibrer les paramètres du modèle. La deuxième méthode, nommée BMA spatiale (XBMA), produit des combinaisons de modèles dépendantes de l'espace en tirant parti des informations locales sur l'écoulement. Les deux méthodes possèdent de bonnes propriétés de généralisation lors de la prédiction d'un nouvel écoulement, tout en conservant l'avantage d'être non intrusives, faciles à mettre en œuvre, abordables en termes de coût de calcul et générales. Les exemples numériques portent sur la quantification et la réduction des incertitudes de modélisation de la turbulence pour des écoulements à travers une grille d'aubes de

compresseur avec des conditions de fonctionnement variées.

Mots clés : Quantification d'incertitudes, modèles RANS, BMA, écoulements en turbomachines.

Contents

List of Tables

List of Figures

Chapter 1

Introduction

1.1 General context

In the aeronautical sector, no compromises are accepted on flight safety. For this reason, aviation authorities enforce the strongest regulations in their respective countries and carefully examine for certification each flying element of an aircraft, whether a physical component or a software. In addition to the safety priority, underestimating risk of failure of a component or its expected performance can severely damage the industrial reputation of an Original Equipment Manufacturer (OEM) and bring months of delay and millions euros losses in contract penalties if performance commitments are not honored. To secure these performances at minimal cost, OEM apply modern risk management programs to their products from the design phase through to the testing phase. In the case of real-life aircraft engines for example, time-consuming and cost-intensive iterative methods are used to design each component, in the hope of derisking as much as possible the prototyping and real-life testing stages, which are often seen as moments of truth. This is the case in particular for rotating machinery equipements, of particular interest for this thesis.

In this context, Uncertainty Quantification (UQ) methods have received considerable interest by the aeronautical industry, and industrial manufacturers have been keen at integrating UQ to their design process. The great strength of UQ methods lies in the fact that they do not simply propose a prediction, but also deliver confidence intervals on a prediction. As such, they are a very useful decision-making tool for program managers and allow them to reduce risks very early in the design phase, long before real-life testing.

Before further diving into our subject, let us first state what meaning we give to the word uncer-

tainty. For that purpose we follow the definitions given by the *American Institute of Aeronautics and Astronautics* (AIAA) [8]:

Definition 1 *Uncertainty: A potential deficiency in any phase or activity of the modeling process that is due to a lack of knowledge.*

Uncertainties are therefore different from errors, which are attributed the following definition:

Definition 2 *Error: A recognizable deficiency in any phase or activity of modeling and simulation that is not due to a lack of knowledge.*

We additionally follow Walters and Huyse [9] by distinguishing the *aleatoric* (or *inherent*) uncertainty from the *epistemic* uncertainty. While the first one arises from intrinsic randomness of the system, and therefore cannot be reduced, the latter can be reduced by considering better models or data for example. In their contribution to the 1998 AIAA special issue devoted to the "Credible Computational Fluid Dynamics Simulations", Oberkampf and Blottner [10] identified four main sources of uncertainty and errors arising from the numerical simulation of a physical problem governed by any Partial Differential Equation (PDE), which are listed below:

1. Physical modeling: it can be related to the assumptions made on the problem (like the hypothesis of flow incompressibility in case of CFD for example), to the definition of boundary conditions or to the use of auxiliary physical models, such as chemical reaction models or turbulence models for example.

2. Discretization and solution errors: these are related to errors in the numerical representation of the problem geometry, to the spatial and temporal grid convergence of the method, to errors associated with the inversion of large matrices arising from the discretization of the governing equations, and to truncation-errors associated with the numerical scheme in use.

3. Computer round-off error: such errors correspond to the finite machine precision of the computer.

4. Programming and user errors.

The last two kinds of errors are generally considered negligible if high-precision arithmetic is used for the calculations and by assuming that the computer code and numerical setup have been carefully prepared and debugged.

In the following of the manuscript, we focus on design tools for aircraft engine compressors, and more specifically on Computational Fluids Dynamics (CFD) solvers. CFD has become the cornerstone of fluid flow analysis in both academic studies and engineering applications, mostly in reason of its ability to provide reliable information about the flow, especially when such information is not readily available via experimental campaigns or theoretical reasoning. Nonetheless, the application of UQ approaches to CFD problems is relatively recent, by contrast with structural mechanics or navigation and control methods for example, which have a long history in uncertainty analysis [9]. This can be explained both by the later emergence of CFD as a discipline and, more importantly, by the much higher computational cost of CFD simulations compared, e.g., to solid mechanics simulations. The constant increase in speed and power of computer systems makes the application of UQ possible in CFD design of complex configurations. In the context of this thesis, we will exclusively focus on the physical modeling (1) source of uncertainty in CFD, as the second source of error (relative to the discretization and solution errors) is out of our scope.

1.2 Uncertainties in CFD and RANS modeling

The Navier-Stokes (NS) equations govern the dynamics of fluid flows at all scales but, due to their nonlinear nature, they lead to complex, chaotic solutions for flows characterized by high values of the Reynolds number (Re), which is the case for configurations of industrial interest. This is also true for turbomachinery flows of interest here, which are mostly turbulent, although transition may also play an important role. Direct Numerical Simulations (DNS) could be used, in theory, to resolve all turbulent scales, but the computations are prohibitively expensive, since the required number of grid points scales as $\mathbf{Re}^{9/4}$ [11]. This restricts the application of DNS to fundamental flow configurations at low to moderate Reynolds number, while they remain out of reach for high Reynolds numbers typically encountered in engineering problems. An attractive alternative consists in solving only the largest, most energetic turbulent scales, while modeling the smaller ones. Such an approach, known as Large-Eddy Simulation (LES), reduces computational cost considerably with respect to

DNS, since the number of grid points is now of the order of $\mathbf{Re}^{0.4}$ for free shear flows. Unfortunately, LES remains prohibitively expensive for wall bounded flows at high Reynolds number due to the small energetic scales dominating the dynamics in the near-wall regions [12]. As a consequence, the only strategy affordable for routine use in engineering design is the Reynolds-averaged Navier–Stokes (RANS) approach, which models the entire range of turbulent flow scales. Although notably flawed by various deficiencies – especially for strongly non-equilibrium and possibly transitional flows like those of interest in this work–, its far lower computational makes RANS modeling the workhorse for turbomachinery design.

RANS modeling uncertainties can be classified into four levels [13]: (1) uncertainties related to the validity of the averaging process itself; (2) uncertainties in representing the unclosed Reynolds stress tensor as a function of the mean field; (3) uncertainties in the mathematical form of the constitutive laws used to relate the Reynolds stresses to the mean field and of the auxiliary transport equations for turbulence properties (e.g. for the turbulent kinetic energy or the dissipation); (4) uncertainties in the closure parameters associated with a given model form. The uncertainties described at point (3) are often called "structural" or "model-form" uncertainties, while those at point (4) are called parametric uncertainties [14]. In this work, we intend to provide a Bayesian probabilistic framework for RANS-based predictions of turbulent flows under both parametric uncertainties (4) and model-form uncertainties (3). For this reason, in the following of this chapter we mostly focus on this kind of approaches. The reader is referred to [14] for a more complete review of model uncertainties in RANS models.

1.3 Parametric uncertainties

A natural framework for parametric uncertainties quantification is Bayesian inference, whereby the model coefficients are assigned *a priori* probability distributions (based, e.g., on literature data or expert judgement) that are updated by observing data, leading to the estimation of a so-called *a posteriori* joint probability distribution. More details about Bayesian uncertainty quantification are given in Chapter 3 of this manuscript. With model coefficients represented as random variables following some probability distribution, the model output is also a random quantity, and characterized by a probability distribution. This implies that, in such a framework, the model output is naturally

equipped with uncertainty intervals.

In addition to the possibility of determining confidence intervals, Bayesian inference appears as particularly suited for the problem at hand, for three main reasons. First, RANS models coefficients have been initially calibrated for simple canonic flows (e.g., the decay of homogeneous and isotropic turbulence, flat plate boundary layers, and simple shear flows), which are rather far apart of the turbomachinery flow configurations at stake. Second, Bayesian methods are well-suited to assimilate observed data into the model while accounting for the observation errors on the calibration data. The latter can be small, noisy data sets and can be successively updated as soon as new or better data become available [15]. Finally, Bayesian inference provides information about model sensitivity to the closure coefficients and the universality (or not) of the latter.

In reason of their considerable cost, the application of Bayesian calibration methods to CFD flow models is rather recent. The first attempt of Bayesian calibration in CFD can be found in the work of Cheung et al. [16], where the Spalart-Allmaras turbulence model coefficients were calibrated for a set of experimental boundary layer flows. Oliver and Moser [17], extended the work of Cheung et al. by considering 3 additional RANS models, namely the Baldwin-Lomax, Chien $k-\varepsilon$ and v^2-f models. Edeling et al [3] calibrated five RANS models on 14 turbulent flat plate flows subject to various external pressure gradients. Margheri et al. [18] investigated the parametric uncertainty of the two widely employed Launder-Sharma $k-\varepsilon$ and Menter $k-\omega$ SST models and used physical constraints and data collected from the literature to construct probability distributions for the model coefficients. Papadimitriou and Papadimitriou [19] used adjoint methods to effectively calibrate the Spalart-Allmaras model on a flat-plate, while Guillas et al. [20] recalibrated the $k-\varepsilon$ model on an urban flow. Similarly, Shaefer et al. [21] investigated the uncertainties in the coefficients of the Spalart-Allmaras model on transonic wall-bounded flows and point out the large epistemic intervals on their values.

1.4 Model-form uncertainties

Usual CFD practice of selecting a single turbulence model among all and assuming the latter to the "best" possible model tends to understate the actual uncertainty. Such a problem has been initially investigated in Statistics (e.g. [22]), where a Bayesian approach is once again adopted to account for

model-form uncertainty. Following [14], we classify the current approaches for quantifying the model-form uncertainties associated with RANS simulations into parametric and non-parametric approaches depending on where the uncertainties are introduced.

First, non-parametric approaches introduce uncertainties directly in the mathematical formulation of the models. In context of CFD, it could mean acting on the eddy viscosity, the source terms in the turbulent transport equations or even the Reynolds stress itself. This option is more powerful, as it account for the uncertainties on the mathematical hypothesis founding the models, but is often intrusive and more computationally expensive. On the other hand, parametric approach introduce the uncertainties via the stochastic representation of the model, *i.e.* which is now intended as a realization from a whole distribution (continuous or discrete) of alternative models. For this reason, the parametric approach to the model-form uncertainty is often adapted to a framework constructed for the quantification of the parametric uncertainty (4), as the two are very close. In general, it is not possible to deal with an infinite, continuous set of alternative models, and model uncertainty is estimated by considering a set of competing RANS models. Compared to the parametric approach, the non-parametric one has the considerable advantage of being non-intrusive (no modification of the CFD solver is required), provided that the RANS model coefficients can be prescribed as input variables of the CFD calculation. However, uncertainty is only estimated through the uncertain parameters and the alternative structures in the model set, and no other model form can be captured.

1.4.1 Non-parametric approaches

Non-parametric approaches attempt to estimate directly the error associated with the model-structure, i.e. the mathematical form of the model. For example, the more largely used turbulence models rely on the Boussinesq analogy (see Chapter 2), i.e. a linear constitutive relation for the turbulent stresses, which prevents them of predicting secondary flows in a square duct, whatever the model coefficients. The goal of parametric approaches is to estimate the error induced by such approximation with respect to a reference solution provided, for instance, by a DNS or LES field (called the high-fidelity field). Non-parametric approaches overcome this limitation.

A first example of such an approach can be found in the work of Dow and Wang [23], who inferred a turbulent viscosity field from full-field DNS velocity data for a plane channel. A Gaussian process metamodel was then constructed to predict a correction to the RANS ν_t field. Singh and Duraisamy

[24] corrected the transport equations of the Spalart-Allmaras model by applying a multiplicative discrepancy function $\beta(x)$ to the production term. This method has been proven better at predicting DNS data on a set of channel flow, shock-boundary layer interactions, and flows with curvature and separation than the unmodified Spalart-Allmaras model.

Finally, the last family of non-parametric approaches aimes at estimating a correction for the Reynolds Stresses. The first attempt in that direction was formulated in Oliver and Moser [25], which introduced δ_T, the Reynolds stress discrepancy tensor, to account for model-form uncertainty and propagated it through a set of differential equations. They demonstrated preliminary successes of their approach in plane channel flows at various Reynolds numbers. Their framework laid the foundation for many subsequent works in quantifying and reducing RANS model form uncertainties. The most successful and widely-used paths in this method however consists in applying perturbations directly to the Reynolds stress. Emory, Iaccarino et al. [26, 27, 28] initially build on previous work on Reynolds stress tensor realizability [29, 30, 31], *i.e.*, and specifically the requirement that the tensor be symmetric positive semi-definite, and proposed physics-constrained perturbations of the Reynolds stress tensor, by means of its eigen-decomposition onto the barycentric triangle [32] or the Lumley triangle [29].

Xiao et al. [33] further extended the method by proposing a statistical framework in which the Reynolds stress was modeled as a random field centered on the RANS Reynolds stress. Perturbations were then properly parametrized and the realizability was enforced to explore the uncertainty space. While this method produced significant results, it only allowed the perturbations of the magnitude and shape of the tensor, but not its orientation. In order to overcome this limitation, Xiao et al. [34] then presented an approach where the Reynolds stress tensor is modeled as a 3×3 random matrix centered on the RANS-predicted Reynolds stress, and the perturbations are directly injected under the form of matrix. This has the large benefit of perturbing magnitude, shape and orientation of the Reynolds stress, even if it makes more difficult to directly incorporate physical insights for a specific flow. The two approaches were then compared [35] and proved to produce similar results.

Ling et al. [36] also chose to infer corrections of the Reynolds stresses, by decomposing the Reynolds stress on a basis of invariants of the velocity gradient vector, and then reconstructed the coefficients of the decomposition a neural network regression. Similarly, Weatheritt and Sandberg [37] used Gene-Expression Programming (GEP) to predict the coefficients in the same decomposition.

Such an approach ends up converging towards the development of Explicit Algebraic Stress Models (EARSM), a class of RANS models using nonlinear constitutive relations for the Reynolds stresses. On the other hand, Wang et al. [38] developed a more systematic strategy to predict discrepancies in the magnitude, anisotropy, and orientation of the Reynolds stress tensor, by considering an extended basis of invariants composed of the velocity gradient vector, the gradient of pressure vector and the gradient of turbulent kinetic energy vector. Wu et al. [39] completed this work by learning the linear and nonlinear parts of the Reynolds stress separately, with the linear part treated implicitly to improve model conditioning. Finally, Schmelzer et al. [40] proposed a sparse regression method for the prediction of the anisotropy of the Reynolds stress tensor directly from high-fidelity data. An augmented $k-\omega$ SST model was then constructed with this approach, and delivered more accurate predictions for a set of separating flows. Ben Hassan Saïdi et al. [41] generalized the method to configurations for which full fields of first and second-order turbulent statistics are not available, such as experimental databases for example.

The non-parametric approaches are undeniably promising, and have attracted considerable interest from the CFD community due to their potential for automatic learning RANS models from data. However, they suffer from the following limitations: (1) they tend to lack generality, *i.e.*, they work well for flows similar to those in the training set but can be hardly extrapolated to different flows; (2) they need a significant amount of high-fidelity data (generally costly to obtain and limited to simple, low-Reynolds number configurations) and are not well suited for incomplete, noisy data such as experiments; (3) in most cases, they lead to deterministic predictions and do not provide estimates of confidence intervals due to persisting uncertainties in both model form and closure coefficients. For industrial turbomachinery design (and for engineering design in general), confidence intervals on the predicted quantities of interest (QoI) represent as valuable information as the QoI itself, since they allow estimating uncertainties about the expected system performance early in the design phase. This is why, in this work, we focus instead on "parametric" uncertainty quantification approaches, described in the next paragraph.

1.4.2 Model-mixture approaches

Although parametric approaches infer only posterior distributions of model coefficients, they can also be used for estimating, to some extent, model-form uncertainties. First, one can extend the stochastic framework constructed for the parametric uncertainty to encompass model uncertainty, by providing a stochastic representation of this uncertainty, like in the seminal work [42]. This requires formulating a stochastic model-inadequacy term to be added to the model output, whose hyperparameters are calibrated alongside the physical model coefficients. For instance, [16], Cheung et al. not only recalibrated the Spalart-Allmaras model coefficients but also formulated three stochastic representations for the model inadequacy in terms of observed quantity use for the calibrations (the mean flow velocity), and calibrated the corresponding hyper-parameters. Oliver and Moser [17] investigated various representations of the model inadequacy term, and they assessed them by means of DNS data for plane channel flows. Unfortunately, the estimated inadequacy term cannot be reused for a different geometrical configuration or QoI than those used in the calibration step.

An important byproduct of Bayesian calibration studies, is the possibility of estimating the posterior model probability based on the observed data. Such estimate is the basis for so-called Bayesian model selection. This kind of estimates has been carried out for a set of competing RANS models first in Cheug et al. [16], then in Oliver and Moser [17] and Edeling et al. [3]. The three studies showed that no single "best" model, with a posterior probability much greater than its competitors can be identified.

In the context of turbomachinery design, engineers typically select a single RANS model based on a trade-off between accuracy, computational cost and expert judgment. The standard practice then ignores model uncertainty, which may lead to over-confident predictions. Instead, one could acknowledge that multiple competing models exist, all delivering potentially different but plausible predictions of the same problem, resulting in a source of uncertainty on the model choice. A way for accounting this, consists in adopting a multi-model ensemble point of view.

Various multi-model ensemble methods exist. All methods rely on the idea that combining models generally increases the skill, reliability and consistency of model forecasts. Examples include model forecasts in the sectors of public health (e.g. malaria in Thomson et al. [43]), agriculture (e.g. crop yield in Cantelaube and Terres [44]), and weather- and climate-related applications, (e.g. Palmer

et al. [45]). In the context of RANS modeling, Poroseva et al. [46] explored the potential of the Dempster–Shafer theory of evidence [47] to quantify model uncertainty on the $k-\varepsilon$ and $k-\omega$ models. In all cases, the combined information of several models is reported to be superior to a single-model forecast.

In the Bayesian framework, the most natural multi-model method is Bayesian Model Averaging (BMA), initially proposed by Box and Tiao [48] and later revisited by Draper [22], who largely contributed to the popularity of the method. BMA provides a coherent and systematic formalism to account for model uncertainty, and can be described [22] as the "Bayesian approach to solving the problem of failure to assess and propagate structural uncertainty". In BMA, the predictions from multiple models are combined using the posterior model probabilities as weights, thereby providing a measure for model uncertainty. The evaluation of the posterior model probabilities was initially computationally intractable, which hindered the further development of the method to other scientific communities outside Bayesian statistics. When model probabilities computations were intractable, Mosleh and Apostolakis [49] proposed the adjustment factors method, which extend the range of Bayesian inference to such applications by replacing model probabilities computations by expert opinions. This approach was later extended by Zio and Apostolakis [50] to take different model structures into account.

By the second half of 1990's however, the advances in computational capabilities had greatly reduced the BMA computational burden, which lead to a revival of the method under the impulsion of Draper, Madigan and Raftery [22, 51]. Hoeting et al. [52] formulated a comprehensive tutorial for BMA with emphasis put on implementation and practical matters. Their pivotal work lead to the adoption of BMA in a wide range of applications outside its original community. In their systematic review, Fragoso et al. [53] counted 820 BMA articles published in more than 300 journals or conference proceedings between 1997 and 2016. They range from econometrics –where it is used to forecast future exchange rate [54]–, to oncology –where BMA is employed to estimate the number of cancer cases [55].

In engineering, BMA has been mainly used in hydrology and meteorology, following the work of Raftery et al. [56] where BMA was extended to dynamic systems, and specifically weather forecasts. Results showed an improved predictive capability, with predictions much better calibrated and sharper confidence intervals. Following this work, BMA was used in a variety of applications in meteorology and hydrology [57, 58, 59, 60, 61, 62, 63, 64], with convincing results.

In addition to their good performance, there are strong mathematical properties supporting the use of BMA: In their work, Madigan and Raftery [51] have proven that using BMA results in better prediction (compared by a logarithmic scoring rule) than any single model considered. In the case of interest of this study, where the "truth" is known to be out of the range of the RANS models considered, BMA will asymptotically select the one single model on the ensemble that is closest to the truth in term of Kullback–Leibler divergence [65]. However, other model combination methods can be better suited for a different purpose. Similarly to BMA, stacking [66] is a linear and convex combination of models, which means that the model weights are in $[0, 1]$ and sum to one. By contrast with BMA, stacking uses optimization methods to evaluate the model weights that minimize a cost function, (often leave-one-out (LOO) mean squared error (MSE)), under the constraint of their convexity. By definition, stacking typically outperforms BMA when the considered criterion is the MSE [67] because BMA is not optimized for this task and rather illustrates the fit to the data [68]. Nonetheless, stacking remains less widely used than BMA because classical stacking only provides point estimates, and not the entire posterior distribution [65].

A significant extension to the BMA method is represented by Bayesian Model and Scenario Averaging (BMSA), which includes the concept of "scenario" to BMA. This idea was originally present in [22] but has been formally first described by Meyer et al. [57]. In this case, a scenario is defined as "a general statement about possible future conditions" [57], and illustrated with the following example: a climate change scenario is a general statement describing a possible change in climate. Like BMA, BMSA combines the predictions from multiple models, thereby providing a measure for model uncertainty, using posterior distributions of the coefficients separately inferred from different calibration scenarios. Although BMSA was successfully employed in the hydrological context [57, 61], with Rojas et al. noticing that the use of scenarios lead to more realistic and reliable estimations of the predictive uncertainty, the method was at that time entirely relying on expert judgment for the evaluation of the scenario probabilities. Edeling et al. [3] proposed a new BMSA formulation, easier to implement, in which scenarios are defined as "examples of a class of flows for which we wish to make reliable predictions", but still defined from their explanatory variables,namely, the geometry or boundary conditions for example. This formulation makes scenarios a very well-suited concept for CFD. In the same work, Edeling et al. [3] proposed an objective criterion for the scenario probabilities, independent of any expert judgment and based on the agreement between models. Such a BMSA was then constructed

by averaging five RANS models calibrated on 14 scenarios, corresponding to turbulent flat plate class flows subject to various external pressure gradients. The BMSA method, calibrated on the scenarios of [3], was then successfully applied to a transonic wing configuration in [69]. Merle et al. [70] proposed a alternative criterion for scenario probabilities, which takes into account the quality of the calibration for each competing scenario. Such promising results have been produced on simple academic cases, but their ability at predicting more complex flows such as turbomachinery flows remains to be seen. Additionally, the different criteria for the scenario probabilities have not yet been compared and one could wonder which one to choose.

On the other hand, a broad consensus exists in the RANS modeling community stating that there is no universal best RANS models, but models are known to perform better in some situations and less well in other. Such disparate performance may even occur within the same flow, where a RANS model may be better suited at predicting one region of the flow and less so in another.

Recently, in the field of applied statistics, Yu et al. [71] proposed a novel algorithm, christened *Clustered Bayesian Averaging* (CBA) to combine concurrent models by using space-varying model weights. This is in contrast with both BMA and BMSA, which apply constant weights throughout the flow. An exception is represented by the wing computation of [69], where different scenario weights were applied at different spanwise locations. The CBA method has since been applied to meteorological models with success [72, 73], but no extensions to CFD problems have been considered up to date.

1.5 Objectives and outline

In the present work, we further investigate the Bayesian model averaging approach in the aim of providing robust predictions of turbulent turbomachinery flows under a set of uncertain RANS models.

Specifically, the objectives of thesis are the following:

1. As a first step, we develop a calibration strategy for costly CFD simulations of turbomachinery flows, and we investigate for the first time the potential of BMSA for such configurations, with focus on a compressor cascade.

2. Secondly, we investigate various scenario-weighting strategies for BMSA, in the attemps of re-

ducing computational costs of the prediction while improving the accuracy of the results.

3. Finally, we explore the idea of a space-varying model combination by proposing an algorithm inspired from Yu et al. CBA [71] and well suited to CFD applications.

The thesis is structured as follows. In Chapter 2, we recall the RANS equations and the RANS models used in this work. In Chapter 3, we introduce the Bayesian framework, with a special emphasis on its application to CFD calculations. In Chapter 4, we describe the calibration and validation test cases and the data used for the inference. Chapter 5 is devoted to the first two objectives of this thesis. First, the BMSA methodology is assessed for a compressor cascade. Then the choice of the scenario probability criteria is investigated for the same case. Finally, Chapter 6 addresses the third objective of the study: the proposed algorithm is described in detail, and thoroughly assessed for the compressor flow case. Conclusions and perspectives arising from this work are proposed in the last Chapter.

Chapter 2

Governing equations and numerical tools

Contents

This section introduces the numerical models and tools used in the present work. First, we recall the governing equations for turbulent compressible flows and the RANS models used in the rest of the study. Afterwards, we present the surrogates models used to reduce the number of RANS simulations involved in Bayesian calibration of models coefficients. Finally, we describe the code used and the numerical settings used in the simulations reported later in this manuscript.

2.1 Governing Equations

In this work, turbulent compressible flows are modelled by the Favre-averaged compressible Navier-Stokes equations, also known as compressible RANS equations. We note $\langle . \rangle$ the ensemble average operator and [.] the Favre operator. For any quantity q, we have q' and q" the corresponding fluctuating quantities: q' = q - $\langle q \rangle$ and q" = q - [q]. The differential form of the compressible RANS equations written with respect to a fixed Cartesian reference frame reads :

$$\begin{cases} \dfrac{\partial\langle\rho\rangle}{\partial t} + \dfrac{\partial(\langle\rho\rangle[u_i])}{\partial x_i} = 0 \\ \dfrac{\partial\langle\rho\rangle[u_i]}{\partial t} + \dfrac{\partial(\langle\rho\rangle[u_i][u_j])}{\partial x_j} + \dfrac{\partial\langle p\rangle}{\partial x_i} - \dfrac{\partial\langle\tau_{ij}\rangle + \tau_{ij}^R}{\partial x_j} = 0 \\ \dfrac{\partial\langle\rho\rangle([e_t] + \langle k\rangle)}{\partial t} + \dfrac{\partial\langle\rho\rangle([e_t] + \langle k\rangle)}{\partial x_j} + \dfrac{\partial\langle p\rangle[u_j]}{\partial x_j} - \dfrac{\partial(\langle\tau_{ij}\rangle + \tau_{ij}^R)[u_i]}{\partial x_j} + \dfrac{\partial\langle q_j\rangle + q_j^T}{\partial x_j} = 0 \end{cases} \tag{2.1}$$

where ρ is the density, u_i is the velocity component in the i-th direction x_i, p is the pressure, τ_{ij} is viscous stress tensor, $\tau_{ij}^R = -\langle\rho\rangle[u_i''u_j'']$ is the Reynolds stress tensor, $k = \dfrac{1}{2}[u_i''u_i'']$ is the turbulent kinetic energy and $e_t = \dfrac{1}{2}u_iu_i + e$ is the total energy, with $e = c_vT$ the internal energy, c_v the heat capacity at constant volume and T the temperature. Similarly, q_j is the heat flux which admit the following definition, under the assumption of negligible molecular diffusion and radiant transfer: $q_j = -\kappa\dfrac{\partial T}{\partial x_j}$, where κ is the thermal conductivity.

For a Newtonian fluid and under the classic Stokes' assumption, $\langle\tau_{ij}\rangle$ is a function of the mean strain rate tensor $S_{ij} = \dfrac{1}{2}\left(\dfrac{\partial[u_i]}{\partial x_j} + \dfrac{\partial[u_j]}{\partial x_i}\right)$:

$$\langle\tau_{ij}\rangle = 2\langle\mu\rangle\left(S_{ij} - \frac{1}{3}\frac{\partial[u_k]}{\partial x_k}\delta_{ij}\right)$$

We also note $\Omega_{ij} = \dfrac{1}{2}\left(\dfrac{\partial[u_i]}{\partial x_j} - \dfrac{\partial[u_j]}{\partial x_i}\right)$ the mean rotation rate tensor.

The preceding equations are supplemented by suitable models for the Reynolds stresses and turbulent heat flux. The latter is modeled by means of the turbulent Fourier law:

$$q_j^T = -\frac{c_p\mu_t}{Pr_t}\frac{\partial\langle T\rangle}{\partial x_j}$$

where μ is the molecular viscosity, Pr_t and μ_t respectively indicate the turbulent Prandtl number and the turbulent eddy viscosity. Models for the Reynolds tensor are described in some more detail hereafter. In the following we drop the Reynolds and Favre-averaging symbols to simplify the notations.

2.2 RANS models

To close the system of the RANS equations, a model for the Reynolds stress tensor must be prescribed. Countless models have been introduced in the literature (see e.g. [74]). Such models differ

1. by the form of the constitutive relation chosen to represent the Reynolds tensor
2. by the form of any auxiliary equations used to complete the model definition
3. by the closure coefficients associated with the chosen model form

The choice of the constitutive relation for τ^R is called hereafter a model class, since it determines the general form of the model and affects its application range. The form of such relation is one of the main sources of uncertainty in RANS modeling.

The first class of RANS models considered in this work corresponds to so-called linear eddy viscosity models (LEVM). These assume a linear relationship between τ^R and the mean strain rate, known as Boussinesq analogy.

We also consider an Explicit Algebraic Reynolds Stress Models (EARSM) model, which makes use of nonlinear constitutive equations for the Reynolds stress tensor. Linear eddy viscosity models and Explicit Algebraic Reynolds Stress Models are presented in 2.2.1 and 2.2.2, respectively.

2.2.1 Linear eddy viscosity models

Turbulence models most widely employed in industrial CFD software rely on the so-called Boussinesq analogy. The latter postulates that the Reynolds stress tensor τ^R satisfies a constitutive relation similar to the one used to model viscous stresses in Newtonian fluids:

$$\tau^R = 2\mu_t\Big(S_{ij} - \frac{1}{3}\frac{\partial u_k}{\partial x_k}\delta_{ij}\Big) - \frac{2}{3}\rho k\delta_{ij} \tag{2.2}$$

Under the Boussinesq hypothesis, the turbulence modeling problem is reduced to the determination of the two scalar quantities k and μ_t.

In the following we mostly focus on transport-equation models, which use auxiliary transport equations for the evaluation of the unknown turbulent properties. The most widely used models in this family are two-equation models, which generally rely on a transport equation for k and another quantity allowing to determine μ_t. More precisely, we selected three models widely used in industrial codes, namely the $k-\tilde{\varepsilon}$ [75], $k-\omega$ [74] and $k-l$ [76] model. In our analysis, we also consider the popular Spalart-Allmaras [77] model, which employs directly one transport equation for the quantity $\tilde{\nu}$.

The models considered in the present study are further described in the following subsections.

2.2.1.1 Launder–Sharma $k-\tilde{\varepsilon}$ model

The family of $k-\tilde{\varepsilon}$ models uses two auxiliary transport equations for the turbulent kinetic energy k and for the isotropic rate of dissipation $\tilde{\varepsilon} = \varepsilon - \varepsilon_0$, with ε_0 the value of the turbulent dissipation at the wall. We select the Launder-Sharma [75] version of the $k-\tilde{\varepsilon}$ model, described by the following set of equations:

$$\begin{cases} & \mu_t = C_\mu f_\mu \dfrac{\rho k^2}{\tilde{\varepsilon}} \\ \dfrac{\partial(\rho k)}{\partial t} + \dfrac{\partial(\rho u_j k)}{\partial x_j} & = P - \rho\tilde{\varepsilon} + \dfrac{\partial}{\partial x_j}\left[(\mu + \dfrac{\mu_t}{\sigma_k})\dfrac{\partial k}{\partial x_j}\right] \\ \dfrac{\partial(\rho \tilde{\varepsilon})}{\partial t} + \dfrac{\partial(\rho u_j \tilde{\varepsilon})}{\partial x_j} & = C_{\varepsilon 1}\dfrac{\tilde{\varepsilon}}{k}P - C_{\varepsilon 2} f_2 \dfrac{\rho\tilde{\varepsilon}^2}{k} + 2\dfrac{\mu\mu_t}{\rho}\Big(\dfrac{\partial^2 u_i}{\partial x_j \partial x_k}\Big)^2 + \dfrac{\partial}{\partial x_j}\left[(\mu + \dfrac{\mu_t}{\sigma_\varepsilon})\dfrac{\partial \tilde{\varepsilon}}{\partial x_j}\right] \end{cases} \tag{2.3}$$

with $P = \tau_{ij}^R \dfrac{\partial u_i}{\partial x_j}$. Two damping functions are used to account for the near-wall effects:

$$f_2 = 1 - 0.3e^{-Re_T^2}$$
$$f_\mu = \exp\Big(\frac{-3.4}{(1 + Re_T/50)^2}\Big)$$

where $Re_T = \dfrac{\rho k^2}{\tilde{\varepsilon}\mu}$. The transport equations and the eddy viscosity definition involve six closure coefficients: C_μ, $C_{\varepsilon 1}$, $C_{\varepsilon 2}$, σ_k, σ_ε and κ, with κ the von Karman constant. The Launder-Sharma $k-\tilde{\varepsilon}$ model uses the following values for its closure coefficients:

$$C_\mu = 0.09 \quad ; \quad C_{\varepsilon 1} = 1.44 \quad ; \quad C_{\varepsilon 2} = 1.92$$
$$\sigma_k = 1.0 \quad ; \quad \sigma_\varepsilon = 1.3 \quad ; \quad \kappa = 0.41$$

The number of independent closure coefficients can be reduced by considering the following relationships, derived for canonical flows [11] (see also [3]):

$$\kappa^2 = \sigma_\varepsilon C_\mu^{1/2}(C_{\varepsilon 2} - C_{\varepsilon 1}) \tag{2.4}$$

$$\frac{P}{\varepsilon} = \frac{C_{\varepsilon 2} - 1}{C_{\varepsilon 1} - 1} \tag{2.5}$$

This relations reduces the number of independent coefficients needing calibration to 4.

2.2.1.2 Wilcox(2006) $k-\omega$ model

We consider the $k-\omega$ model presented in [74], generally known under the name Wilcox(2006) model[†], which relies on transport equations for k and for the specific dissipation ω:

$$\begin{cases} & \mu_t = \dfrac{\rho k}{\widehat{\omega}} \\ \dfrac{\partial(\rho k)}{\partial t} + \dfrac{\partial(\rho u_j k)}{\partial x_j} & = P - \beta^* \rho k \omega + \dfrac{\partial}{\partial x_j}\left[(\mu + \sigma_k \dfrac{\rho k}{\omega})\dfrac{\partial k}{\partial x_j}\right] \\ \dfrac{\partial(\rho \omega)}{\partial t} + \dfrac{\partial(\rho u_j \omega)}{\partial x_j} & = \dfrac{\gamma \omega}{k} P - \beta \rho \omega^2 + \dfrac{\partial}{\partial x_j}\left[(\mu + \sigma_\omega \dfrac{\rho k}{\omega})\dfrac{\partial \omega}{\partial x_j}\right] + \sigma_d \dfrac{\rho}{\omega}\dfrac{\partial k}{\partial x_j}\dfrac{\partial \omega}{\partial x_j} \end{cases} \tag{2.6}$$

The definition of μ_t uses the following modified specific dissipation:

$$\widehat{\omega} = \max\Big[\omega, C_{lim}\sqrt{\frac{2\overline{S}_{ij}\,\overline{S}_{ij}}{\beta^*}}\Big]$$

where $\overline{S}_{ij} = S_{ij} - \dfrac{1}{3}\dfrac{\partial u_k}{\partial x_k}\delta_{ij}$. This model uses eight closure coefficients, seven of which are independent, with the following standard values and damping functions:

$$\beta^* = 0.09 \quad ; \quad \sigma_k = 0.6 \quad ; \quad \sigma_\omega = 0.5 \quad ; \quad \kappa = 0.41$$

$$\beta = \beta_0 f_\beta \quad ; \quad \beta_0 = 0.0708 \quad ; \quad C_{lim} = \frac{7}{8}$$

$$\sigma_d = \frac{1}{8}\mathbb{1}_{\left[\frac{\partial k}{\partial x_j}\frac{\partial \omega}{\partial x_j} > 0\right]} \quad ; \quad \gamma = \frac{\beta_0}{\beta^*} - \sigma_\omega \frac{\kappa^2}{\sqrt{\beta^*}} = \frac{13}{25}$$

$$f_\beta = \frac{1 + 85\chi_\omega}{1 + 100\chi_\omega} \quad ; \quad \chi_\omega = \left|\frac{\Omega_{ij}\Omega_{jk}\widehat{S_{ki}}}{(\beta^*\omega)^3}\right| \quad ; \quad \widehat{S_{ki}} = S_{ki} - \frac{1}{2}\frac{\partial u_m}{\partial x_m}\delta_{ki}$$

2.2.1.3 Smith's $k-l$ model

The $k-l$ model, initially proposed by Smith [76], uses transport equations for the turbulent kinetic energy k and the turbulent length scale l. The model is intended to simplify the formulation of Smith's

[†]https://turbmodels.larc.nasa.gov/wilcox.html

$k-kL$ model [78] in the wall region. The model transport equations write:

$$\begin{cases} & \mu_t = \mu\chi f_\mu \\ \dfrac{\partial(\rho k)}{\partial t} + \dfrac{\partial(\rho u_j k)}{\partial x_j} = & P - \dfrac{\rho(2k)^{3/2}}{B_1 l} - 2\mu\Big(\dfrac{\partial\sqrt{k}}{\partial x_j}\Big)^2 + \dfrac{\partial}{\partial x_j}\left[(\mu + \dfrac{\mu_t}{\sigma_k})\dfrac{\partial k}{\partial x_j}\right] \\ \dfrac{\partial(\rho l)}{\partial t} + \dfrac{\partial(\rho u_j l)}{\partial x_j} = & (2-E_2)\dfrac{\rho\sqrt{2k}}{B_1}\Big[1 - \Big(\dfrac{l}{K\eta}\Big)^2\Big] + \rho l\dfrac{\partial u_j}{\partial x_j} - \dfrac{\mu_t}{\sigma_l}\dfrac{1}{l}\Big(\dfrac{\partial l}{\partial x_j}\Big)^2\Big(\dfrac{l}{K\eta}\Big)^2 \\ & +2\dfrac{\mu_t}{\sigma_l}\dfrac{1}{k}\Big(\dfrac{\partial l}{\partial x_j}\dfrac{\partial k}{\partial x_j}\Big) + \dfrac{\partial}{\partial x_j}\left[(\mu + \dfrac{\mu_t}{\sigma_l})\dfrac{\partial l}{\partial x_j}\right] \end{cases} \tag{2.7}$$

The auxiliary functions necessary for the definition of μ_t are defined as :

$$\chi = \frac{\rho l\sqrt{2k}}{\mu B_1^{1/3}} \quad ; \quad f_\mu = \Big(\frac{c_1^4 f_1 + c_2^2\chi^2 + \chi^4}{c_1^4 + c_2^2\chi^2 + \chi^4}\Big)^{1/4}$$
$$f_1 = \exp\Big[-50\Big(\frac{l}{K\eta}\Big)^2\Big] \quad ; \quad c_1 = 25.5 \quad ; \quad c_2 = 2$$

The model uses five closure coefficients:

$$B_1 = 18 \quad ; \quad E_2 = 1.2 \quad ; \quad \kappa = 0.41 \quad ; \quad \sigma_k = 1.43 \quad ; \quad \sigma_l = 1.43$$

2.2.1.4 Spalart-Allmaras one-equation model

In contrast to the $k-\varepsilon$, $k-\omega$ and $k-l$ models, the Spalart-Allmaras model [77] uses a single transport equation. The transported variable is the quantity $\tilde{\nu}$, which corresponds to the kinematic eddy viscosity $\nu_t = \dfrac{\mu_t}{\rho}$ far from the walls. Since its first introduction in 1994, many corrections and improvements have been proposed for the Spalart-Allmaras model. In this work, we use the standard Spalart-Allmaras model, as described in the Turbulence Modeling Resource website [‡] of the NASA Langley research center. The model transport equation writes:

$$\begin{cases} & \mu_t = \rho\tilde{\nu} f_{v1} \\ \dfrac{\partial\tilde{\nu}}{\partial t} + u_j\dfrac{\partial\tilde{\nu}}{\partial x_j} = & c_{b1}(1-f_{t2})\hat{S}\tilde{\nu} - \left[c_{w1}f_w - \dfrac{c_{b1}}{\kappa^2}f_{t2}\right]\Big(\dfrac{\tilde{\nu}}{d}\Big)^2 \\ & +\dfrac{1}{\sigma}\Big[\dfrac{\partial}{\partial x_j}\Big((\nu+\tilde{\nu})\dfrac{\partial\tilde{\nu}}{\partial x_j}\Big) + c_{b2}\dfrac{\partial\tilde{\nu}}{\partial x_i}\dfrac{\partial\tilde{\nu}}{\partial x_i}\Big] \end{cases} \tag{2.8}$$

[‡]https://turbmodels.larc.nasa.gov/spalart.html

The model requires the definition of several damping functions, presented hereafter:

$$\chi = \frac{\tilde{\nu}}{\nu} \quad ; \quad f_{v1} = \frac{\chi^3}{\chi^3 + c_{v1}^3} \quad ; \quad f_{v2} = 1 - \frac{\chi}{1 + \chi f_{v1}} \quad ; \quad f_w = g\Big[\frac{1 + c_{w3}^6}{g^6 + c_{w3}^6}\Big]^{1/6}$$
$$\Omega_{mag} = \sqrt{2\Omega_{ij}\Omega_{ij}} \quad ; \quad \hat{S} = \Omega_{mag} + \frac{\tilde{\nu}}{\kappa^2 d^2} f_{v2}$$
$$g = r + c_{w2}(r^6 - r) \quad ; \quad r = \min\Big[\frac{\tilde{\nu}}{\hat{S}\kappa^2 d^2}, 10\Big] \quad ; \quad f_{t2} = c_{t3}\exp(-c_{t4}\chi^2)$$

There is therefore 10 closure coefficients associated with the Spalart-Allmaras model, 9 of which being independent. Their standard values are presented hereafter.

$$c_{b1} = 0.1355 \quad ; \quad \sigma = 2/3 \quad ; \quad c_{b2} = 0.622 \quad ; \quad \kappa = 0.41 \quad ; \quad c_{v1} = 7.1$$
$$c_{w1} = \frac{c_{b1}}{\kappa^2} + \frac{1 + c_{b2}}{\sigma} \quad ; \quad c_{w2} = 0.3 \quad ; \quad c_{w3} = 2 \quad ; \quad c_{t3} = 1.2 \quad ; \quad c_{t4} = 0.5$$

We then fix the c_{t3} and c_{t4} parameters to their standard values, similarly to [3]. Ultimately, we are left with 7 independent model parameters.

2.2.2 Non Linear eddy viscosity model

LEVM RANS models are numerically robust and among the less expensive RANS models, but they fail to predict complex flows. The linear constitutive equation arising from the Boussinesq analogy does not provide a correct representation of turbulence anisotropy, especially for flows characterized by significant non-equilibrium effects, such as rotation, strong pressure gradients, etc.

One alternative to Boussinesq models is to compute the Reynolds stress directly by considering six extra transport equations, each corresponding to one component of the symmetrical Reynolds Stress tensor. Such models are often called Differential or Full Reynolds Stress Models (DRSM or FRSM), or simply Reynolds Stress Models (RSM).

This class of RANS models have been proven more accurate than Boussinesq models for predicting non-equilibrium behavior of the flow, such as in separated flow. However, their complexity brings a large number of extra closure coefficients to the model, which can be an issue when model calibration is desired. Additionally, RSM models are often less numerically robust than Boussinesq models and require the solution of seven additional transport equations in 3-D flow and four equations in 2-D.

In this work, an intermediate solution is adopted. A non-linear constitutive relation is used for the computation of the Reynolds stress τ^R, in conjunction with transport equations for two turbulence

scales (like in classical Boussinesq models) in order to determine a turbulent characteristic time. Based on a preliminary accuracy study, we select the Explicit Algebraic Reynolds Stress Models (EARSM) $k-kL$ model of [79], presented hereafter.

2.2.2.1 EARSM $k-kL$ model

EARSM model are obtained by assuming local equilibrium of turbulence. Under this assumption, it is possible to neglect advection and diffusion terms in the Reynolds stress transport equations and, after some algebraic manipulations, explicit algebraic expressions for the Reynolds stresses are obtained, i.e., a nonlinear constitutive relation. Wallin & Johansson [80] proposed the following constitutive relation:

$$\overline{u_i' u_j'} = k\Big(\frac{2}{3}\delta_{ij} - 2C_\mu^{eff}\frac{k}{\varepsilon}S_{ij} + a_{ij}^{(ex)}\Big) \tag{2.9}$$

The preceding expression differs from the standard linear eddy viscosity models for two reasons: first, the C_μ^{eff} coefficient is not constant but depends on the velocity gradients and turbulent quantities; the last term $a_{ij}^{(ex)}$ is non-linear and represents the extra anisotropy of the Reynolds stress which is a complex function of the velocity gradients and turbulent quantities. The full expressions of C_μ^{eff} and $a_{ij}^{(ex)}$ proposed by Wallin & Johansson can be found in Appendix A of their work [80]. Their model for the anisotropy tensor has the following closure coefficients:

$$C_1 = 1.80 \quad ; \quad C_1' = 0.0 \quad ; \quad C_2 = 0.80 \quad ; \quad C_3 = 2.0 \quad ; \quad C_4 = \frac{10}{9}$$

The preceding constitutive relation is supplemented with transport equations for the turbulent kinetic energy k and the product of the turbulent kinetic energy with the turbulent length scale $kL = \dfrac{k^{5/2}}{\varepsilon}$ proposed by Smith [78]. Specifically, we used the equations given in [79], corresponding to the "Low Reynolds" version of the EARSM $k-kL$ model. The equations write:

$$\begin{cases} & \mu_t = \rho C_\mu f_\mu \dfrac{\Phi}{\sqrt{k}} \\ \dfrac{\partial(\rho k)}{\partial t} + \dfrac{\partial(\rho u_j k)}{\partial x_j} & = P - \rho\dfrac{k^{5/2}}{\Phi} - \dfrac{2\mu k}{\eta^2} + \dfrac{\partial}{\partial x_j}\left[(\mu + \dfrac{\mu_t}{\sigma_k})\dfrac{\partial k}{\partial x_j}\right] \\ \dfrac{\partial(\rho \Phi)}{\partial t} + \dfrac{\partial(\rho u_j \Phi)}{\partial x_j} & = C_{\Phi_1}\dfrac{\Phi}{k}P - C_{\Phi_2}\rho k^{3/2} - C_{\Phi\omega}f_\omega\rho^3\dfrac{\Phi^{5/2}}{\mu^2\sqrt{\eta}} + 2C_{\Phi k}\dfrac{\mu_t}{\sqrt{k}}\dfrac{\partial\sqrt{k}}{\partial x_j}\dfrac{\partial\Phi}{\partial x_j} + 4C_{\Phi\Phi}\mu_t(\dfrac{\partial\sqrt{\Phi}}{\partial x_j})^2 \end{cases} \tag{2.10}$$

where $\Phi = kL$ and η is the wall distance.

The auxiliary functions necessary for the damping in the near-wall regions are defined as:

$$f_\omega = \exp(-C_{\omega 1} R_\eta) \quad ; \quad R_\eta = \frac{\eta\sqrt{k}}{\nu} \quad ; \quad f_\mu = 1 - \exp(-C_{\omega 2} R_\eta^{3/2})$$

The $k - kL$ model has 11 closure coefficients with the following standard values :

$$C_{\Phi_1} = 1 \quad ; \quad C_{\Phi_2} = 0.58 \quad ; \quad C_\mu = 0.09 \quad ; \quad C_{\Phi k} = 1.53 \quad ; \quad C_{\Phi\Phi} = -1.38$$

$$\sigma_k = 0.9 \quad ; \quad \sigma_\Phi = 1.6 \quad ; \quad C_{\Phi\omega} = 0.00077 \quad ; \quad C_{\omega_1} = 0.08 \quad ; \quad C_{\omega 2} = 0.00325 \quad ; \quad \kappa = 0.41$$

In the rest of this work the $C_{\omega 2}$ is fixed to its standard value.

2.3 RANS solver and computational setup

The simulations presented in the following are conducted by using the CFD solver *elsA* version v4.0.2, developed by the ONERA [81]. *elsA* solves the compressible Euler, Navier-Stokes or RANS equations on both structured and unstructured multi-block grids, from the low subsonic to the high supersonic flow regime. Concerning the RANS equations, a large variety of turbulence models from eddy viscosity to full Reynolds stress models (RSM) are implemented in the solver [82, 79]. Laminar-turbulent transition modelling relies either on criteria, or on solving additional transport equations [82]. Following the works of Deck [83, 84], Zonal Detached Eddy Simulation (ZDES) and LES are also available. The system of equations is solved by means of a cell-centered finite volume discretization. Space discretization schemes include classical second order centered or upwind schemes and higher order schemes [81]. The Cassiopee module [85] developed at ONERA was used in the pre-processing and post-processing steps.

Finally, the calibration of the RANS models also required access to each model parameters. We developed a path to set the values of the coefficients directly from *elsA* user interface. This development has been integrated and is available for every *elsA* user using version v4.0.2 or higher.

2.4 Chapter summary

In this section, we first recalled the general formulation of the compressible RANS equations. We then presented the five RANS models used in the rest of the work. Four of them are linear eddy-viscosity models, namely the $k - \tilde{\varepsilon}$, $k - \omega$, $k - l$ and Spalart-Allmaras models, while the fifth uses

a non-linear relation for the the Reynolds stress, namely the EARSM $k - kL$ model. Finally, we described the *elsA* CFD solver, which was used in this work.

In the next chapter, we present the Bayesian framework used for the calibration of the RANS models and for the prediction of the selected QoIs.

Chapter 3

Bayesian inference applied to computer models

Contents

In this chapter, we present the mathematical methods used in the rest of the thesis. First, we recall some generalities about the Bayesian framework, formulated in the context of Computational Fluid Dynamics (CFD). Subsequently, we focus on the Bayesian Model Averaging (BMA) approach, which constitutes the cornerstone of the model-form uncertainty quantification strategy adopted in this work.

3.1 Bayesian inference

One of the strongest arguments for the use of the Bayesian approach lies in its common-sense interpretabilty, in addition to its flexibility that helps its application on complex problems. In the context of Bayesian probabilities, the confidence interval provided for an unknown Quantity of Interest

(QoI) is immediately understandable, as it can be interpreted as the interval that has high probability of containing the QoI. On the contrary, frequentist intervals can only be interpreted as a sequence of similar inferences occurring over a repeated practice. Recent developments in applied statistics have led to an increased emphasis on the Bayesian approach as it seems likely that most users of standard confidence intervals give them a common-sense Bayesian interpretation [15].

Let us consider a quantity $\widehat{\delta}$, stemming from a physical phenomenon, that we try to estimate through a general model of the form:

$$\delta = M(\mathbf{x}; \boldsymbol{\theta}, S) \tag{3.1}$$

where M is a model for the underlying physics, $\mathbf{x}$ is a vector of the explanatory space, $\boldsymbol{\theta}$ is the set of parameters upon which the model depends, S is the scenario to which the underlying model M is applied and δ is an output of the model.

In the context of CFD, δ represents an output of a CFD flow solver supplemented by a turbulence model; both the CFD solver and the turbulence model constitute the model M. For instance, δ is the solution for the conservative flow variables provided by the CFD solver. $\mathbf{x} = (x, y, z)^T$ is mainly a vector of the physical space (but could be a vector of a different space - see Chapter 6). $\boldsymbol{\theta}$ is the vector of $N_{\boldsymbol{\theta}}$ closure coefficients associated with the RANS model described in Chapter 2. At last, in the following, we assume that S is defined by assigning a set of variables (that we will consider as deterministic) describing the geometry, the boundary conditions, the fluid properties and all other specifications required to carry out a computation.

Most often, δ is not the only QoI provided by M and we could be interested in predicting an other QoI Δ stemming directly from M or from post-processing of δ. We denote by $\boldsymbol{\Delta} = (\Delta_1, ..., \Delta_{N_{\boldsymbol{\Delta}}})^T$ a vector of such QoI. As an example, $\boldsymbol{\Delta}$ can be constituted by flow quantities extracted at given locations in the flow, like velocity profiles, pressure or skin friction distributions, or also by global quantities like forces, power outputs or mass flow. Such outputs also depend on the scenario, the turbulence model and the corresponding closure coefficients, *i.e.*:

$$\Delta = M(\mathbf{x}; \boldsymbol{\theta}, S) \tag{3.2}$$

Let us suppose now that a vector of measures $\overline{\boldsymbol{\delta}} = (\overline{\delta}_1, ..., \overline{\delta}_d, ..., \overline{\delta}_{N_{\overline{\delta}}})^T$ and model predictions $\boldsymbol{\delta} = (\delta_1, ..., \delta_d, ..., \delta_{N_{\overline{\delta}}})^T$ of $\widehat{\delta}$ are available at points $\mathbf{X} = \{\mathbf{x}_d\}_{d=1}^{N_{\overline{\delta}}}$, where $\delta_d = M(\mathbf{x}_d; \boldsymbol{\theta}, S)$. Components

of $\overline{\boldsymbol{\delta}}$ and $\boldsymbol{\delta}$ can be connected through the stochastic relationship:

$$\overline{\delta}_d = \delta_d + e_d \tag{3.3}$$

where e_d is a random variable representing the observation error. Implicitly, in Eq. (3.3), we assume that $\delta_d = \widehat{\delta}_d$, which is obviously not true ; another kind of error, *i.e.* model error, is then generally added in the stochastic model (3.3) to account for the fact that the model cannot capture $\widehat{\delta}$ even with the best set of coefficients [42, 86]. The formulation of the model error is discussed later. On the other hand, the observation error e_d is often represented as a normal random variable with a 0 mean and a prescribed variance σ_e^2. Consequently, a random vector $\tilde{\boldsymbol{\delta}}$ can now be defined, the distribution of which $f(\tilde{\boldsymbol{\delta}})$ represents the probability to observe $\overline{\boldsymbol{\delta}}$ at points $\mathbf{X}$ (here f stands for the probability density function (pdf)).

Finally, the vector of closure parameters $\boldsymbol{\theta}$ is only known imperfectly. It is then treated as a random vector representing our belief on $\boldsymbol{\theta}$. It turns out that $\boldsymbol{\delta}$ and Δ, which depend on $\boldsymbol{\theta}$, become random vectors with a pdf of the form $f(\boldsymbol{\delta}|\boldsymbol{\theta})$. Furthermore, the observed value $\tilde{\boldsymbol{\delta}}$ follows a pdf of the form $f\left(\tilde{\boldsymbol{\delta}}|\boldsymbol{\delta} = M(\mathbf{X};\boldsymbol{\theta},S),\boldsymbol{\theta}\right)$. For brevity, the foregoing equation is generally written $f\left(\tilde{\boldsymbol{\delta}}|\boldsymbol{\theta}\right)$

Statistical inference is the task of drawing conclusions on yet unobserved QoIs from numerical data. Observed data $\overline{\boldsymbol{\delta}}$ being given, the problem consists in estimating the values of the parameters $\boldsymbol{\theta}$ that cause the model output $\boldsymbol{\delta}$ to best fit the data $\overline{\boldsymbol{\delta}}$. This process is also referred to as the inverse statistical problem in the literature.

3.1.1 Bayes rule

The goal of the inverse problem formulation is to gain new knowledge about $\boldsymbol{\theta}$ by constructing an improved representation of its pdf, based on prior knowledge and assimilation of observed data. By invoking the Bayes rule, we can write :

$$f\left(\boldsymbol{\theta}|\tilde{\boldsymbol{\delta}}\right) = \frac{f\left(\tilde{\boldsymbol{\delta}}|\boldsymbol{\theta}\right)}{f\left(\tilde{\boldsymbol{\delta}}\right)} f\left(\boldsymbol{\theta}\right) \tag{3.4}$$

where $f(\boldsymbol{\theta})$ is the joint prior probability distribution of the parameters, representing the initial belief about $\boldsymbol{\theta}$, $f\left(\tilde{\boldsymbol{\delta}}|\boldsymbol{\theta}\right)$ is the likelihood function and corresponds to the probability of observing $\overline{\boldsymbol{\delta}}$, a

realization of the random variable $\tilde{\boldsymbol{\delta}}$, if the parameters are assigned the distribution $f(\boldsymbol{\theta})$. The parameter posterior probability distribution $f\left(\boldsymbol{\theta}|\tilde{\boldsymbol{\delta}}\right)$ represents the updated knowledge of $\boldsymbol{\theta}$ given the observed data vector $\overline{\boldsymbol{\delta}}$. The denominator $f\left(\tilde{\boldsymbol{\delta}}\right)$ in (3.4) is the evidence of the data, and is defined by:

$$f\left(\tilde{\boldsymbol{\delta}}\right) = \int_{\boldsymbol{\theta}} f\left(\tilde{\boldsymbol{\delta}}|\boldsymbol{\theta}\right) f(\boldsymbol{\theta})\, d\boldsymbol{\theta} \tag{3.5}$$

As the evidence is independent of $\boldsymbol{\theta}$, it is often treated as a normalization constant so that (3.4) writes:

$$f\left(\boldsymbol{\theta}|\tilde{\boldsymbol{\delta}}\right) \propto f\left(\tilde{\boldsymbol{\delta}}|\boldsymbol{\theta}\right) f(\boldsymbol{\theta}) \tag{3.6}$$

In other words, calibration compares the model predictions and the observations to construct the pdf of the parameter vector $\boldsymbol{\theta}$ that is the most likely to capture the data.

3.1.2 Bayesian Prediction

Suppose now that we want to evaluate the probability of observing the value $\overline{\delta}^*$ at point $\mathbf{x}^*$, $\overline{\delta}^*$ being a realization of the random variable $\tilde{\delta}^*$. The joint pdf between $\tilde{\delta}^*$, $\tilde{\boldsymbol{\delta}}$ and $\boldsymbol{\theta}$ can be written as:

$$f\left(\tilde{\delta}^*, \tilde{\boldsymbol{\delta}}, \boldsymbol{\theta}\right) = f\left(\tilde{\delta}^*|\tilde{\boldsymbol{\delta}}, \boldsymbol{\theta}\right) f\left(\boldsymbol{\theta}|\tilde{\boldsymbol{\delta}}\right) f\left(\tilde{\boldsymbol{\delta}}\right) \tag{3.7}$$

that we integrate so that:

$$\begin{aligned}
\int_{\boldsymbol{\theta}} f\left(\tilde{\delta}^*, \tilde{\boldsymbol{\delta}}, \boldsymbol{\theta}\right) d\boldsymbol{\theta} &= \int_{\boldsymbol{\theta}} f\left(\tilde{\delta}^*|\tilde{\boldsymbol{\delta}}, \boldsymbol{\theta}\right) f\left(\boldsymbol{\theta}|\tilde{\boldsymbol{\delta}}\right) f\left(\tilde{\boldsymbol{\delta}}\right) d\boldsymbol{\theta} \\
f\left(\tilde{\delta}^*, \tilde{\boldsymbol{\delta}}\right) &= f\left(\tilde{\boldsymbol{\delta}}\right) \int_{\boldsymbol{\theta}} f\left(\tilde{\delta}^*|\tilde{\boldsymbol{\delta}}, \boldsymbol{\theta}\right) f\left(\boldsymbol{\theta}|\tilde{\boldsymbol{\delta}}\right) d\boldsymbol{\theta} \\
f\left(\tilde{\delta}^*|\tilde{\boldsymbol{\delta}}\right) f\left(\tilde{\boldsymbol{\delta}}\right) &= f\left(\tilde{\boldsymbol{\delta}}\right) \int_{\boldsymbol{\theta}} f\left(\tilde{\delta}^*|\tilde{\boldsymbol{\delta}}, \boldsymbol{\theta}\right) f\left(\boldsymbol{\theta}|\tilde{\boldsymbol{\delta}}\right) d\boldsymbol{\theta}
\end{aligned} \tag{3.8}$$

that ultimately gives:

$$f\left(\tilde{\delta}^*|\tilde{\boldsymbol{\delta}}\right) = \int_{\boldsymbol{\theta}} f\left(\tilde{\delta}^*|\boldsymbol{\theta}\right) f\left(\boldsymbol{\theta}|\tilde{\boldsymbol{\delta}}\right) d\boldsymbol{\theta} \tag{3.9}$$

where we assume a conditional independence of $\tilde{\delta}^*$ and $\tilde{\boldsymbol{\delta}}$ when $\boldsymbol{\theta}$ is known. $f\left(\tilde{\delta}^*|\tilde{\boldsymbol{\delta}}\right)$ is called the posterior predictive distribution.

For the posterior predictive distribution of the unobserved QoI Δ, we can no longer use the likelihood $f\left(\tilde{\boldsymbol{\delta}}|\boldsymbol{\theta}\right)$ because the underlying stochastic model were only developed for $\tilde{\boldsymbol{\delta}}$ and cannot be applied

for Δ. Instead we simply assume a minimalistic stochastic model corresponding to the relation (3.2) with no error. Hence the conditional distribution of Δ is:

$$f\left(\Delta^*|\boldsymbol{\theta}\right) = \delta(\Delta^* - M(\mathbf{x}^*;\boldsymbol{\theta},S)) \tag{3.10}$$

where δ is the Dirac distribution. Then, the posterior predictive distribution of Δ^* is calculated by:

$$f\left(\Delta^*|\tilde{\boldsymbol{\delta}}\right) = \int_{\boldsymbol{\theta}} \delta(\Delta^* - M(\mathbf{x}^*;\boldsymbol{\theta},S)) f\left(\boldsymbol{\theta}|\tilde{\boldsymbol{\delta}}\right) d\boldsymbol{\theta} \tag{3.11}$$

meaning that the posterior distribution $\boldsymbol{\theta}|\tilde{\boldsymbol{\delta}}$ is only propagated through the model M. The computation of $f\left(\tilde{\delta}^*|\tilde{\boldsymbol{\delta}}\right)$ in Eq. 3.9 represents a considerable computational cost in CFD context, as it require the computation of the integral at every position $\mathbf{x}^*$. Instead, we follow [3] and treat $\tilde{\delta}^*$ as Δ^* in Eq. 3.11, *i.e.* we simply propagate the parameters posterior distribution $\boldsymbol{\theta}|\tilde{\boldsymbol{\delta}}$ in the model M.

3.2 Application to CFD

The application of this Bayesian framework to the context of CFD requires the addition of a few concepts and notations detailed hereafter.

3.2.1 Stochastic modeling choices for CFD

In the case of turbulence models, the closure parameters are assigned many different values in practice. Margheri *et al.* [18] investigated the parametric uncertainty of two widely employed turbulence models and used physical constraints and data collected from the literature to construct probability distributions for the coefficients. Although it would be possible to use such an approach to construct informative prior distributions for various turbulence models, the latter could strongly constrain the posterior, especially if relatively few observed data is available. For this reason, we prefer to follow a common practice in Bayesian inference [87, 70] and we choose uninformative priors, *i.e.* uniform priors, for each component of $\boldsymbol{\theta}$ (supposed independent). Since RANS models have been carefully designed, we are confident in assuming that the standard values should be included in the range of the prior. We therefore choose uniform priors that include standard values of model coefficients found in the literature, as done in [16, 88]. Furthermore, there is no evidence that model predictions would be improved by choosing closure coefficients with significant deviations from the standard values. The

prior intervals are therefore chosen to be large enough to allow a good exploration of the parameter space, while avoiding too large or too small values preventing the CFD solver to converge. Also note that excessively large prior distributions may lead to overfitting problems, resulting in posterior coefficients that fit very well the calibration data, but deteriorate predictions of unobserved QoIs. The likelihood function $f\left(\tilde{\boldsymbol{\delta}}|\boldsymbol{\theta}\right)$ is a statistical model that aims at representing observation errors (discrepancies between the data and its true unobserved value) and just as much as model inadequacies. The latter account for the fact that part of the physics is missed by the model due to any approximation introduced in its construction, so that the true phenomenon can never be exactly captured, even with the best possible model coefficients.

In the present calculations, the observation error is modeled as an additive noise and the model inadequacy as a multiplicative term, as in [16]. We assume that the data $\overline{\boldsymbol{\delta}}$ is a flow quantity observed at a given location $\mathbf{x}_d$, related to the observation error by:

$$\overline{\delta}_d = \widehat{\delta}_d + e_d \tag{3.12}$$

with e_d the observation noise at position $\mathbf{x}_d$ and $\widehat{\delta}_d$ the (unobserved) true value of the QoI vector. The components of the observation noise are assumed to be uncorrelated in space and normally distributed, with zero mean and standard deviation σ_e.

To account for the model inadequacy, we assume that the output δ_d of the model is connected to the true unobserved value $\widehat{\delta}_d$ by a coefficient η_d:

$$\widehat{\delta}_d = \eta_d \delta_d \tag{3.13}$$

We choose the model errors to be independent and Gaussian, *i.e.* $\eta_d \sim \mathcal{N}(1, \sigma_\eta^2)$ where σ_η is an additional uncertain hyper-parameter that needs to be calibrated, and is therefore concatenated to the vector of parameters $\boldsymbol{\theta}$. The hyper-parameter σ_η is a measure of the model inadequacy, *i.e.*, an indicator of the accuracy of a given model, calibrated for a given scenario. The introduction of a model inadequacy term mitigates the risk of overfitting the calibration, as it relaxes constraints. For more detailed discussion, see [22].

The preceding choices for η_d and e_d lead to a likelihood function of the form:

$$f(\tilde{\boldsymbol{\delta}}|\Delta,\boldsymbol{\theta}) = \frac{1}{\sqrt{(2\pi)^{N_{\tilde{\delta}}}|\mathbf{K}|}} \exp\left[-\frac{1}{2}(\tilde{\boldsymbol{\delta}}-\boldsymbol{\delta}(\boldsymbol{\theta}))^T\mathbf{K}^{-1}(\tilde{\boldsymbol{\delta}}-\boldsymbol{\delta}(\boldsymbol{\theta}))\right] \tag{3.14}$$

with $\mathbf{K} = \mathbf{K}_e + \mathbf{K}_M$ where $\mathbf{K}_e$ is a diagonal matrix representing the observational error vector and $\mathbf{K}_M = \sigma_\eta^2\mathbf{I}$ a diagonal matrix reflecting model inadequacy.

The calibration method used for the inference of the models parameters is presented in the next section.

3.3 Markov-Chain Monte Carlo and Surrogate modeling

The Bayes rule (3.4) is an analytical expression for the posterior of $\boldsymbol{\theta}$ when the model M is an analytical function. However, when it comes to complex models such as those of interest here, the Eq. (3.4) cannot be used to compute the posterior probability explicitly. Instead, a numerical approximation of the posterior is determined by sampling the parameter space. Besides, computing the integral for $f\left(\tilde{\boldsymbol{\delta}}\right)$ is a challenging task, as the posterior of $\boldsymbol{\theta}$ is often very peaked and close to a Dirac function: a coarse discretization of the parameter space would not capture the peak while a fine discretization would be computationally expensive. A better approach is due to Metropolis *et al.* in the early 50's [89]. Based on Markov chains, the Markov-Chain Monte Carlo (MCMC) of Metropolis *et al.* is a 2-step acceptance/rejection method that allows to draw samples from non-standard pdfs (more efficient methods exist for standard pdfs). For Bayesian inference, the algorithm draws samples of the posterior pdf of $\boldsymbol{\theta}$. In a sense, it is a clever exploration of the parameter space, focusing on regions where the posterior is the most likely. In the calculations presented in the following, we use the Metropolis-Hastings algorithm [90] available in the *pymc*[†] open library. To stop computing the chain, we use kinds of go/no go flags that indicate whether the chain is rather close to a Markov chain (for there is no real stopping criteria). Those flags are: the traces, the steadiness of the first two moments, the Geweke z-score [91] (which is a statistical flag that compares the head and the tail of the chain) and the auto-correlations. For more details concerning such flags, we refer to [70]. Typically, $\mathcal{O}(10^5)$ samples are needed to reach convergence, which is unacceptably high for costly RANS models.

[†]https://github.com/pymc-devs/pymc

To reduce the computational effort to an amenable level, we approximate $M(\mathbf{x};\boldsymbol{\theta},S)$, required in the argument of the likelihood, by means of surrogate models based on a Gaussian Process Regression [92]. A Gaussian Process is a flexible and natively Bayesian method widely used for problems in which input variables are continuous. Let us consider a probability space $(\Omega,\mathcal{F},\mathbb{P})$, a measure space $(R,\mathcal{B}(R))$ and a set T. A stochastic process $Z(\mathbf{x})$, $\mathbf{x}\in T$, is a set of random variables defined on $(\Omega,\mathcal{F},\mathbb{P})$, indexed by T and whose values are in $\mathfrak{S}$. $Z(\mathbf{x})$ is Gaussian if and only if for all finite set $C\subset T$, $Z(C)$ is Gaussian. For this work, $\mathfrak{S}=\mathbb{R}$ and $T\subset\mathbb{R}^d$. A Gaussian Process GP is completely defined by its mean function $\mu(\mathbf{x})$ and its covariance function $k(\mathbf{x},\overline{\mathbf{x}})$. We refer to [15] for a more complete description of the method. In this work, we use the Gaussian Process Regression module available in *scikit-learn* [93]. We impose a zero mean function and a Matern-3/2 kernel whose hyper-parameters are selected through likelihood maximization performed by the L-BFGS-B [94] optimizer available in the *scipy* library [95].

For performing the regression, a set of RANS calculations is run by Latin Hypercube Sampling (LHS) of the parameter space [96], optimized under the Maximum Projection Design criterion. This criterion ensures optimal space filling by maximizing the minimal distance between points of the LHS, for every projection in parameter sub-spaces. We construct a separate surrogate based on N_{GP} RANS samples for each concurrent turbulence model and each calibration scenario considered. $N_{GP}=200$ for the linear eddy viscosity models and $N_{GP}=400$ for the $EARSM$ $k-kL$ model, as the latter has more degrees of freedom. The initial sampling requires a total of 4800 CFD calculations. This represents a considerable computational effort, but it is done once prior to the calibration phase. For a given model and a given calibration scenario, the N_{GP} samples are used to build a surrogate for each one of the observed QoIs.

The reliability of the surrogate models is checked by means of a Leave-One-Out cross-validation. For each model and configuration case considered in the study, we compute the well-known Q^2 criterion

defined by

$$Q^2[GP] = 1 - \frac{\frac{1}{N_{GP}} \sum_{i=1}^{N_{GP}} \left(M(\mathbf{x}_i; \boldsymbol{\theta}, S) - GP_{\mathbf{X}_i}(\mathbf{x}_i)\right)^2}{\frac{1}{N_{GP}-1} \sum_{i=1}^{N_{GP}} \left(M(\mathbf{x}_i; \boldsymbol{\theta}, S) - E\right)^2} \quad \text{with} \quad E = \frac{1}{N_{GP}} \sum_{i=1}^{N_{GP}} M(\mathbf{x}_i; \boldsymbol{\theta}, S) \tag{3.15}$$

where $\mathbf{X} = \{\mathbf{x}_j\}_{j=1}^{N_{GP}}$, $\mathbf{X}_i = \{\mathbf{x}_j | 1 \leq j \leq N_{GP}, j \neq i\}$ and $GP_{\mathbf{X}_i}$ indicates that the Gaussian Process Regression has been performed on $\mathbf{X}_i$. $Q^2 \in [0; 1]$; the closer to 1 is Q^2, the closer to M is GP. The Q^2 criterion may be interpreted as a noise/signal ratio, the signal being the model M and the noise corresponding to the inaccuracy of the Gaussian Process.

3.4 Bayesian Model Averaging

When considering the prediction of a physical phenomenon such as turbulence, it is often challenging to select one single model from an ensemble of competing models M_m, $1 \leq m \leq N_M$. Some models might be better suited at predicting some physical phenomenon or regions of interest but there is no a priori universal model to use in every situation. In such cases, one may consider that each model has a share of the available information, and that predictions must be formulated from multiple model predictions. The Bayesian Model Averaging (BMA) approach provides a coherent framework for mixing model predictive inference in Bayesian context.

Let us consider a set $\mathcal{M} = \{M_1, ..., M_m, ..., M_{N_M}\}$ of N_M models, each one with a vector of parameters $\boldsymbol{\theta}_m$. Let also consider a scenario S, be common to all models, for which data $\overline{\boldsymbol{\delta}}$ are available. Within the Bayesian framework, models in the set may be interpreted as the realizations of a discrete, qualitative random variable $\mathcal{M}$, whose probability mass function (pmf) $p(M = M_m)$ represents our trust that model M_m best matches the observed vector $\overline{\boldsymbol{\delta}}$. The joint pdf $f\left(\tilde{\delta}^*, \tilde{\boldsymbol{\delta}}, \mathcal{M} = M_m, \boldsymbol{\theta}\right)$ can be established as

$$f\left(\tilde{\delta}^*, \tilde{\boldsymbol{\delta}}, M_m, \boldsymbol{\theta}\right) = f\left(\tilde{\delta}^* | \tilde{\boldsymbol{\delta}}, M_m, \boldsymbol{\theta}\right) f\left(\boldsymbol{\theta} | \tilde{\boldsymbol{\delta}}, M_m\right) p\left(M_m | \tilde{\boldsymbol{\delta}}\right) f\left(\tilde{\boldsymbol{\delta}}\right) \tag{3.16}$$

where we write M_m instead of $M = M_m$ for brevity. Integrating Eq. (3.16) over $\boldsymbol{\theta}$ leads to

$$\begin{aligned} \int_{\boldsymbol{\theta}} f\left(\tilde{\delta}^*, \tilde{\boldsymbol{\delta}}, M_m, \boldsymbol{\theta}\right) d\boldsymbol{\theta} &= \int_{\boldsymbol{\theta}} f\left(\tilde{\delta}^* | \tilde{\boldsymbol{\delta}}, M_m, \boldsymbol{\theta}\right) f\left(\boldsymbol{\theta} | \tilde{\boldsymbol{\delta}}, M_m\right) p\left(M_m | \tilde{\boldsymbol{\delta}}\right) f\left(\tilde{\boldsymbol{\delta}}\right) d\boldsymbol{\theta} \\ f\left(\tilde{\delta}^*, \tilde{\boldsymbol{\delta}}, M_m\right) &= p\left(M_m | \tilde{\boldsymbol{\delta}}\right) f\left(\tilde{\boldsymbol{\delta}}\right) \int_{\boldsymbol{\theta}} f\left(\tilde{\delta}^* | \tilde{\boldsymbol{\delta}}, M_m, \boldsymbol{\theta}\right) f\left(\boldsymbol{\theta} | \tilde{\boldsymbol{\delta}}, M_m\right) d\boldsymbol{\theta} \end{aligned} \tag{3.17}$$

where $f\left(\tilde{\delta}^*, \tilde{\boldsymbol{\delta}}, M_m\right)$ is the marginal distribution. Summing over models M_m we obtain:

$$\begin{aligned} \sum_{m=1}^{N_M} f\left(\tilde{\delta}^*, \tilde{\boldsymbol{\delta}}, M_m\right) &= \sum_{m=1}^{N_M} p\left(M_m | \tilde{\boldsymbol{\delta}}\right) f\left(\tilde{\boldsymbol{\delta}}\right) \int_{\boldsymbol{\theta}} f\left(\tilde{\delta}^* | \tilde{\boldsymbol{\delta}}, M_m, \boldsymbol{\theta}\right) f\left(\boldsymbol{\theta} | \tilde{\boldsymbol{\delta}}, M_m\right) d\boldsymbol{\theta} \\ f\left(\tilde{\delta}^*, \tilde{\boldsymbol{\delta}}\right) &= f\left(\tilde{\boldsymbol{\delta}}\right) \sum_{m=1}^{N_M} p\left(M_m | \tilde{\boldsymbol{\delta}}\right) \int_{\boldsymbol{\theta}} f\left(\tilde{\delta}^* | \tilde{\boldsymbol{\delta}}, M_m, \boldsymbol{\theta}\right) f\left(\boldsymbol{\theta} | \tilde{\boldsymbol{\delta}}, M_m\right) d\boldsymbol{\theta} \\ f\left(\tilde{\delta}^* | \tilde{\boldsymbol{\delta}}\right) f\left(\tilde{\boldsymbol{\delta}}\right) &= f\left(\tilde{\boldsymbol{\delta}}\right) \sum_{m=1}^{N_M} p\left(M_m | \tilde{\boldsymbol{\delta}}\right) \int_{\boldsymbol{\theta}} f\left(\tilde{\delta}^* | \tilde{\boldsymbol{\delta}}, M_m, \boldsymbol{\theta}\right) f\left(\boldsymbol{\theta} | \tilde{\boldsymbol{\delta}}, M_m\right) d\boldsymbol{\theta} \\ f\left(\tilde{\delta}^* | \tilde{\boldsymbol{\delta}}\right) &= \sum_{m=1}^{N_M} p\left(M_m | \tilde{\boldsymbol{\delta}}\right) \int_{\boldsymbol{\theta}} f\left(\tilde{\delta}^* | \tilde{\boldsymbol{\delta}}, M_m, \boldsymbol{\theta}\right) f\left(\boldsymbol{\theta} | \tilde{\boldsymbol{\delta}}, M_m\right) d\boldsymbol{\theta} \\ f\left(\tilde{\delta}^* | \tilde{\boldsymbol{\delta}}\right) &= \sum_{m=1}^{N_M} p\left(M_m | \tilde{\boldsymbol{\delta}}\right) f\left(\tilde{\delta}^* | \tilde{\boldsymbol{\delta}}, M_m\right) \end{aligned} \tag{3.18}$$

where $f\left(\tilde{\delta}^* | \tilde{\boldsymbol{\delta}}, M_m\right)$ is the posterior predictive distribution of $\tilde{\delta}^*$ for the model M_m, $f\left(\tilde{\delta}^* | \tilde{\boldsymbol{\delta}}, M_m, \boldsymbol{\theta}\right)$ is the likelihood and

$$\begin{aligned} f\left(\boldsymbol{\theta} | \tilde{\boldsymbol{\delta}}, M_m\right) &= \frac{f\left(\boldsymbol{\theta}, \tilde{\boldsymbol{\delta}}, M_m\right)}{f\left(\tilde{\boldsymbol{\delta}}, M_m\right)} \\ &= \frac{f\left(\tilde{\boldsymbol{\delta}} | \boldsymbol{\theta}, M_m\right) f\left(\boldsymbol{\theta}, M_m\right)}{f\left(\tilde{\boldsymbol{\delta}}, M_m\right)} \\ &= \frac{f\left(\tilde{\boldsymbol{\delta}} | \boldsymbol{\theta}, M_m\right) f\left(\boldsymbol{\theta} | M_m\right) f\left(M_m\right)}{f\left(\tilde{\boldsymbol{\delta}} | M_m\right) f\left(M_m\right)} \\ &= \frac{f\left(\tilde{\boldsymbol{\delta}} | \boldsymbol{\theta}, M_m\right) f\left(\boldsymbol{\theta} | M_m\right)}{f\left(\tilde{\boldsymbol{\delta}} | M_m\right)} \end{aligned} \tag{3.19}$$

because of the Bayes Rule. The posterior model probability is ultimately calculated as

$$p\left(M_m | \tilde{\boldsymbol{\delta}}\right) = \frac{f\left(\tilde{\boldsymbol{\delta}} | M_m\right) p\left(M_m\right)}{\sum_{i=1}^{N_M} f\left(\tilde{\boldsymbol{\delta}} | M_i\right) p\left(M_i\right)} \tag{3.20}$$

where $p\left(M_m\right)$ is the prior model probability (i.e. the probability of M_m before observing the data) and $f\left(\tilde{\boldsymbol{\delta}} | M_m\right)$ is the likelihood of the model. The evidence - the denominator of (3.20) - is usually treated as a normalization constant.

For an unobserved QoI Δ, the posterior predictive $f\left(\Delta^*|\tilde{\boldsymbol{\delta}}, M_m\right)$ is obtained by propagating the parameter posteriors $\boldsymbol{\theta}|\tilde{\boldsymbol{\delta}}, M_m$ through each model M_m, leading to an expression similar to eq. (3.18):

$$f\left(\Delta^*|\tilde{\boldsymbol{\delta}}\right) = \sum_{m=1}^{N_M} p\left(M_m|\tilde{\boldsymbol{\delta}}\right) f\left(\Delta^*|\tilde{\boldsymbol{\delta}}, M_m\right) \tag{3.21}$$

where $f\left(\Delta^*|\tilde{\boldsymbol{\delta}}, M_m\right)$ is the posterior predictive distribution of Δ obtained by propagating the posterior $\boldsymbol{\theta}|\tilde{\boldsymbol{\delta}}, M_m$ through the model M_m.

The first two statistical moments of $\tilde{\delta}^*|\tilde{\boldsymbol{\delta}}$ (namely, the expectancy and the variance) are obtained by computing the following integrals:

$$\begin{aligned} E\left[\tilde{\delta}|\tilde{\boldsymbol{\delta}}\right] &= \int_{\tilde{\delta}} \tilde{\delta} f\left(\tilde{\delta}|\tilde{\boldsymbol{\delta}}\right) d\tilde{\delta} \\ &= \int_{\tilde{\delta}} \tilde{\delta} \sum_{m=1}^{N_M} p\left(M_m|\tilde{\boldsymbol{\delta}}\right) f\left(\tilde{\delta}|\tilde{\boldsymbol{\delta}}, M_m\right) d\tilde{\delta} \\ &= \sum_{m=1}^{N_M} p\left(M_m|\tilde{\boldsymbol{\delta}}\right) \int_{\tilde{\delta}} \tilde{\delta} f\left(\tilde{\delta}|\tilde{\boldsymbol{\delta}}, M_m\right) d\tilde{\delta} \\ &= \sum_{m=1}^{N_M} p\left(M_m|\tilde{\boldsymbol{\delta}}\right) E\left[\tilde{\delta}|\tilde{\boldsymbol{\delta}}, M_m\right] \end{aligned} \tag{3.22}$$

$$\begin{aligned} Var\left[\tilde{\delta}|\tilde{\boldsymbol{\delta}}\right] = &\sum_{m=1}^{N_M} p\left(M_m|\tilde{\boldsymbol{\delta}}\right) Var\left[\tilde{\delta}|\tilde{\boldsymbol{\delta}}, M_m\right] \\ &+ \sum_{m=1}^{N_M} p\left(M_m|\tilde{\boldsymbol{\delta}}\right) \left(E\left[\tilde{\delta}|\tilde{\boldsymbol{\delta}}, M_m\right] - E\left[\tilde{\delta}|\tilde{\boldsymbol{\delta}}\right]\right)^2 \end{aligned} \tag{3.23}$$

where $E\left[\tilde{\delta}|\tilde{\boldsymbol{\delta}}, M_m\right]$ and $Var\left[\tilde{\delta}|\tilde{\boldsymbol{\delta}}, M_m\right]$ are the mean and the variance of the posterior predictive distribution of $\tilde{\delta}|\tilde{\boldsymbol{\delta}}, M_m$. The variance is decomposed in two contributions: the first term of the right hand side of (3.23) is the variance induced by uncertainty on the model parameters while the second term is the variance due to discrepancies in the predictions delivered by the competing models in $\mathcal{M}$. In the BMA formalism, the first contribution is called *within-model variance* and the second *between-model variance*. BMA has shown better predictive performance than the selection of a single model and gives more stable results in general [71].

BMA can be seen as the application of the Bayes' rule to a "hyper-model" consisting of a distribution across models and a distribution on the parameters within each model [71]. It produces a

prediction as a weighted average of multiple models as any model mixing method. However, BMA uses the posterior model probability of each model as its weight in the mixing. The posterior model probability being obtained from their likelihood over the training data, it is a direct measurement of their ability to accurately predict the training data. BMA thus puts its trust in the most accurate models for the calibration scenario, while still accounting for the uncertainty in model selection.

Specification of the prior model probability $p(M_m)$ has been recognized as a challenge from the beginning [52]. Hoeting *et al.* consider a reasonable choice to assume that all models are equally likely when there is only limited information on the relative plausibility of the models. Following this recommendation, multiple authors [3, 62, 70, 97, 98] have chosen uninformative uniform priors for the models.

3.4.1 MAP approximation

The posterior distributions obtained from the calibrations must be propagated through the model to compute the posterior predictive distribution of $\tilde{\delta}$ or any other QoI Δ, as previously described. This step requires an Uncertainty Quantification (UQ) method. Such methods are based on sampling strategies, the number of required samples being more or less important (from the classical Monte Carlo method requiring a large amount of samples to the less demanding Polynomial Chaos Expansion [99]). However, the quantification would still require an intractable number of RANS computations, even in the case of Polynomial Chaos Expansion. Surrogate modeling is not yet an affordable strategy because it limits the propagation to a subset of variables for which a surrgate model has been constructed (typically, these are the same variables used for model calibration, as discussed in Chapter 5). The advent of powerful machine learning algorithms, such as Deep Neural networks, is expected to make possible, in the near future building surrogate models for a complete CFD solution, but they are still the object of current research [100, 101]. A workaround solution is to approximate the full posterior distributions by Dirac distributions centred on their Maximum A Posteriori (MAP) value, as proposed in [69]. By using this approximation, the posterior parametric uncertainty is neglected, but the computational cost associated with the propagation of the posteriors through the numerical model corresponds to that of a single deterministic CFD computation. With this choice, a BMA prediction requires only as many computations as the number of models in $\mathcal{M}$, N_M, instead of various

hundreds of thousands of calculations, as typically required by Monte Carlo UQ. Furthermore, since the parameters are no longer considered as random variables in the propagation step, the BMA formula can be applied to any QoI, whether or not a surrogate model has been build beforehand. This allows ultimately to reconstruct the full stochastic solution associated with the set of concurrent models at stake.

3.5 Chapter summary

In this chapter, we presented the Bayesian methods used in the rest of the study. First, we recalled the general framework of Bayesian inference, and we particularized it to the case of CFD models. After that, we focused on Bayesian calibration methods used in the following, and we discussed the need of surrogate models to alleviate the computational burden associated with repeated CFD solves during the calibration process. The fundamentals of the BMA method, which constitutes the cornerstone of the developments reported in Chapters 5 and 6, were also recalled. In the next chapter, we describe the data used in the present thesis.

Chapter 4

Reference data and simulation setup

Contents

In this chapter, we introduce the reference data used for model calibration and validation in the rest of the study. First, a set of flat plate experimental data available from 1968 AFOSR-IFP-Stanford conference is presented. Such data were used for the calibration of RANS models in a previous study [3]. In this work we use coefficients calibrated for this data set to predict the flow through a linear compressor cascade. Afterwards, the NACA 65 V103 − 220 compressor cascade configuration is presented, along with associated reference data sets. The numerical settings used for the corresponding RANS calculations are also briefly presented.

4.1 Flat plate configuration

The 1968 AFOSR-IFP-Stanford conference [2] and the 1980 − 81 AFOSR-HTTM-Stanford Conference on Complex Turbulent Flows [102] presents the results of a wide experimental campaign on flat plate configurations subject to various external pressure gradients. The goal was to provide trustworthy data sets for the numerical modeling of turbulent flows. The flows are loosely classified in terms of the external pressure gradient as "favorable" ($\frac{\partial \overline{p}}{\partial x} < 0$), "mildly adverse", "moderately ad-

Identification	Type	Description
1400	Zero	Equilibrium boundary layer at constant pressure
1300	Fav	Near-equilibrium boundary layer in moderate negative pressure gradient
2700	Fav	Equilibrium boundary layer in mild negative pressure gradient
6300	Fav	Near-equilibrium boundary layer growing beneath potential flow on model spillway
2100, 2133, 2134	Div	Boundary layer on large airfoil-like body; pressure gradient first mildly negative, then strongly positive, with eventual separation
2400	Div	Initial equilibrium boundary layer in moderate positive pressure gradient; pressure gradient abruptly decreases to zero, and flow relaxes to new equilibrium
1100	Mild adv	Boundary layer in diverging channel
2500	Mild adv	Equilibrium boundary layer in mild positive pressure gradient
3300	Mod adv	Boundary layer, initially at constant pressure, developing into equilibrium flow in moderate positive pressure gradient
0141	Str adv	Boundary-layer with strong adverse pressure gradient
1200	Str adv	Boundary layer in diverging channel with eventual separation
4400	Str adv	Boundary layer in strong positive pressure gradient

Table 4.1: Flows from [1, 2]. Flow selection and description from [3].

verse" and "strongly adverse" ($\frac{\partial \overline{p}}{\partial x} > 0$), x being the streamwise position. This classification is based upon "qualitative observations of the velocity profile shape with respect to the zero-pressure gradient case and incipient separation". Wilcox [1] identified the 15 "best" cases, *i.e.* the "cases that satisfy the momentum integral equation" and one constant pressure case from the data sets produced by these two conferences. The data consist in hot-wire measurements of time-averaged velocity profiles across the boundary layer. Selected normalized experimental streamwise velocity profiles $u^+ \equiv \frac{\overline{u}_1}{u_\tau}$ are reported in Fig. 4.1, where $u_\tau = \sqrt{\frac{\tau_w}{\rho}}$ is the friction velocity. The x-axis represents $y^+ \equiv \frac{x_2}{\delta_\nu}$, the distance to the wall normalized by the the length-scale of the viscous layer $\delta_\nu = \frac{u_\tau}{\nu}$.

Edeling et al. [3] selected 12 cases out of Wilcox's work plus two extra cases from the AFOSR-IFP-Stanford conference, more representative of an airfoil-like body. For those two cases the pressure gradient is first mildly negative, then strongly positive, with an eventual separation. In reason of this special behavior, we label cases 2100, 2133, 2134 and 2400 as 'diverse pressure gradient'. Edeling et al. [3] carried out the BMSA procedure described in Chapter 5 and obtained encouraging results for the prediction of flat plate flows outside the calibration data set as well as for separated incompressible flow and 3D transonic flow with shocks [69].

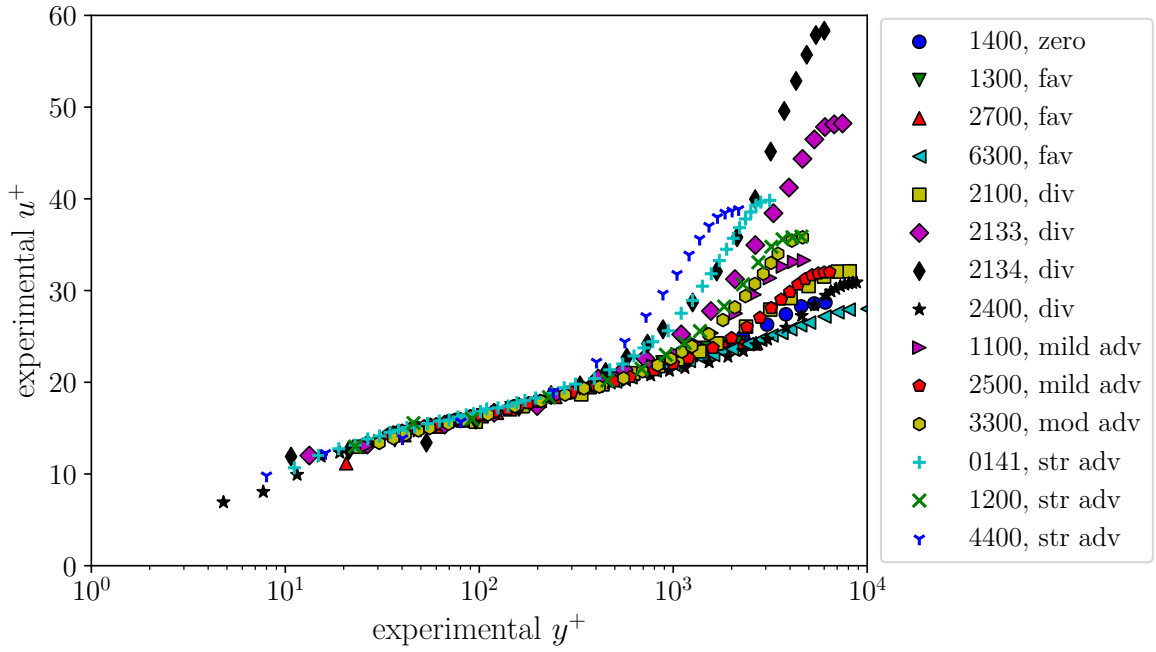

Figure 4.1: Experimental data set. Flows from [1, 2].

In Chapter 5, we use sets of coefficients pre-calibrated in [3] for flows in Table 4.1 to predict a linear compressor cascade (see next section) by using BMSA.

4.2 NACA 65 V103 cascade

In the following, we investigate a compressor cascade configuration working at various operating conditions. More specifically, we focus on the NACA 65 V103 − 220 linear compressor cascade, widely studied in the past years [103, 6, 104, 105, 7].

This cascade is representative of the mid-span section of a stator blade in a highly loaded axial compressor [103]. The blade aspect ratio being $h/l = 1.36$, it has been observed from the oil flow visualizations performed on the blade surface [106] that the flow "can be considered two-dimensional in the mid-span section" for this considered range of Mach and Reynolds numbers. This observation justifies the use of a 2-D approximation: only a single plane corresponding to the blade mid-span is considered in RANS simulations, which is extruded over a short spanwise distance for performing LES calculations (see [7]). The geometrical data of the cascade and the definitions of angles and distances are copied from the work of Hilgenfeld et al. [6] displayed in Fig. 4.2. The design conditions of the

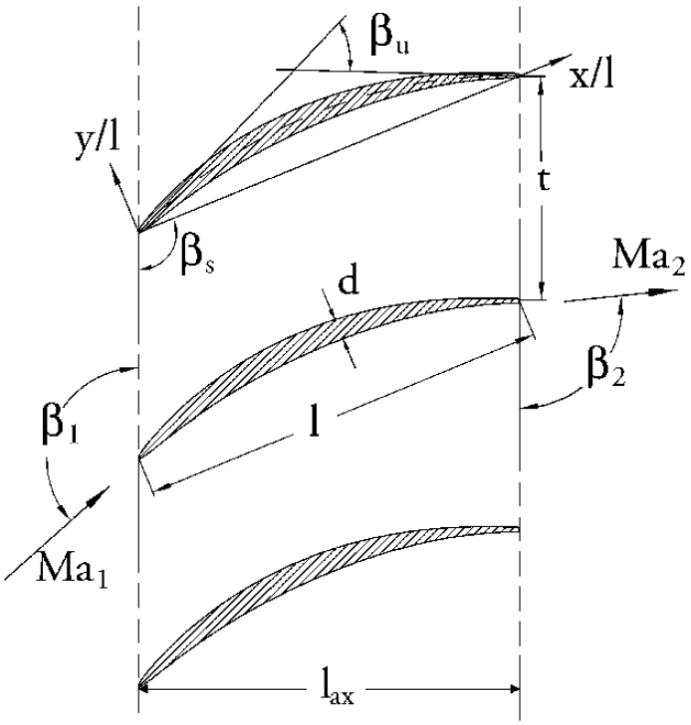

Design Conditions	
Ma_1	0.67
Re_1	450 000
β_1	132°
β_2	96°
l	220 mm
l_{ax}	203.25 mm
t/l	0.55
d/l	0.055
β_s	112.5°
δ_u	48°

Figure 4.2: Sketch and design conditions of the NACA 65 V103 − 220 linear compressor cascade. Sketch copied on from [6].

original cascade are presented on the same figure.

Although high-fidelity simulations exist in the literature for this cascade (e.g. [105, 7]) the databases are not publicly available and we were not able to obtain the solution full fields nor the averaged quantities. The generation of high-fidelity data set is a complex and time-consuming task beyond the scope of the present research. For that reason, we restricted our analysis to the high-fidelity data published in Leggett's et al. work, which carried out LES simulations of the cascade at both design and off-design conditions. Such high-fidelity LES data are used in Chapter 5 for the Bayesian calibration and the validation of our stochastic models. An additional data set of reference data was also generated by using the EARSM $k-kL$ model and used for training and validation of mixtures of lower fidelity Boussinesq models, as discussed in Chapter 6.

In the following we first describe the numerical setup used for the present simulations. Afterwards, we present the LES and EARSM $k-kL$ reference data set used for numerical model calibrations.

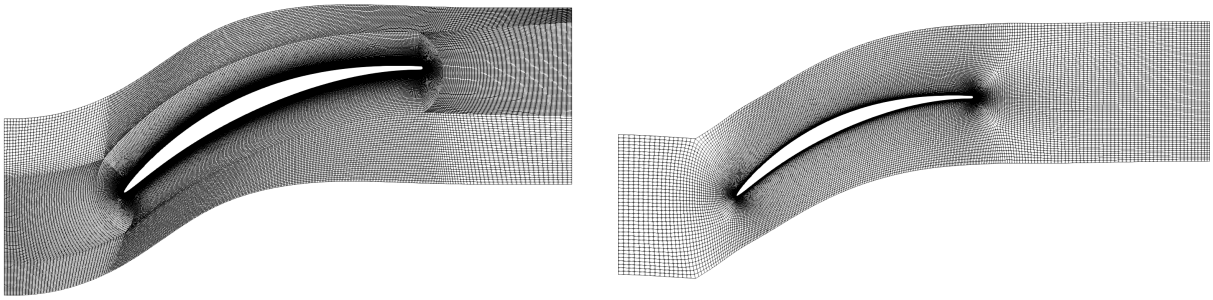

(a) Grid used in Chapter 5. (b) Grid used in Chapter 6.

Figure 4.3: Grid used for the RANS computations.

4.2.1 Numerical setup

All of the RANS calculations reported in this manuscript only require the consideration of a single blade passage, since periodic boundary conditions are used to represent the entire cascade.

The two grids used in this work are shown in Fig. 4.3. The computational domain is discretized by means of the ICEM software for the first grid as well as Autogrid for the second. These two softwares are used to create block-structured meshes to be used by the *elsA* CFD solver. The first grid (Fig. 4.3a) was used for the computations in Chapter 5. Its domain extends from 0.4 axial-chord upstream of the leading edge to 0.5 axial-chord downstream the trailing edge and its computational grid is composed by $200,000$ vertex distributed on 12 blocks. The second grid (Fig. 4.3b) was used for the computations in Chapter 6. The second domain extends from 0.5 axial-chord upstream of the leading edge to 1.0 axial-chord downstream the trailing edge and its computational grid is composed of 80180 vertex distributed on 6 blocks. This grid has been optimized in order to ensure higher skewness among the cells. Also, as we can see on Fig. 4.3b, it provides a smoother behavior at block edges.

2D compressible RANS simulations of a diatomic perfect Newtonian gas are carried out by imposing characteristic boundary conditions at the inlet and outlet boundaries, periodicity conditions at the upper and lower boundary to simulate an infinite cascade and an adiabatic wall condition along the blade surface. The top and bottom boundaries are separated by a distance equal to 0.59 axial chord, that also represents the gap between neighboring blades. At the inlet, the total pressure, enthalpy and angle of attack are prescribed, whereas a constant static pressure is enforced at the outlet.

The inviscid fluxes for both the conservative variables and turbulent quantities are approximated by means of Roe's upwind scheme with second-order MUSCL extrapolation, and a five-point second-

order approximation is used for the viscous fluxes. To obtain physical solutions of the problem, it is necessary to recover the Roe scheme compatibility with the entropy condition. To this end, the eigenvalues of the Jacobian matrix are corrected where they are close to zero, using the so-called Harten correction. Furthermore, to avoid possible spurious oscillations (wiggles) that would otherwise occur with second-order spatial discretization schemes due to shocks, discontinuities or sharp changes in the solution domain, we use a minmod flux limiter along with our Roe's upwind scheme.

All the RANS simulations presented in this thesis target the steady state flow solutions. However, the CFD solver uses a time that can be considered as an iterative parameter allowing to converge towards a steady solution. The method is then known as "pseudo-unsteady" since it is not necessarily consistent with an unsteady evolution having a physical meaning. The time stepping on this pseudo-time is performed by means of the first-order (implicit) backward Euler scheme. This scheme is then solved by using a robust LU relaxation method: the scalar LU-SSOR, which in general is observed to lead to higher numerical efficiency. The LU-SSOR in *elsA* relies on a method of relaxation which consists in calculating a succession of approximate solutions of the exact (linear) system to be solved. In our case, we consider a number of relaxation cycles equal to 4. The relaxation method has the advantage of allowing a quasi exact resolution of the system by application of a succession of relaxation cycles.

The near-wall grid resolution leads to an average height of the first cell closest to the wall (in wall coordinates) such that $y^+ < 1.0$ on both the suction and the pressure side of the blade. For all computations, we assume that the solution has converged to the steady state when the L_2 norm of the conservative quantities residuals are reduced by six orders of magnitude with respect to their initial value. Simulations that do not meet the required convergence criterion are discarded.

4.2.2 LES reference data

In the third chapter of his PhD Thesis manuscript [4], also published in [7], Leggett presents LES and RANS results for a range of off-design conditions. The simulations are validated against Leipold et al. [103] experimental data. More precisely, Leggett simulated the NACA 65 V103 − 220 cascade at an inlet Mach number $Ma_1 \in [0.65, 0.674]$, an inlet Reynolds number based on the axial chord $Re_1 \in [289000, 302000]$ and 4 values of the angle of attack $\alpha = \beta_1 - 90° = 37°, 40°, 44°$ and $49°$. We call each flow condition a scenario. The inlet Mach numbers, free-stream turbulence level and axial chord

Scenario	S_1	S_2	S_3	S_4
β_1	36.99°	39.97°	44.09°	49.2°
Ma_1	0.654	0.674	0.666	0.65
Re_1	302000	302000	298000	289000
Tu (%)	2.9	3.3	3.2	3.5

Table 4.2: Flow conditions for the NACA 65 V103 – 220 scenarios, from [4].

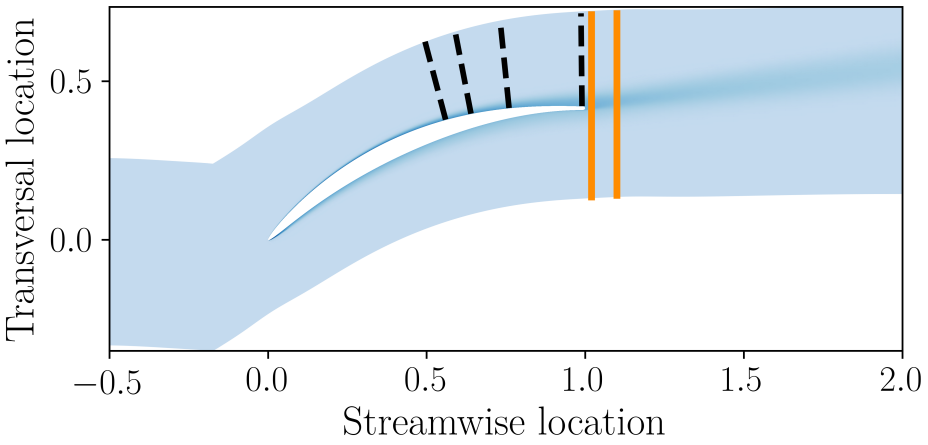

Figure 4.4: Location of the LES profiles from [4].
Tangential velocity profiles (- - -) Total pressure loss profiles (—).

Reynolds numbers corresponding to each scenario are reported in Table 4.2.

For the purpose of model calibration and validation, profiles of various quantities of interest are extracted from Leggett in [4]. More specifically, we selected tangential velocity and turbulent kinetic energy (TKE) profiles in the wall-normal direction and total pressure loss profiles in the wake, where the pressure loss is defined as:

$$\frac{P_{t,inlet} - P_t}{P_{t,inlet} - P_{inlet}}$$

where P and P_t are respectively the pressure and the total pressure.

Tangential velocity and turbulent kinetic energy profiles are taken at streamwise positions $x/l = 0.56, 0.64, 0.76$ and 0.99 along the suction side, l being the chord and $x/l = 0$ corresponding to the leading edge, and total pressure loss profiles are extracted at two positions downstream of the trailing edge ($x/l = 1.02$ and 1.10). The positions of theses profiles are sketched in Fig. 4.4. The TKE profiles are used for the calibration of two-equations RANS models such as $k - \varepsilon$, the $k - l$ and the $k - \omega$ models, as well as for the EARSM $k - kL$ model.

4.2.3 EARSM reference data

The lack of high-fidelity data is one of the usual limitations to the wider use of data-based methods for high-Reynolds flows. In order to overcome this limitation, a more complete data set is generated by means of the EARSM $k-kL$ model for each of the four scenarios presented in Table 4.2.

We could also refer to these data set as synthetic data, since the EARSM $k-kL$ model does not outperform Boussinesq models (in terms of agreement with the LES) for all of the considered flow conditions and quantities of interest. However, since the EARSM model relies on a different constitutive equation, it is expected that it produces a family of solution that does not completely overlap with that spanned by LEVM models, thus mimicking the discrepancy between LEVM solutions and the LES. Additionally, using full fields available from EARSM simulations allows us to control the number and spatial position of data used in the training of a data-based method such as the XBMA presented in Chapter 6, and to investigate the sensitivity of the method to such parameters. On the other hand, the use EARSM-generated reference data in place of high-fidelity data will naturally reduce the significance of any physical interpretations of the results obtained with such method. Any discussion concerning the ability of a Boussinesq model to capture a physical property of the flow, like a detachment of the boundary layer for example, after training on EARSM data could be challenged. Instead, the results obtained after training on EARSM data sets should be regarded as a demonstration of the predictive capabilities of the method, provided that some high-fidelity or experimental data are made available.

4.3 Chapter summary

In this chapter, we described the reference data used for model calibration and validation in the rest of the study. First, we describe one reference data set that was previously used in the calibration of RANS models in [3]. The data set is composed of a set of 14 flat plate experimental flows originating from the 1968 AFOSR-IFP-Stanford conference, and serve as on-the-shelf calibrations of RANS models. The second configuration corresponds to the NACA 65 V103$-$220 compressor cascade, which is representative of the mid-span section of a stator blade, working at 4 operating conditions. First we assembled a high-fidelity data set on this configuration corresponding to the LES data from Leggett [4]. Then, as this data set was simply not complete enough for our purpose, we constructed

on the same compressor configuration a second data set from the prediction of the EARSM $k - kL$ model. This second reference data set allowed us to investigate the influence of the number of data on the method described in Chapter 6. The numerical settings used for the corresponding RANS calculations are also briefly presented.

In the next chapter, we present and apply the BMSA method on the NACA 65 V103 − 220 configuration.

Chapter 5

Bayesian model-scenario averaging: application to the prediction of compressor cascade flows under uncertain turbulence models

Contents

5.1 Introduction

In the present chapter, we investigate the potential of Bayesian model-scenario averaging (BMSA) for robust predictions of turbomachinery flows under uncertain RANS models. We focus more particularly on the NACA65 V103 compressor cascade described in Chapter 4, for which high-fidelity numerical and experimental data are available in the literature. For this study, we select the five widely used RANS models described in Chapter 2, namely the Spalart–Allmaras, Wilcox' $k-\omega$,

Smith's $k-l$, Launder–Sharma $k-\varepsilon$ and the EARSM $k-kL$ turbulence models. The purpose of the study is manifold: 1) we investigate if BMSA calibrated on canonical external flow configurations like those of [3, 69] may still provide valuable information for the internal flow configuration of interest; 2) we set up a computationally efficient strategy for specifically calibrating BMSA for costly compressor flows; 3) we apply BMSA to the NACA65 V103 compressor flow at operating conditions outside the calibration set, and we assess its capability to provide accurate predictions and the associated uncertainty intervals for new flows. The results are compared to those of BMSA based on the on-the-shelf sets of coefficients [69].

The chapter is organized as follows. In Section 5.2, we present the BMSA framework, and we discuss the choice of the *a priori* scenario probabilities. In Section 5.3, we describe model calibration using surrogate models. In Section 5.4, we report BMSA results for the NACA65V103 cascade at two off-design conditions using three alternative scenario-weighting criteria. Finally, Section 5.5 summarizes the main findings and draws perspectives for future work. The results reported in this chapter have been published in [98, 107].

5.2 Methodology

In this section, we describe the Bayesian calibration strategy for the present CFD models and we recall the Bayesian Model-Scenario Averaging (BMSA) framework, following [3, 69, 70].

5.2.1 Bayesian Model-Scenario Averaging

Predicting a new scenario based on a single model calibrated for a single scenario introduces a bias due to model inadequacy. In BMA (see Chapter 3), the bias due to the model structure is alleviated by averaging the predictions over a set of models. However, such models are calibrated over a single scenario, which can be far apart the configuration we want to predict. In other terms, while BMA reduces the bias due to the choice of model structure, it may still be biased due to an inadequate choice of calibration scenario, causing large errors when applied to a prediction case that is too different from the calibration one. One possibility for reducing such a bias consists in simultaneously calibrating the models over multiple scenarios as, e.g. in [16]. Nevertheless, this causes the calibration process

to select coefficients providing the best compromise, in terms of fit to the data, among the multiple scenarios, without necessarily providing a very accurate solution for any of the scenarios. This effect has been discussed in [70] for the case of compressible flow predictions using real-gas equations of state, where BMSA of models calibrated individually over various scenarios is shown to overperform BMA of the same models with coefficients calibrated on several scenarios simultaneously.

Similarly to BMA, BMSA considers a set of competing models $\mathcal{M} = \{M_1, .., M_m, .., M_{N_M}\}$, calibrated for a set of scenarios $\mathcal{S} = \{S_1, .., S_s, .., S_{N_S}\}$ for which we have N_S vectors of observed data $\mathcal{D} = \{\overline{\boldsymbol{\delta}}_1, ..., \overline{\boldsymbol{\delta}}_s, .., \overline{\boldsymbol{\delta}}_{N_S}\}$. The kind and number of data may be different for each scenario. For each model M_m, applied to each scenario S_s, we assume that the calibration phase resulted in $N_M \times N_S$ posteriors for $\boldsymbol{\theta}$:

$$\boldsymbol{\theta}_{m,s} \sim \boldsymbol{\theta} | \mathcal{M} = M_m, \mathcal{S} = S_s, \mathcal{D} = \overline{\boldsymbol{\delta}}_s \tag{5.1}$$

Afterwards, let us consider a new scenario S' with no available data for which we wish to predict a QoI Δ, not necessarily equal to the variables observed in the calibrations. Similarly to [22], we use the law of total probabilities to write the posterior predictive distribution of Δ based on the selected model set $\mathcal{M}$ and the available posteriors:

$$f\left(\Delta | S', \mathcal{M}, \mathcal{S}, \mathcal{D}\right) = \sum_{m=1}^{N_M} \sum_{s=1}^{N_S} f\left(\Delta | S', M_m, S_s, \overline{\boldsymbol{\delta}}_s\right) p\left(M_m | S_s, \overline{\boldsymbol{\delta}}_s\right) p\left(S_s\right) \tag{5.2}$$

Here, $f\left(\Delta | S', M_m, S_s, \overline{\boldsymbol{\delta}}_s\right)$ represents the distribution of Δ obtained by propagating the posterior distribution $\boldsymbol{\theta}_{m,s}$ (calibrated from data available for S_s) through model M_m, applied to the new scenario S'; $p\left(M_m | S_s, \overline{\boldsymbol{\delta}}_s\right)$ is the posterior probability of model M_m based on the data observed for S_s. Finally, $p\left(S_s\right) = p\left(S_s | \overline{\boldsymbol{\delta}}_s\right)$ is the scenario probability, *i.e.* the probability that S_s is relevant to make predictions for the unseen scenario S'. We assume that S_s and $\overline{\boldsymbol{\delta}}_s$ are independent, *i.e.* that the observed data do not affect the probability assigned to the scenario, see [57, 61] for a more detailed discussion. The distribution (5.2) can be used to compute the statistical moments of Δ. Specifically, the two leading moments of $f\left(\Delta | S', \mathcal{M}, \mathcal{S}, \mathcal{D}\right)$, *i.e.* the expectancy and the variance of Δ are:

$$E\left[\Delta | S', \mathcal{M}, \mathcal{S}, \mathcal{D}\right] = \sum_{m=1}^{N_M} \sum_{s=1}^{N_S} E\left[\Delta | S', M_m, S_s, \overline{\boldsymbol{\delta}}_s\right] p\left(M_m | S_s, \overline{\boldsymbol{\delta}}_s\right) p\left(S_s\right) \tag{5.3}$$

$$
\begin{aligned}
Var\left[\Delta|S',\mathcal{M},\mathcal{S},\mathcal{D}\right] = & \underbrace{\sum_{m=1}^{N_M}\sum_{s=1}^{N_S} Var\left[\Delta|S',M_m,S_s,\overline{\boldsymbol{\delta}}_s\right] p\left(M_m|S_s,\overline{\boldsymbol{\delta}}_s\right) p\left(S_s\right)}_{\textit{within-model, within-scenario variance}} \\
& + \underbrace{\sum_{m=1}^{N_M}\sum_{s=1}^{N_S} \left(E\left[\Delta|S',M_m,S_s,\overline{\boldsymbol{\delta}}_s\right] - E\left[\Delta|S',\mathcal{M},S_s,\overline{\boldsymbol{\delta}}_s\right]\right)^2 p\left(M_m|S_s,\overline{\boldsymbol{\delta}}_s\right) p\left(S_k\right)}_{\textit{between-model, within-scenario variance}} \\
& + \underbrace{\sum_{s=1}^{N_S} \left(E\left[\Delta|S',\mathcal{M},S_s,\overline{\boldsymbol{\delta}}_s\right] - E\left[\Delta|S',\mathcal{M},\mathcal{S},\mathcal{D}\right]\right)^2 p\left(S_s\right)}_{\textit{between-scenario variance}}
\end{aligned}
\tag{5.4}
$$

In Eq. (5.4) the variance $Var\left[\Delta|S',\mathcal{M},\mathcal{S},\mathcal{D}\right]$ is decomposed in three contributions: the first one is related to the uncertainty in model parameters, and results from the fact that Δ is obtained by propagating through model M_m the posterior pdf $\boldsymbol{\theta}_{m,s}$ obtained in the calibration phase for scenario S_s: for this reason, it is called the *within-model, within-scenario* variance. The second term represents the *between model, within scenario* variance, *i.e.* the fact that the competing models in $\mathcal{M}$, calibrated for a same scenario S_s and applied to S', release different predictions. The last term, called *between scenario* variance, reflects the fact that using different calibration scenarios results in different posteriors for $\boldsymbol{\theta}_{m,s}$ and in different model probabilities $p\left(M_m|S_s,\overline{\boldsymbol{\delta}}_s\right)$. This ultimately leads to different predictions for $\Delta|S'$.

The term $E\left[\Delta|S',\mathcal{M},S_s,\overline{\boldsymbol{\delta}}_s\right]$ in Eq. (5.4) represents the average of Δ over all models when using posteriors calibrated on the same scenario. It is computed through the law of total probabilities:

$$
E\left[\Delta|S',\mathcal{M},S_s,\overline{\boldsymbol{\delta}}_s\right] = \sum_{m=1}^{N_M} E\left[\Delta|S',M_m,S_s,\overline{\boldsymbol{\delta}}_s\right] p\left(M_m|S_s,\overline{\boldsymbol{\delta}}_s\right) \tag{5.5}
$$

The term $E\left[\Delta|S',\mathcal{M},\mathcal{S},\mathcal{D}\right]$ appearing in Eq. (5.3) is the average of Eq. (5.5) over all scenarios:

$$
E\left[\Delta|S',\mathcal{M},\mathcal{S},\mathcal{D}\right] = \sum_{s=1}^{N_S} E\left[\Delta|S',\mathcal{M},S_s,\overline{\boldsymbol{\delta}}_s\right] p\left(S_s\right)
$$

The posterior model probabilities $p\left(M_m|S_s,\overline{\boldsymbol{\delta}}_s\right)$ reflect how well the model M_m fits the data $\overline{\boldsymbol{\delta}}_s$ for the scenario S_s. It can be computed through Bayes' rule :

$$
p\left(M_m|\overline{\boldsymbol{\delta}}_s,S_s\right) = \frac{f\left(\overline{\boldsymbol{\delta}}_s|M_m,S_s\right) p\left(M_m|S_s\right)}{\sum_{j=1}^{N_M} f\left(\overline{\boldsymbol{\delta}}_s|M_j,S_s\right) p\left(M_j|S_s\right)} \tag{5.6}
$$

where $p\left(M_m|S_s\right)$ is a user-defined prior and $f\left(\overline{\boldsymbol{\delta}}_s|M_m,S_s\right)$ is the evidence for model M_m and scenario S_s. For BMSA, the denominator of Bayes' rule is no longer ignored and is calculated as follows:

$$p\left(\overline{\boldsymbol{\delta}}_s|M_m,S_s\right)=\int_{\boldsymbol{\theta}_m} f\left(\overline{\boldsymbol{\delta}}_s|\boldsymbol{\theta}_m,M_m,S_s\right) f\left(\boldsymbol{\theta}_m|M_m,S_s\right) d\boldsymbol{\theta}_m \tag{5.7}$$

and computed through a Monte Carlo algorithm. Finally, the prior model probability mass function $p\left(M_m|S_s\right)$ is generally chosen equiproportional, *i.e.* $p\left(M_m|S_s\right)=1/N_M$.

The BMSA formulation is completed by selecting a prior probability mass function for the scenarios, *i.e.* an expression for $p\left(S_s\right)$. Several formulations are likely to be chosen leading potentially to radically various predictions.

5.2.2 Prior scenario probability models

The role of the scenario probability is to assign a higher probability to calibration scenarios more likely to provide an accurate estimate of model coefficients with respect to the new predicted scenario S'. For that purpose, we evaluate three different formulations proposed in the literature for $p\left(S_s\right)$.

5.2.2.1 Agreement-based criterion

First, we choose a scenario probability based on model agreement, as described in [88], *i.e.* a criterion which rewards scenarios for which all models give similar predictions:

$$\begin{cases} p\left(S_s\right)=\dfrac{\varepsilon_s^{-2}}{\sum_{s=1}^{N_S}\varepsilon_s^{-2}} \\ \varepsilon_s=\displaystyle\sum_{m=1}^{N_M}\left|\left|E\left[\Delta|S',M_m,S_s,\overline{\boldsymbol{\delta}}_s\right]-E\left[\Delta|S',\mathcal{M},S_s,\overline{\boldsymbol{\delta}}_s\right]\right|\right|_2 \end{cases} \tag{5.8}$$

In most cases, such a criterion tends to assign higher weights to scenarios that are the more similar to the prediction one. However, it may provide wrong information in the case all models provide a similar but wrong prediction. This risk may be reduced by including in the mixture sufficiently diverse models and scenarios. Another drawback is that the criterion is an "a posteriori" error measure: it requires to propagate all the posterior pdfs for each model and scenario while only a few of them may have a scenario probability close to zero leading to useless computational efforts.

5.2.2.2 Calibration-driven criterion

In order to reduce the computational cost of BMSA predictions, it is interesting to consider a scenario weighting criterion that allows to exclude "a priori" scenarios that are assigned low probability (below a user-defined threshold). Hereafter we consider the scenario weighting criterion proposed in [70], which takes into account the hyper-parameter σ_η, a measure of model inadequacy, as mentioned in Chapter 3:

$$\begin{cases} p\left(S_s\right) = \dfrac{\varepsilon_s^{-1}}{\sum_{s=1}^{N_S} \varepsilon_s^{-1}} \\ \varepsilon_s = \displaystyle\sum_{m=1}^{N_M} \varepsilon_{m,s} p\left(M_m | S_s, \overline{\boldsymbol{\delta}}_s\right) \\ \varepsilon_{m,s} = \left|\left| E\left[\Delta_{m,s}\right] - \overline{\boldsymbol{\delta}}_s \right|\right|_2 + E\left[\sigma_\eta^{m,s} | \overline{\boldsymbol{\delta}}_s, S_s, M_m\right] \end{cases} \tag{5.9}$$

where $\Delta_{m,s}$ is the posterior predictive distribution of Δ for the model M_m and the scenario S_s. The criterion (5.9) tends to penalize scenarios for which the model do not match well the data after calibration, or for which the data could be captured by introducing a large model-inadequacy term η.

5.2.2.3 Naive criterion

Finally, we also consider a naive expression for $p\left(S_s\right)$, which simply computes a distance between the scenarios S_s and S' in the space of operating conditions. These operating conditions are noted ϕ_t, and collected in a vector of $\mathbb{R}^{N_\phi}$, with N_ϕ the dimension of the operating condition space.

$$\begin{cases} p\left(S_s\right) = \dfrac{\varepsilon_s^{-1}}{\sum_{s=1}^{N_S} \varepsilon_s^{-1}} \\ \varepsilon_s = \left| \displaystyle\sum_{t=1}^{N_\phi} \left(\frac{\phi_t(S') - \phi_t(S_s)}{\max\limits_{1 \le j \le N_S} \left(\phi_t(S') - \phi_t(S_j)\right)} \right)^2 \right|^{1/2} \end{cases} \tag{5.10}$$

In the following, the flow operating conditions are defined by assigning the flow Mach number M_a, the Reynolds number R_e and the cascade inlet angle α; therefore $N_\phi = 3$. This criterion is the most restrictive one, as it can be applied only to scenarios that can be described by the same type of operating conditions.

5.3 Calibration data

In this chapter we use the LES reference data from [4] presented in the previous Chapter 4. For the purpose of calibration, we use 8, 9 and 8 probes to sample each velocity, pressure and TKE profile,

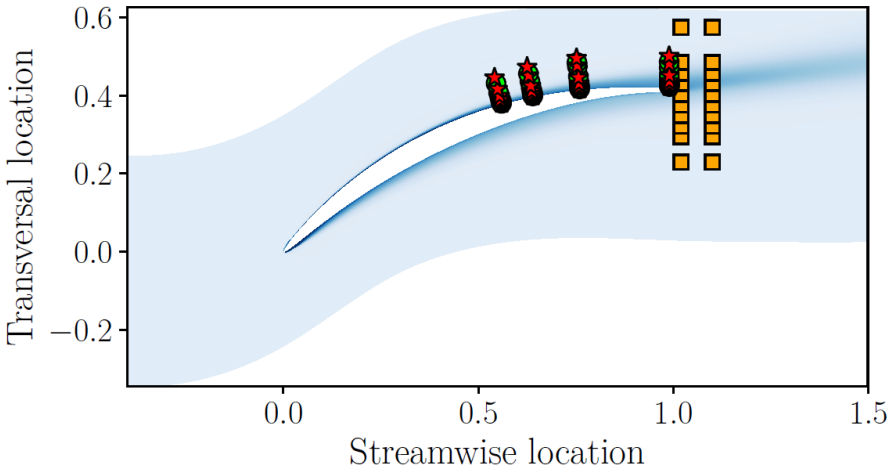

Figure 5.1: Location of the LES probes drawn from [4].
(●) Tangential velocity, (★) Turbulent kinetic energy, (■) Total pressure loss.

respectively. In total, this leads to $N_{\tilde{\boldsymbol{\delta}}} = 82$ or $N_{\tilde{\boldsymbol{\delta}}} = 50$ observed data, depending on whether TKE is included or not. The position of the probes are presented in Fig. 5.1. Note that using large observation vectors increases the computational cost associated with the inversion of the correlation matrix $\mathbf{K}$ at each iteration of the MCMC algorithm. On the other hand, using too few observations leads to poorly informed posterior distributions. As a consequence, the number of data used in the calibration is a trade-off between the necessity of informing the model coefficients and the computational cost associated with the construction and inversion of the correlation matrix involved in the likelihood function. In the present calculations, we chose an uncorrelated error model and the covariance $\mathbf{K}$ is a diagonal matrix, easy to invert. This allows using a rather large data set.

Although a systematic study of the effects of the quantity and location of the data on the calibration results is beyond the scope of the present thesis, we note that no significant differences on the posteriors is observed when the vector of data is increased up to 120, showing that the posteriors are already rather well informed. Furthermore, the placement of observation probes was chosen based on the available LES results and expert judgement. Optimal sample placement is an active research subject (see, e.g., the works of Papadimitriou et al. [108] and Mons at al. [109]), and could be considered in future research work.

Finally, the statistical model used in the calibration procedure also requires information about the

observation error e, *i.e.* the difference between the observed data and the "truth". Since no information is available for the LES data used in this study, except that the LES simulations are numerically well resolved, we assign the observation error a small standard deviation σ_e (1 % of the observed value). We verified that the calibration results are little affected by this choice, since our statistical model also includes a model inadequacy term with a free hyper-parameter σ_η which is calibrated from the data. Such error terms tend to compensate each other. Numerical tests, not reported here for brevity, show that increasing σ_e up to 5 % do not modify the posteriors of the model coefficients significantly, but simply results in smaller values for σ_η.

5.4 Results

In this section we first report the outcome of the Bayesian calibration of turbulence model parameters for the compressor cascade scenarios. Afterwards, we present various BMSA predictions for two of selected compressor scenarios, using coefficients calibrated for different scenarios.

5.4.1 Calibration Results

The statistical calibration framework of Chapter 3 is first used to infer posterior distributions of the RANS coefficients $\boldsymbol{\theta}_m$ for the five models considered in this study - namely the Spalart–Allmaras, Wilcox' $k-\omega$, Smith's $k-l$, Launder–Sharma $k-\varepsilon$ and the EARSM $k-kL$ turbulence models - and the LES calibration data relative to the four NACA 65 V103 – 220 scenarios described in Section 5.3.

First, we evaluate the quality of the surrogates models, for each model and scenario, by computing the Q^2, as described in Chapter 3. The mean value and the standard deviation of the Q^2 criterion over the various QoIs are presented in Table 5.1. The values being greater than 0.96 for all models and scenarios, with standard deviation that does not exceed 5% of the average in most cases, the surrogates should deliver a sufficient accuracy for the calibration step.

Average Q^2	$k-\varepsilon$	$k-\omega$	Spalart–Allmaras	$k-l$	EARSM $k-kL$
S_1	0.976	0.991	0.975	0.961	0.966
S_2	0.967	0.968	0.965	0.986	0.969
S_3	0.995	0.997	0.970	0.987	0.977
S_4	0.996	0.985	0.994	0.975	0.973

Table 5.1: Average values of Q^2 over the considered QoIs for the 5 models and 4 scenarios.

For each model and scenario, we then assign to the closure coefficients non-informative uniform marginal prior distributions, ranging from 10 % to 300 % of the standard values from the literature. Eventually, such large ranges must be restricted for computational stability reasons, *i.e.* to prevent non-convergence of the CFD solver when using too large or too small values of the coefficients. The final prior ranges are the largest ensuring numerical stability. The hyper-parameter σ_η is assigned an uniform prior in the range $[0, 1]$ for all cases. As an example, the prior ranges assigned to the closure coefficients of the Spalart–Allmaras model for scenario 3 are reported in Table 5.2.

Closure Coefficient	Lower bound	Upper bound
κ	0.36	0.56
C_{w2}	1.0	2.4
C_{w3}	0.1	0.9
C_{v1}	6.5	18.0
C_{b1}	0.5	1.5
C_{b2}	0.06	0.16
σ	0.6	2.0

Table 5.2: Lower and upper bounds for the uniform marginal priors assigned to the Spalart–Allmaras closure coefficients for the scenario 3.

Fig. 5.2a shows typical calibration results for the κ coefficient of the Spalart–Allmaras model. As also observed in [88], this coefficient is well informed by the data but is highly sensitive to the calibration scenario. It can be noticed that calibration may assign high probabilities to values of κ that are very different from the standard value 0.41, especially for off-design scenarios farthest from the nominal conditions. The modified values of the Von Karman κ constant, or other coefficients, do not affect the numerical convergence of the CFD solver because of the careful choice of the prior distributions. Large variations of the Von Karman constant are also found for the other models under consideration. However, κ has a different meaning and influence with respect to the model and thus should not be

confused with any model-independent, or "true", Von Karman constant. Nonetheless, κ should ideally be independent of scenario for a given model. The present results clearly show statistically significant variation in calibrated coefficients across scenarios, in accordance with the results obtained in [3] for flat plate boundary layers. Similar large variations across scenarios are also found for other model coefficients, thus reminding us that the standard closure parameters in RANS models are often chosen as a trade-off for a large range of flows, and therefore suboptimal for one specific class of flows such as turbomachinery flows. For instance, the MAP of C_μ and the β^* coefficients of the $k-\varepsilon$ and $k-\omega$ models, which control the eddy viscosity, are greater or equal than the nominal values for all scenarios except S_4, for which a separated region is present. In this case, calibration leads to somewhat lower values to enable a larger separation bubble size. This result has important consequences for BMSA predictions of S_4. We report in the Appendix (tables A.1 to A.5) the MAP estimates after calibration for each model and scenario, alongside nominal values from the literature.

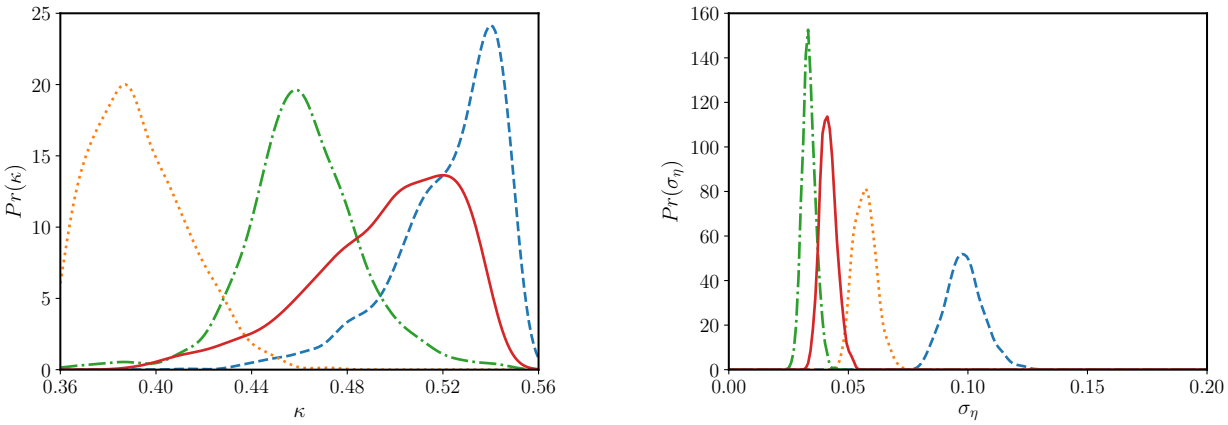

(a) Coefficient κ.

(b) Hyper-parameter σ_η.

Figure 5.2: Posterior probabilities in case of Spalart–Allmaras model: Scenario 1 (- - -), Scenario 2 (·····), Scenario 3 (-·-·-) and Scenario 4 (——).
Priors has been chosen uniform on $[0.36, 0.56]$ and $[0, 1]$ respectively.

In Fig. 5.2b, we present calibration results for the model-inadequacy hyper-parameter σ_η applied to the Spalart–Allmaras model. This hyper-parameter is well informed by the data. As mentioned in Chapter 3, σ_η can be interpreted as a measure of model accuracy in the calibration scenario. It is worth noting that the posterior mean of σ_η is smaller than 0.10 for each scenario. This shows that the data scarcely differs from the predictions of the models after calibration.

In the end, the calibration step delivered posterior parameter distributions $\boldsymbol{\theta}_{i,k}$ specifically trained for NACA 65 cascade configurations. The next step is then to propagate those posteriors for new unseen scenarios.

5.4.2 BMSA prediction with 3 linear eddy viscosity models

In this section, we use BMSA based on the first scenario weighting criteria (5.8) to predict NACA65 V103 flows. In order to compare the effect of calibration compared to on-the-shelf parameter distributions, we restrict our attention to the three linear eddy viscosity models Spalart–Allmaras, $k-\omega$ and $k-\varepsilon$, which were calibrated by Edeling et al. [3] against flat plate flows.

In order to assess the capability of predicting flows outside the set of calibration scenarios $\mathcal{S}$, we do not use the data available for the prediction scenarios. These are only used for validation purposes. In the following of this section, we focus on a vector of prediction QoIs consisting of a profile of the tangential velocity (normalized with the maximum velocity for each profile) and one of the normalized total pressure loss at prescribed locations among those used in the calibration step. These QoIs are then a subset of the calibration variables, for which surrogate models are already available. This allows to propagate the full posteriors across the prediction scenario, but only for the QoI and locations for which a Kriging surrogate is available. Another option would be to construct, e.g., Kernel Density Estimate (KDE) or other approximations of the posteriors using known pdf, and then use a polynomial chaos method for propagating them through the RANS solver and getting posterior predictive estimates of any QoI at any flow location. This approach is however costly due to the high number of uncertain variables to be propagated. Here we retain MAP approximations of the posteriors and examine the pros and cons of such a choice in terms of accuracy, computational cost, and possibility of predicting a large variety of flow quantities.

S_2 and S_4 are first considered as prediction scenarios. For S_2, the flow remains attached all over the suction side of the blade, whereas a flow separation is observed in S_4. The dynamics are very different for the other scenarios in the database. Making predictions for S_2 and S_4 thus comes to assessing BMSA far outside the training set. To evaluate the influence of the calibration scenarios on the pre-

diction, we form three different BMSA models, each using posteriors calibrated for a specific ensemble of scenarios. First, a baseline BMSA model, noted $BMSA_1$, is constructed by propagating the MAP estimates of the model coefficients and the model posterior probabilities $p\left(M_m|S_s,\overline{\boldsymbol{\delta}}_s\right)$ provided in [69]. Although such coefficients were obtained for flat plate flows, we may expect that the thin NACA 65 $V103$ blades can be approximately modeled as flat plates subject to a variable (mostly adverse) pressure gradient. It is then interesting to measure the capability of BMSA to predict the present compressor cascade before having observed any data for this family of configurations. In the following, the flat-plate scenarios are noted S_{WXYZ}, with WXYZ the four-digit code presented in Chapter 4, more specifically in Table 4.1. Afterwards, another BMSA model, noted $BMSA_2$, is developed by propagating the full posterior distributions calibrated on NACA 65 configurations. For each prediction scenario, a $BMSA_2$, model is constructed by using posteriors for the three remaining scenarios. For instance, we use posteriors obtained for scenarios S_1, S_3 and S_4 to predict scenario S_2. Two strategies are tested for the prediction: on one hand the full parameter posteriors are propagated by using the Kriging surrogate models built for the calibrations and, on the other hand, only the MAP estimates of the posteriors $\boldsymbol{\theta}_{m,s}$ are propagated. Finally, a more general BMSA model, named $BMSA_3$, is constructed by mixing together flat plate scenarios and the S_1, S_2 and S_3 NACA 65 scenarios and then applied to the prediction of S_4 . For $BMSA_3$, only MAP approximations are used.

The construction of BMSA models necessitates the calculation of posterior model probabilities (Eq. (5.6)) which in turn are computed from the evidences in the Bayes' rule for each model and calibration scenario considered in the BMSA. We use model probabilities given in [69] for the flat plate scenarios (after renormalization for the present model set) and we compute model probabilities for the compressor scenarios following the procedure described in Section 5.2.1. The model probabilities for the compressor scenarios are reported in Table A.6 of the Appendix for assessment and future use. Finally, the scenario probabilities $p\left(S_s\right)$ are assigned by using the agreement based criterion presented in Eq. (5.8).

In the rest of this chapter, we present BMSA prediction in blue color, with 1 and 2-standard deviation confidence interval in lighter shades of blue. Red color is reserved for the LES reference data from [4]. Black, green and orange colors are used respectively for the baseline $k-\omega$, $k-\varepsilon$ and

Spalart–Allmaras models, with the nominal closure coefficients as reported in Chapter 2.

5.4.2.1 BMSA prediction for S_2

We first report the results of the BMSA of the NACA 65 $V103$ configuration at mildly off-design conditions, namely the scenario S_2. The results are discussed for selected velocity and total pressure profiles, representative of typical BMSA predictions. However, similar considerations hold for other locations in the flow.

We present in Figure 5.3 the prediction (left pannel) and variance decomposition (right pannel) for the tangential velocity profile at $x/l = 0.99$. The y-axis represents the normalized distance to the wall y_n/l, y_n being the distance to the blade. The results are based on the baseline model $BMSA_1$ (Fig. 5.3a), $BMSA_2$ where only MAP estimates are propagated (Fig. 5.3b) and $BMSA_2$ for which the full posteriors are propagated (Fig. 5.3c). Regarding the $BMSA_2$, the predictions for S_2 are based on the calibrations on $\{S_1, S_3, S_4\}$. Predictions of the baseline RANS models are also reported for comparison. It turns out that significant differences arise, even for the present attached 2D flow. The baseline $k-\omega$ and Spalart–Allmaras models provide rather close predictions, in better agreement with the LES data than the baseline $k-\varepsilon$ model, which performs noticeably worse for this case.

The $BMSA_1$ model does not yield better results than the best baseline model but performs much better than the worst one. Nonetheless, the 2-standard deviation confidence interval on the prediction encompasses rather well the reference data, except in the region closest to the wall. This is related to the scenario weighting criterion, as discussed later. On the other hand, the predictive accuracy of $BMSA_2$, based on the propagation of MAP estimates, improves significantly over $BMSA_1$, thanks to the use of posteriors calibrated for scenarios closer to the prediction one. In particular, the mean prediction $E[\Delta|S']$ is significantly better than the best RANS model, and the reference data are now captured within the 1-standard deviation confidence interval. Finally, the propagation of the full posterior distributions improves even more the predictions. However, the increase of accuracy entails a non-negligible extra computational cost because the propagation requires building new surrogate models for each QoI to be predicted, for each model involved in the mixture, at any point $\mathbf{x}$ for the new scenario S'.

Let us now focus on the variance decomposition associated with each prediction. The right side of

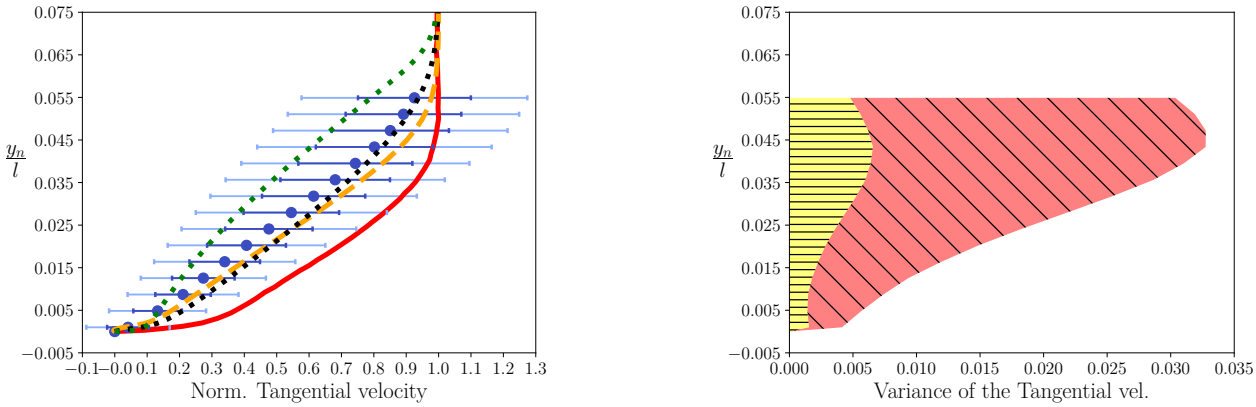

(a) MAP estimates calibrated on flat-plate from [69] ($BMSA_1$).

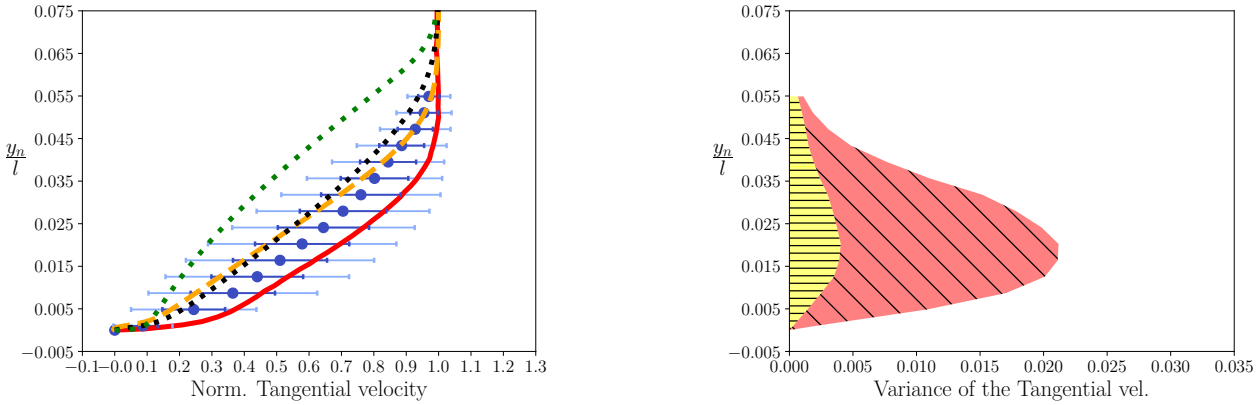

(b) MAP estimates obtained on $\mathcal{S} = \{S_1, S_3, S_4\}$ ($BMSA_2$).

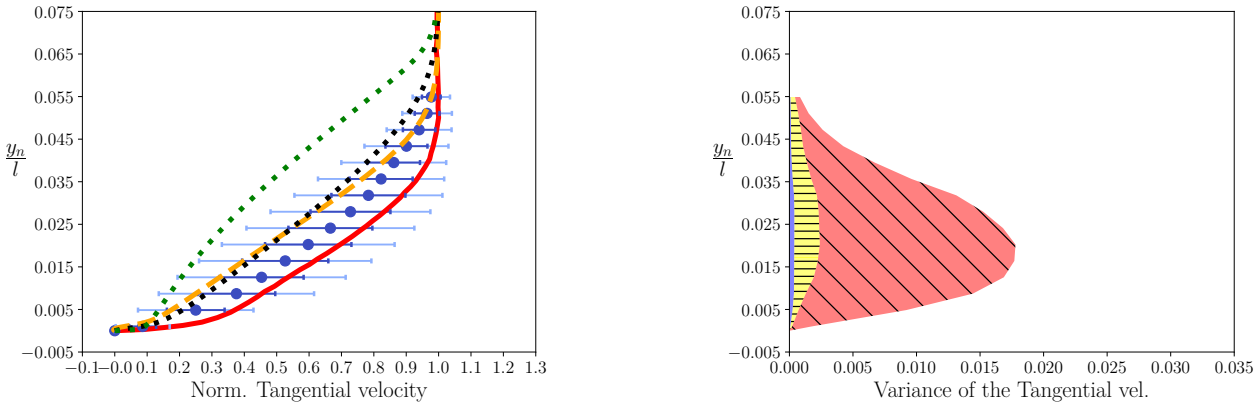

(c) Complete distributions obtained on $\mathcal{S} = \{S_1, S_3, S_4\}$ ($BMSA_2$).

Figure 5.3: Prediction (left) and decomposition of the variance (right) for the normalized tangential velocity profile on the suction side at $x/l = 0.99$ for scenario 2.
(- - -), Left: LES data from Leggett *et al.* [7] (—), $E[\Delta|S'] \pm \sqrt{Var[\Delta|S']}$ (—●—), $E[\Delta|S'] \pm 2\sqrt{Var[\Delta|S']}$ (—●—), Baseline $k-\omega$ (·····), Baseline Spalart–Allmaras (- - -) and Baseline $k-\varepsilon$ (-·-·-).
Right: ■ *within-model, within scenario variance*, ■ *between models, within scenario variance* and ■ *between scenario variance.*

Fig. 5.3 shows the variance decomposition according to Eq. (5.4), for each prediction of the tangential velocity presented on the left side. The total variance for $BMSA_1$ appearing in Fig. 5.3a is larger than for the other two cases, due to the greater diversity of scenarios included in the model. The wall-normal locations associated with the largest variance are close to the boundary layer edge in this case, whereas they are located in the near-wall region for $BMSA_2$ predictions, either using full posteriors or MAP estimates. A possible explanation is that the flat-plate scenarios used in $BMSA_1$ mostly differ in the wake region. As a consequence, the calibration mostly adjusts the coefficients to fit velocity profiles in the outer part of the boundary layer. On the contrary, for NACA 65 scenarios the near wall region is found to be the most sensitive to the RANS model. As expected, the *within-model, within scenario* variance is strictly equal to zero for the MAP-based BMSA models. However, inspection of the right side of Fig. 5.3c shows that this term is very small when propagating the full posteriors of the parameters. The reason is that the latter are rather peaked (*i.e.* not too different from a Dirac function), since the model coefficients are well informed from the data. The residual parametric uncertainty is then small compared to the *between-model, within scenario* uncertainty. On the other hand, the total variance of the MAP-based $BMSA_2$ model (Fig. 5.3b) is comparable to the one of the full $BMSA_2$ or slightly larger. The discrepancy is due to the different scenario weighting in the two cases, as discussed below. Overall, these results further support the choice of MAP estimates for BMSA predictions. To complete the discussion of this figure, we also observe that the larger contribution to the variance is due to the *between scenarios* component. As discussed in the above, the posteriors of the parameters are highly dependent on the calibration scenario. A high *between scenarios* variance indicates that the uncertainty associated with the calibration of the closure coefficients for different scenarios is larger than the model-form uncertainty.

In order to measure the improvement deriving from the calibration of the RANS models for the prediction scenarios, we report in Fig. 5.4 the results of a BMSA of the three RANS models calibrated on S_2. Since only one scenario is considered, the BMSA becomes a simple BMA. As expected, calibration for the prediction scenario further improves the solution, that is now very close to the reference LES data, and reduces the error bars, due to the good agreement of models calibrated for the same scenario.

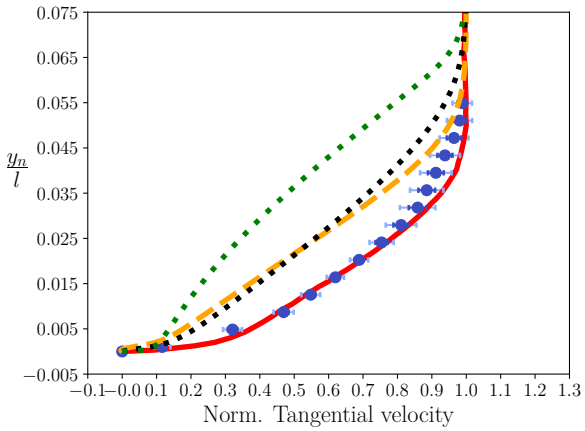

Figure 5.4: BMA prediction of the normalized tangential velocity profile on the suction side at $x/l = 0.99$ for scenario 2.

BMSA predictions of a normalized total pressure profile in the compressor wake are presented in Fig. 5.5. The BMSA predictions are plotted on the left pannel while the variance decompositions are on the right. Results are reported again for $BMSA_1$ and for $BMSA_2$ based on full posterior distributions and MAP estimates of the closure coefficients. The y-axis represents the normalized cross flow position y/l; the origin is aligned with the trailing edge.

For this QoI, the BMSA model predictions exhibit a trend similar to the velocity profiles. The $BMSA_1$ model predicts a wake profile relatively close to the best performing nominal RANS model, with LES reference data falling within the 2-standard deviation confidence interval from the prediction. For the right-hand side of the profile, corresponding to a flow coming from the suction side (characterized by a more challenging physics), $BMSA_1$ still improves over the nominal models but with higher standard deviations than for the rest of the profile. The $BMSA_2$ model using MAP estimates (Fig. 5.5b) provides results in very good agreement with the reference data, especially for the peak and the left-hand side of the profile. So are the $BMSA_2$ results based on the full posteriors (Fig. 5.5c). In fact, the right side of Fig. 5.5 again shows that the contribution of the parametric uncertainty (*i.e.* to the variability of the parameters for a fixed model and scenario) to the total variance is very small, which justifies the use of MAPs.

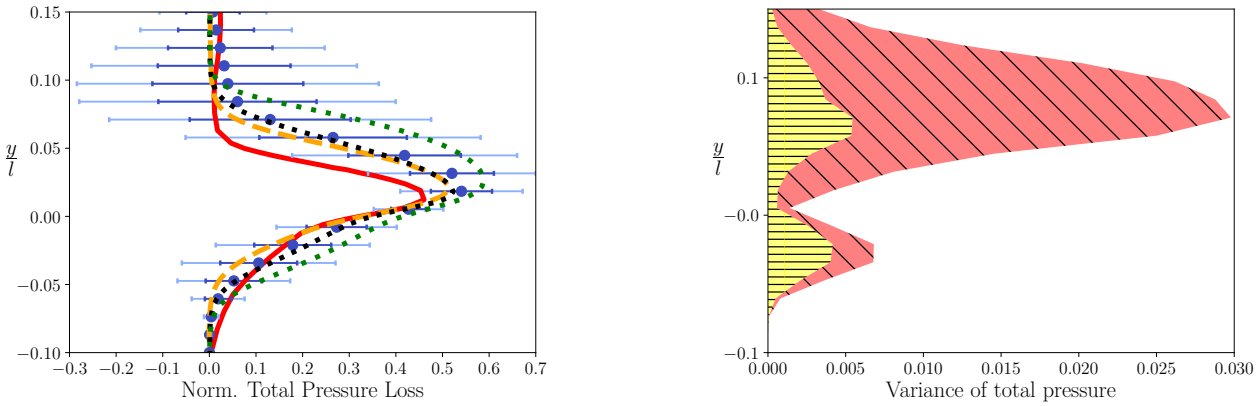

(a) MAP estimates calibrated on flat-plate from [69] ($BMSA_1$).

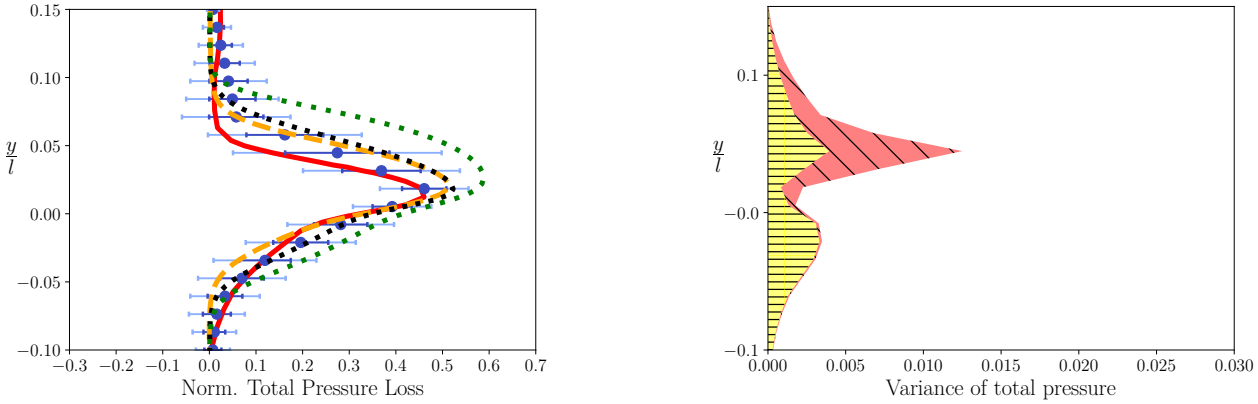

(b) MAP estimates obtained on $\mathcal{S} = \{S_1, S_3, S_4\}$ ($BMSA_2$).

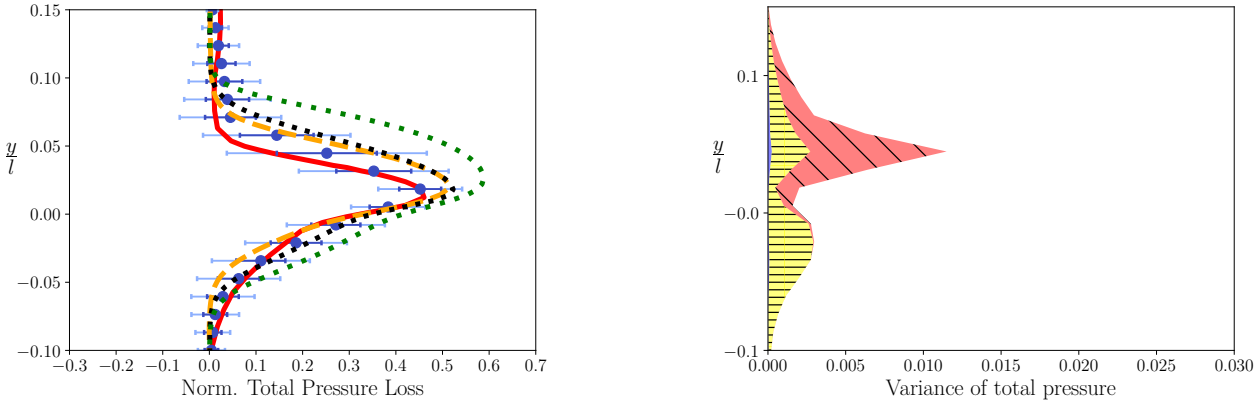

(c) Complete distributions obtained on $\mathcal{S} = \{S_1, S_3, S_4\}$ ($BMSA_2$).

Figure 5.5: Prediction (left) and decomposition of the variance (right) for the normalized pressure wake profile at $x/l = 1.10$ for scenario 2.
Left: LES data from Leggett *et al.* [7] (—), $E[\Delta|S'] \pm \sqrt{Var[\Delta|S']}$ (—●—), $E[\Delta|S'] \pm 2\sqrt{Var[\Delta|S']}$ (—●—), Baseline $k-\omega$ (·····), Baseline Spalart–Allmaras (- - -) and Baseline $k-\varepsilon$ (-·-·-).
Right: ■ *within-model, within scenario variance*, ■ *between models, within scenario variance* and ■ *between scenario variance*.

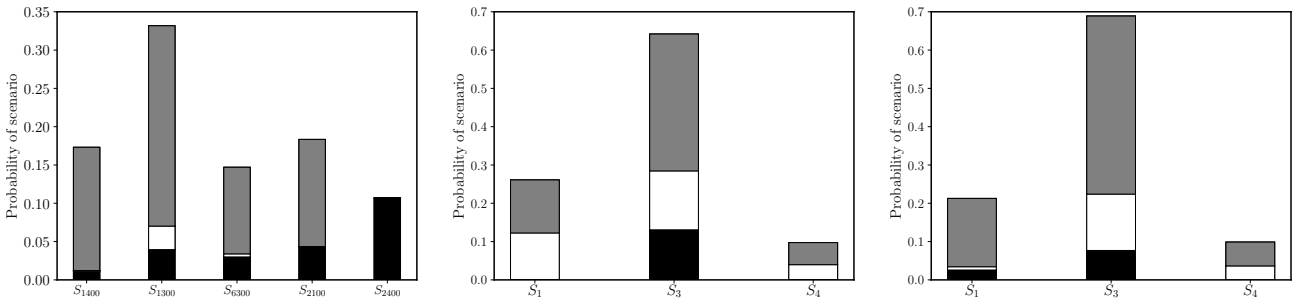

(a) MAP coefficients calibrated on flat-plate [69] ($BMSA_1$).

(b) Obtained with the MAP of the distributions on $\mathcal{S} = \{S_1, S_3, S_4\}$ ($BMSA_2$).

(c) Obtained with complete distributions on $\mathcal{S} = \{S_1, S_3, S_4\}$ ($BMSA_2$).

Figure 5.6: Distribution of $p(S_s)$ and $p\left(M_m|\overline{\boldsymbol{\delta}}_k, S_s\right)$ in case of scenario 2. Only scenarios with probability superior to 5% are shown on Figure 5.6a. Each bar sums to the probability of the scenario. Each probability of scenario is then decomposed into probabilities of models, given this scenario. $k-\varepsilon$ (■), $k-\omega$ (□) and Spalart–Allmaras (▩).

Finally, in Fig. 5.6, we compare the scenario weighting for the various BMSA models. Only the scenarios that are assigned a probability over 5% are shown. For each scenario, we also report the fraction assigned to each RANS model in the mixture, *i.e.* $p\left(M_m|S_s, \overline{\boldsymbol{\delta}}_s\right)p(S_s)$. For $BMSA_1$, the calibration scenarios are labelled as in [3]. The scenario weighting criterion automatically assigns higher probabilities to scenarios corresponding to mixed pressure gradients (airfoil-like cases like S_{2100}) or to zero-gradient (S_{1400}) and mildly favorable cases (S_{6300}), which is a bit counter-intuitive. This is probably due to the fact that model agreement for the prediction scenarios is better for regions of favorable pressure gradient (the left part of the blade), leading to lower errors and then higher weighting of such scenarios. Overall, the five more influential scenarios shown in the figure are assigned relatively similar weights, which increases the dispersion of the predictions around its mean, and ultimately the variance as observed in Figures 5.3a and 5.5a. For $BMSA_2$, scenario weighting is little affected by the MAP approximation. Nevertheless, for both the propagation methods, the scenarios are assigned similar probabilities, with scenarios the S_1 and S_3 being preferentially weighted with respect to S_4. This can be explained by the proximity of the inlet flow angle of S_2 with S_3 and S_1. For S_1 and S_3, the flow is qualitatively similar to S_2, which is not the case for S_4. In all BMSA, the Spalart–Allmaras model is generally assigned the highest probability, and $k-\varepsilon$ the lowest. This ranking of the RANS model accuracy is in accordance with the authors' experience on such flow configurations. Using the MAP approximation changes slightly the model evidences, and subsequently model weighting within each scenario, but the results are overall very close to the $BMSA_2$ using the full posterior distributions.

In addition to speeding up the prediction phase, the MAP approximation of the posteriors allows easily to predict any QoI in the flow with no extra cost. For instance, Fig. 5.7 shows the isocontours of the mean and standard deviation of the total pressure field around the blade. The latter provides a global view of flow regions that are the most sensitive to the turbulence model, namely the boundary layers and the wake. Fig. 5.8 shows the BMSA prediction of the expectancy and variance of the Mach number field. As expected, this QoI is less sensitive to the turbulence model than the pressure loss, since the flow is attached and the Mach number field is mostly determined by inviscid mechanisms: this further illustrates the effectiveness of the MAP-based BMSA procedure.

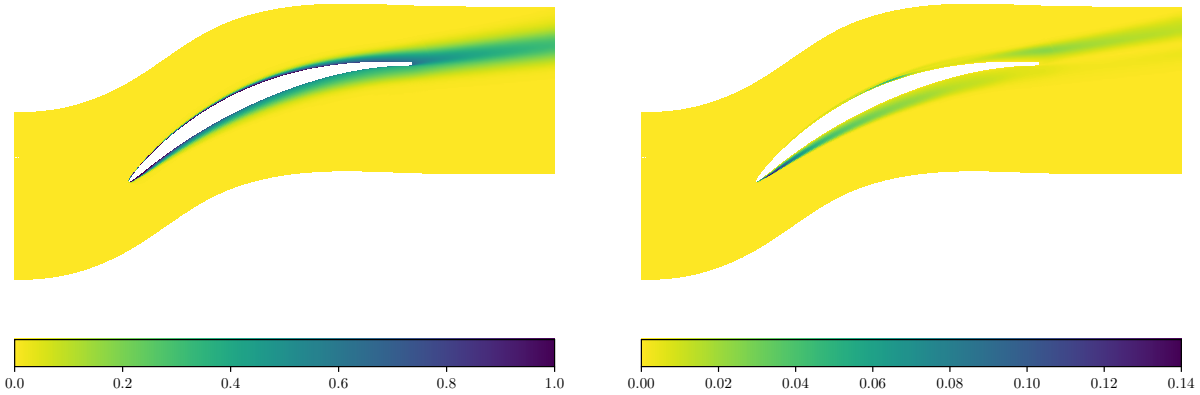

(a) $E\left[P_t(\mathbf{x}_i)|S_2\right]$ (b) $Var\left[P_t(\mathbf{x}_i)|S_2\right]$

Figure 5.7: 2-D contour of first two moments of the BMSA prediction for normalized total pressure for scenario 2. In this case, we considered MAP estimates on scenarios $\mathcal{S} = \{S_1, S_3, S_4\}$

Finally, in Fig. 5.9, we show the BMSA prediction for a particularly sensitive QoI, namely, the Turbulent Kinetic Energy (TKE). Since the Spalart-Allmaras model does not provide an output for this quantity, the BMSA model is constructed using the $k-\varepsilon$ and $k-\omega$ models only, with MAP estimates of the coefficients calibrated for scenarios S_1, S_3 and S_4. The model probabilities are always based on the evidences computed at the end of the calibration step, renormalized for the present subset of models. In the figure we report the TKE profile at $x/l = 0.99$ along the suction side. As for tangential velocity and total pressure, the BMSA prediction shows a significant improvement over the baseline RANS models. Additionally the reference LES solution is contained within less than 2 standard deviations from the average.

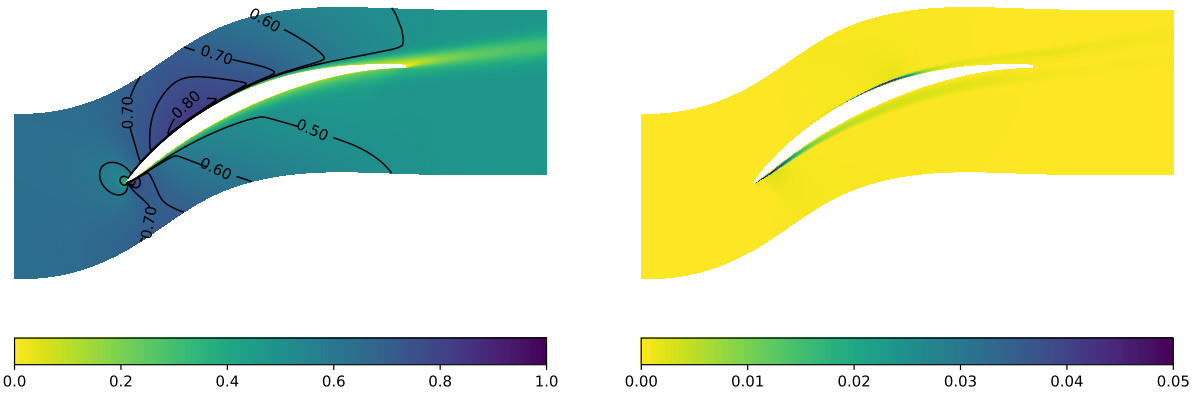

(a) $E\left[M_a(\mathbf{x}_i)|S_2\right]$ (b) $Var\left[M_a(\mathbf{x}_i)|S_2\right]$

Figure 5.8: 2-D contour of first two moments of the BMSA prediction of the Mach number for scenario 2. In this case, we considered MAP estimates on scenarios $\mathcal{S} = \{S_1, S_3, S_4\}$

Based on the preceding results and discussion, only MAP-based BMSA models are considered in the rest of the paper.

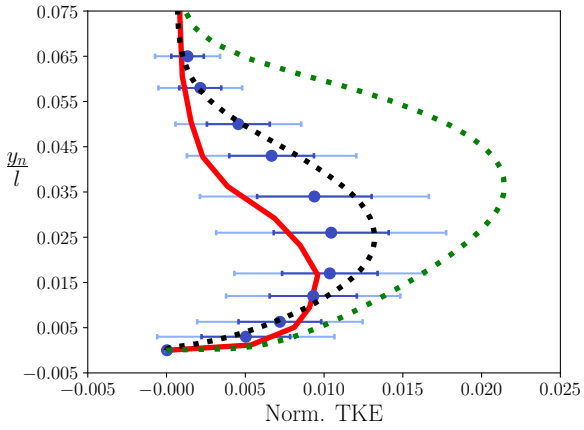

Figure 5.9: Prediction of the tangential TKE profile at $x/l = 0.99$ on the suction side for scenario 2. LES data from Leggett *et al.* [7] (—), $E\left[\Delta|S'\right] \pm \sqrt{Var\left[\Delta|S'\right]}$ (—●—), $E\left[\Delta|S'\right] \pm 2\sqrt{Var\left[\Delta|S'\right]}$ (—●—), Baseline $k-\omega$ (·····) and Baseline $k-\varepsilon$ (-·-·-).

5.4.2.2 BMSA prediction for S_4

The BMSA mixture model is then applied for the prediction of the more challenging off-design condition separated flow scenario S_4. The $BMSA_1$ and $BMSA_2$ approaches are thus compared. The

set of calibration scenarios is $\{S_1, S_2, S_3\}$ for the $BMSA_2$. Those approaches are completed on one hand by a BMSA model computed from the aggregation of the on-the-shelf scenarios of [69] and S_1, S_2 and S_3; this is referred to as $BMSA_3$. On the other hand, just a BMA for S_4 is performed.

The predictions for the tangential velocity profile at $x/l = 0.99$ are plotted in Fig. 5.10. More specifically, the predictions for $BMSA_1$, $BMSA_2$, $BMSA_3$ and the BMA are depicted in Figs 5.10a, 5.10b, 5.10c and 5.10d respectively. The $BMSA_1$ clearly underestimates the size of the backward flow region. Nevertheless, the predicted velocity profile exhibits incipient separation and the 2-standard deviation confidence interval encompasses reasonably well the reference LES solution. For $BMSA_2$, the mean solution compares poorly with the reference LES. Since $BMSA_2$ has been calibrated on attached scenarios, the coefficients controlling the eddy viscosity have larger values than the nominal values. This leads to even fuller velocity profiles than the baseline models (which already fail to predict flow separation), except for the baseline $k-\omega$ that underestimates the size of the reversed flow. We also observe that, in this case, the confidence intervals are small and do not encompass the reference data. This is due to the fact that the models in the mixture all rely on similar but wrong solutions. This result shows the importance of including sufficiently diverse scenarios in BMSA models. In the present BMSA, predictions are based on models with similar characteristics (linear eddy viscosity), furthermore calibrated on similar attached flow scenarios. As a consequence, the resulting BMSA model is very good at predicting flow scenarios similar to the calibration ones but generalizes badly to a different flow, leading to less accurate results than $BMSA_1$. Increasing the diversity of scenarios in the model mixture, as for $BMSA_3$, has a beneficial effect on the solution. The $BMSA_3$ prediction is not as accurate as the $BMSA_1$ but it is not worst than the naively averaged baseline RANS models either. In addition, estimates for the confidence intervals are provided for which the reference data are captured within 2 standard deviations. Besides, the latter is artificially inflated by including numerous scenarios. That can be used as a criterion for retraining the model for the scenario under consideration. Finally, if data for the new scenario become available, as in BMA, model retraining is effective in improving the quality of the prediction while reducing the confidence intervals. This enforces the conclusion that the discrepancies noted for $BMSA_1$, $BMSA_2$ and $BMSA_3$ originate from not suited calibration scenarios. Also, for BMA the variance only accounts for residual deviations between the various RANS models in the data set after calibration. This partially explains

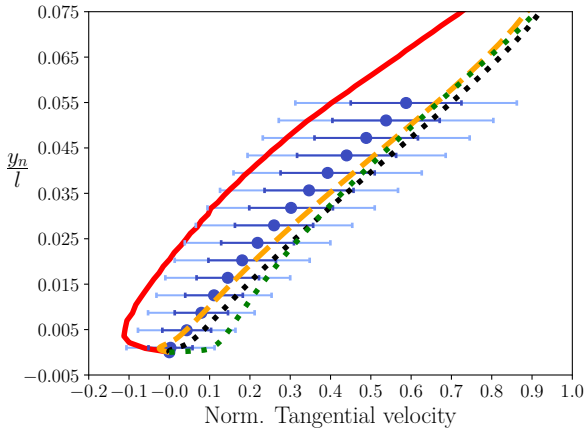

(a) MAP estimates calibrated on flat-plate scenarios [69] ($BMSA_1$).

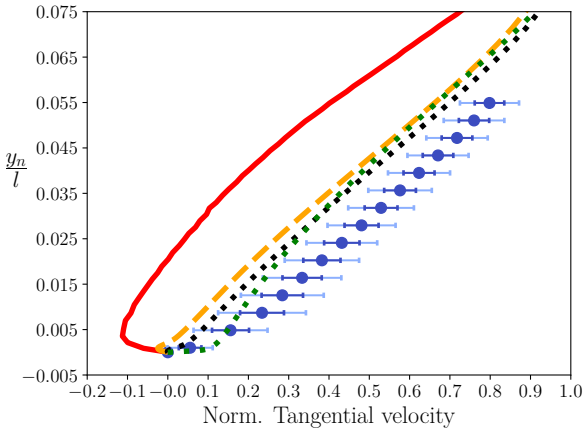

(b) MAP estimates obtained on $\mathcal{S} = \{S_1, S_2, S_3\}$ ($BMSA_2$).

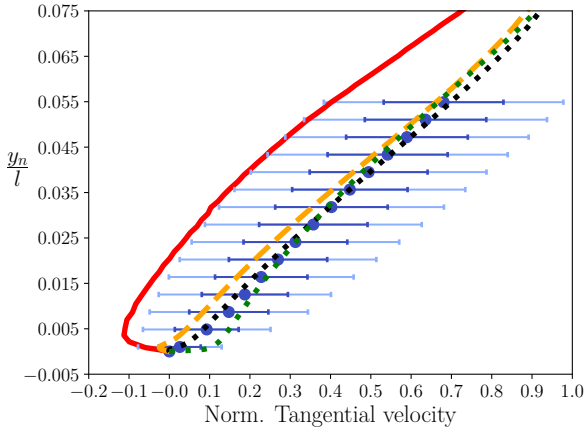

(c) MAP estimates obtained on $\mathcal{S} = \{S_{1400}, ..., S_{2134}, S_1, S_2, S_3\}$ ($BMSA_3$).

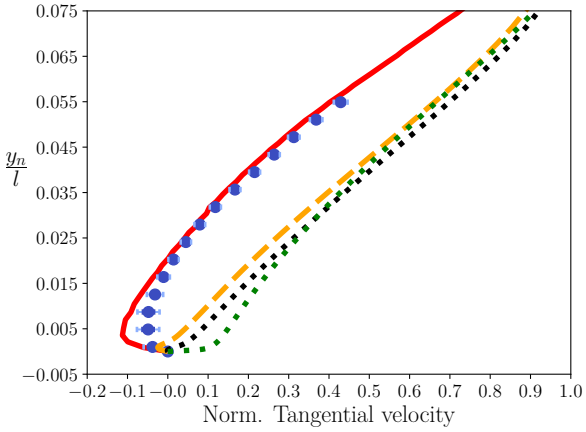

(d) BMA prediction for scenario S_4 using RANS models calibrated for the same scenario.

Figure 5.10: Prediction of the tangential velocity profile at $x/l = 0.99$ on the suction side for scenario 4. LES data from Leggett *et al.* [7] (—), $E[\Delta|S'] \pm \sqrt{Var[\Delta|S']}$ (—●—), $E[\Delta|S'] \pm 2\sqrt{Var[\Delta|S']}$ (—●—), Baseline $k-\omega$ (·····), Baseline Spalart–Allmaras (- - -) and Baseline $k-\varepsilon$ (-·-·-).

the reduction of variance.

The scenario probabilities are reported in Fig. 5.11 for the three BMSA. We focus again only on scenarios with a probability of 5% or higher. For $BMSA_1$ (Fig. 5.11a), S_{1400} is the most influential scenario, *i.e.* the zero pressure gradient flat plate, probably owing to strong model agreement in the upstream portion of the flow. Interestingly, the BMSA now also assigns significant weights to S_{1100} and S_{2500}, characterized by mildly adverse pressure gradients, and S_{1200} which is representative of a "diverging channel, with eventual separation". Such scenarios were not assigned any significant

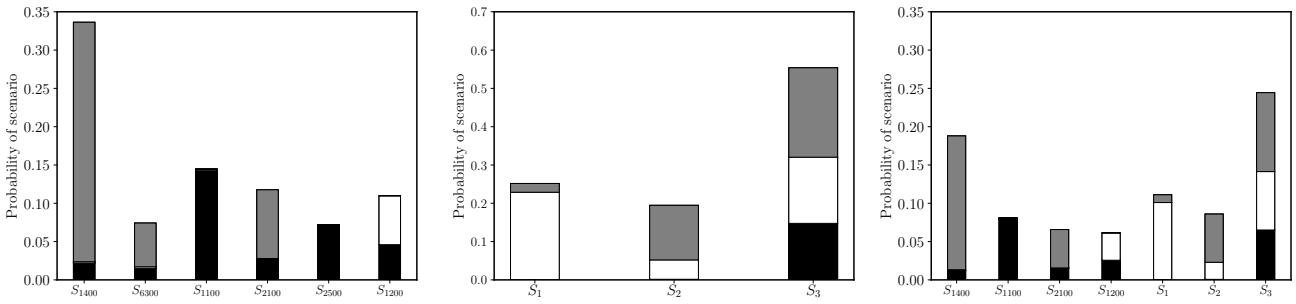

(a) Obtained with MAP estimates calibrated on flat-plates [69] ($BMSA_1$).

(b) Obtained with complete distributions on $\mathcal{S} = \{S_1, S_2, S_3\}$ ($BMSA_2$).

(c) Obtained with MAP estimates on $\mathcal{S} = \{S_{1400}, ..., S_{2134}, S_1, S_2, S_3\}$ ($BMSA_3$).

Figure 5.11: Distribution of $p(S_s)$ and $p\left(M_m|\overline{\boldsymbol{\delta}}_s, S_s\right)$ in case of scenario 4. Only scenarios with probability superior to 5% are shown on Figure 5.11a. Each bar sums to the probability of the scenario. Each probability of scenario is then decomposed into probabilities of models, given this scenario. $k-\varepsilon$ (■), $k-\omega$ (□) and Spalart–Allmaras (▩).

probability in the S_2 solution. For $BMSA_2$ (Fig. 5.11b), the highest probability is assigned to S_3, followed by S_1 and finally S_2. This shows that the scenario weighting criterion tends to promote scenarios with inlet angles closest to the one of the prediction scenario. Finally, $BMSA_3$ (Fig. 5.11c), based on 17 scenarios, assigns weights larger than 5% only to 7 scenarios (only one more than $BMSA_1$). The higher weights are given to the mixed and adverse pressure gradient scenarios from $BMSA_1$ and to the NACA65 scenarios, which is in agreement with expert judgement since the mean predictions seem closer to the $BMSA_1$ than the $BMSA_2$.

5.4.3 Effects of prior scenario probability criteria

In this subsection we investigate the influence of the prior scenario probability criteria on the BMSA prediction. Additionally, we increase the diversity of the model set by adding two new models, namely, Smith's $k-l$ and the EARSM $k-kL$, described in Chapter 2. The multi-model ensemble $\mathcal{M}$ is therefore now constituted of five turbulence models, namely the $k-\varepsilon$, $k-\omega$, $k-l$, Spalart–Allmaras and the EARSM $k-kL$ model.

Concerning the second purpose, three alternative BMSA models are constructed by using the three *a priori* scenario weighting criteria described in 5.2.1. The criterion of Eq. (5.8) is used as the reference criterion, to which the two others are being compared. As MAP approximation has been proven effective on the preceding subsection, the three BMSA models are all based on the MAP hypothesis.

In the following, we focus on the BMSA prediction of a vector of QoIs Δ for scenario S_2, using the five turbulence models calibrated for the other three scenarios. More specifically, we report the results for two QoIs, the tangential velocity profile at $x/l = 0.99$, l being the chord and $x/l = 0$ the position of the blade leading edge and the total pressure loss at $x/l = 1.10$. All results obtained on this section are tabulated in Table 5.3. Similar results are observed for velocity profiles and total pressure loss at different locations and for other QoIs.

Model used for prediction		Mean-square error on Tang. Velocity	Mean-square error on Total Pressure Loss
BASELINES	Spalart-Allmaras	0.950	0.329
	$k-l$	1.080	0.376
	$k-\omega$	0.979	0.384
	$k-\varepsilon$	1.978	0.763
	EARSM $k-kL$	1.384	0.503
BMSA with the following criterion for $p(S_s)$	Model agreement	0.608	0.238
	Calibration-driven	0.625	0.250
	Naive	0.717	0.272

Table 5.3: Root-Mean Square values for the baseline models and the BMSA prediction under the three criteria for $p(S_s)$. The results are presented for the two QoI presented in Fig. 5.13 and Fig. 5.14.

We first compare on Fig. 5.12 the probabilities assigned to the various scenarios according to the three criteria in Eqs. (5.8), (5.9), (5.10). As noted previously, each bar sums to the probability of the scenario $p(S_s)$. For each scenario S_s the various shades represents the weights assigned to the different models, *i.e.* the posterior model probabilities $p\left(M_m|S_s, \overline{\boldsymbol{\delta}}_s\right)$. The figure shows that the hierarchy between the probabilities of scenarios is the same for all criteria. S_3 is always assigned the highest probability, and it is indeed the closest one to S_2 in the space of operating conditions. We also note that scenario S_1, characterized by more severe off-design conditions than S_2 and S_3 but exhibiting fully attached flow, is always preferred to scenario S_4, characterized by a separated flow region at the rear part of the suction side. The probabilities assigned to each scenario differ slightly from one criterion to another. For example, S_4 is given a higher probability according to criterion (5.10), compared to criteria (5.8) and (5.9). It is also worth noticing that the $EARSM\ k-kL$ model is not assigned higher probability than the linear eddy viscosity models for scenarios S_3 and S_4, while it is overwhelmingly preferred for scenario S_1. This results partly from the greater accuracy of $EARSM$

for this scenario. Also, the prior ranges used to calibrate this model for scenario S_1 are, for numerical robustness reasons, significantly narrower than those of the other models, resulting in a higher model evidence and, subsequently, also in a higher posterior probability for this model.

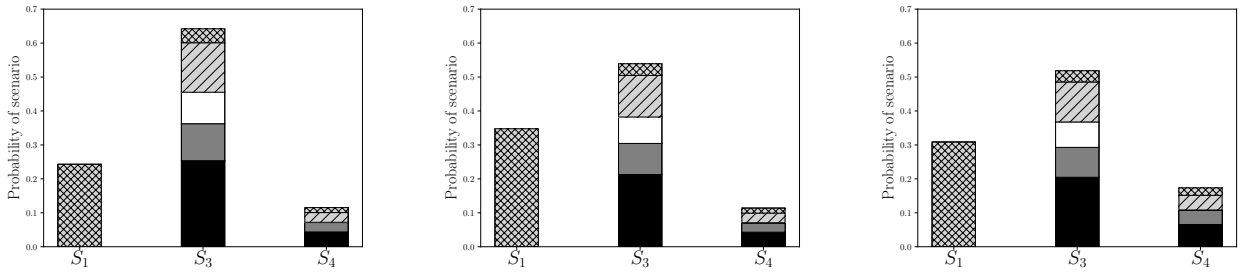

(a) BMSA prediction obtained with $p(S_s)$ defined as in Eq. (5.8).

(b) BMSA prediction obtained with $p(S_s)$ defined as in Eq. (5.9).

(c) BMSA prediction obtained with $p(S_s)$ defined as in Eq. (5.10).

Figure 5.12: Distribution of $p(S_s)$ and $p\left(M_m|S_s, \overline{\boldsymbol{\delta}}_s\right)$ in case of scenario 2, for different $p(S_s)$ criteria. Probabilities of models are presented with the following colors: Spalart–Allmaras (■), $k-\omega$ (■), $k-\varepsilon$ (□), $k-l$ (▨), $EARSM$ $k-kL$ (⊠) .

We present in Fig. 5.13 (left) the tangential velocity profile and variance decomposition (right) for the tangential velocity profile at $x/l = 0.99$. The y-axis represents the normalized distance to the wall y_n/l, y_n being the distance to the blade. The results are based on the same BMSA model, but each figure uses a different criterion for the probability of scenarios. Predictions of the baseline RANS models are also reported for comparison. The baseline $k-\omega$, $k-l$, EARSM $k-kL$ and Spalart–Allmaras models provide rather close predictions, in better agreement with the LES data than the baseline $k-\varepsilon$ model, which performs noticeably worse than the other four models for this case.

The BMSA predictions are reported in the left side of Fig. 5.13. We first note that the predictive accuracy of BMSA improves significantly when compared to the baseline models, due to the calibration of the coefficients for compressor scenarios, in similar fashion to Fig. 5.3b. In all cases, the mean prediction $E[\Delta|S']$ is in much closer agreement with LES reference data, which are captured within the 1-standard deviation confidence interval in all cases. The three scenario weighting criteria give similar results both in terms of average profiles and confidence intervals, even if their formulation is significantly different. The best results are obtained using the more costly model-agreement criterion, while the naive criterion, which assigns a higher weight to a flow scenario rather different from the

prediction one, leads to a slightly less accurate prediction and larger uncertainty intervals.

The right side of Fig. 5.13 illustrates the variance decomposition according to Eq. (5.4) for the corresponding tangential velocity. Since only MAP approximations are propagated for the prediction, the *within-model, within scenario* variance term is exactly equal to zero. The main contribution to the variance is once again due to the *between scenarios* component, which indicates that the uncertainty associated with the calibration of the closure coefficients for different scenarios is the largest source of uncertainty here. Fig 5.13 further shows that the total variance predicted by the naive $p(S_s)$ criterion is larger than for the two other cases. The additional part of variance is mostly associated to the *between scenarios* component, which in turn depends on the larger probability given to S_4. The quantification of the variance on the prediction, which is directly related to the confidence intervals, is a valuable information in our case, and it can be used as a measure of quality of the $p(S_s)$ criterion. In fact, confidence interval must be large enough to capture the reference data, but should also be small enough to give a valuable information about the predictive uncertainty. Keeping that in mind, the naive criterion seems to be the worst performing criterion, and the most restrictive in terms of application to a large variety of scenarios, and therefore it must be discarded.

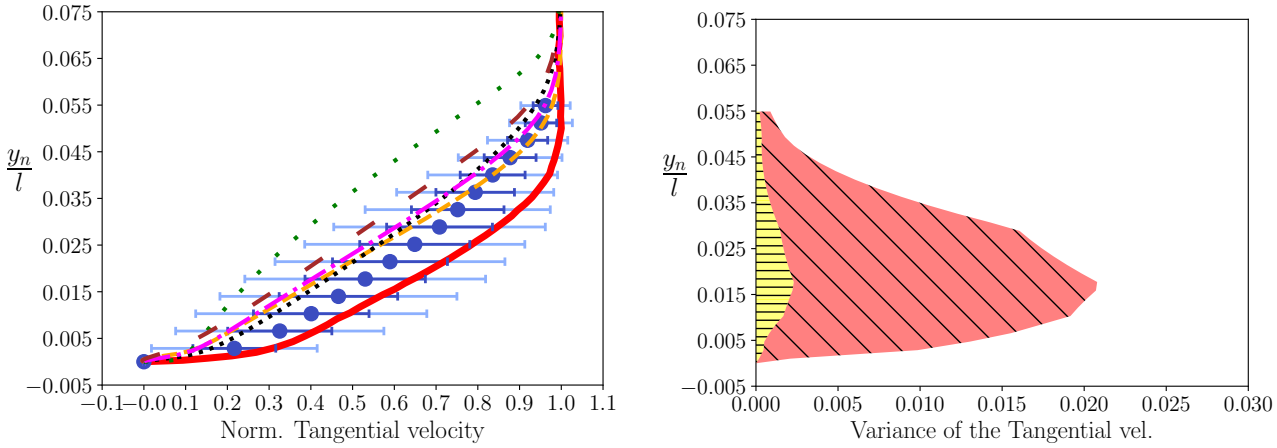

(a) Results obtained with $p(S_s)$ defined as in Eq. (5.8).

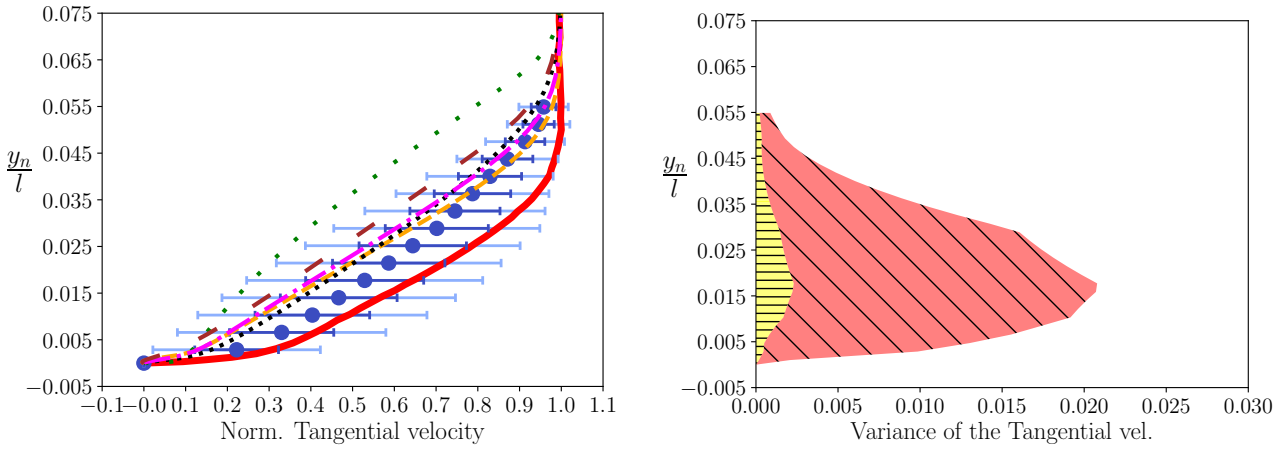

(b) Results obtained with $p(S_s)$ defined as in Eq. (5.9).

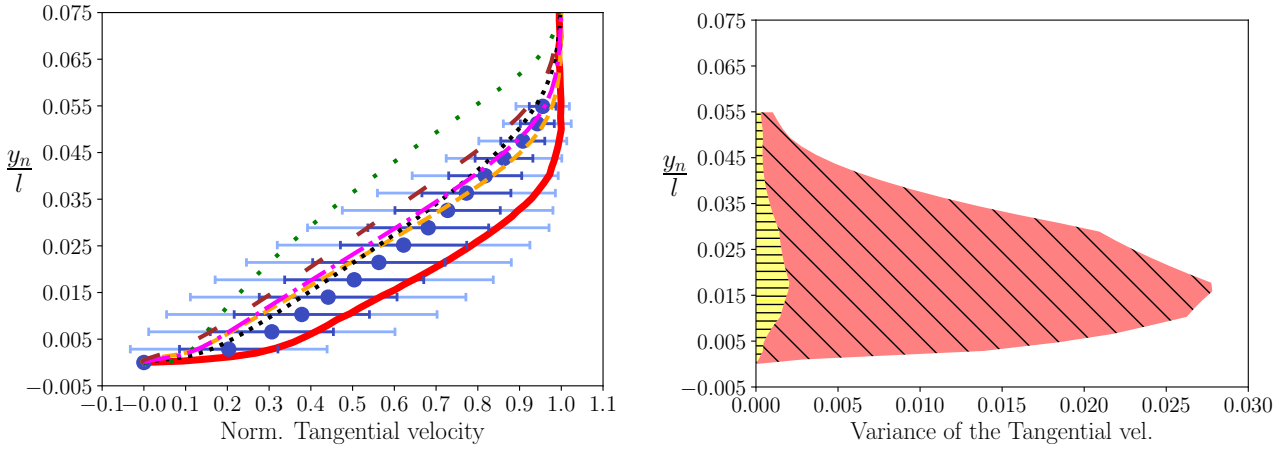

(c) Results obtained with $p(S_s)$ defined as in Eq. (5.10).

Figure 5.13: Prediction (left) and decomposition of the variance (right) for the normalized tangential velocity profile at $x/l = 0.99$ on the suction side for scenario 2.
Left: LES data from Leggett *et al.* [7] (——), $E[\Delta|S'] \pm \sqrt{Var[\Delta|S']}$ (—●—), $E[\Delta|S'] \pm 2\sqrt{Var[\Delta|S']}$ (—●—), Baseline $k-\omega$ (·····), Baseline Spalart–Allmaras (- - -) and Baseline $k-\varepsilon$ (-·-·-), Baseline $k-l$ (-·-·-) and Baseline $EARSM$ $k-kL$ (- -) .
Right: ■ *within-model, within scenario variance*, ■ *between models, within scenario variance* and ■ *between scenario variance.*

BMSA predictions of the total pressure loss profile across the wake are presented in the left side of Fig. 5.14. The quantity on the y-axis (namely y/l) represents the normalized cross-flow position, with the origin aligned with the trailing edge. For this QoI, the BMSA models show a behavior similar to the velocity profiles. The three BMSA models predict a profile closer to the LES than the RANS baseline models. The LES reference data fall within the 2-standard deviation confidence interval in all cases. Similarly to the tangential velocity profiles, the three scenario weighting criteria give consistent results in terms of average profiles and confidence intervals. The model-agreement criterion is again found to be the best performing criterion, whereas the naive criterion yields once again the least accurate prediction and largest uncertainty intervals.

The right side of Fig. 5.14 displays the variance decomposition of the total pressure loss for the corresponding BMSA prediction. The three BMSA models predict roughly the same variance decomposition. The solution variance exhibits two peaks: the highest one is located at the upper side of the wake, and it is mainly due to the large *between scenario variance*; the lower one is almost exclusively due to the *between models, within scenario variance*. As the flow scenario are characterized by different inlet flow angles, the predicted wake position would differ for each scenario, causing a large variance in the wake. It is worth noticing that this variance mostly concerns the upper side of the wake, where the scenarios S_3 and S_4 would predict the position of the wake.

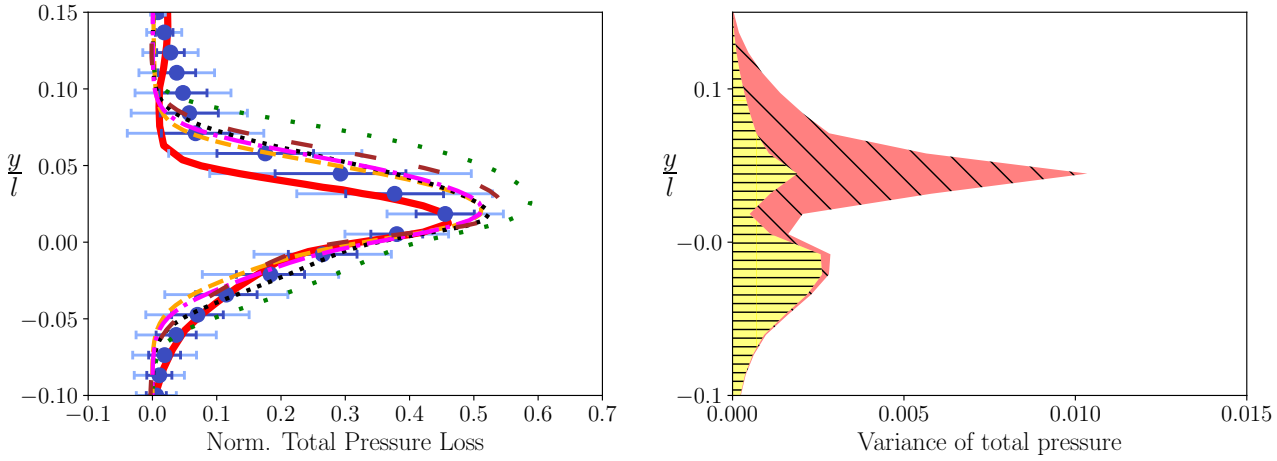

(a) Results obtained with $p(S_s)$ defined as in Eq. (5.8).

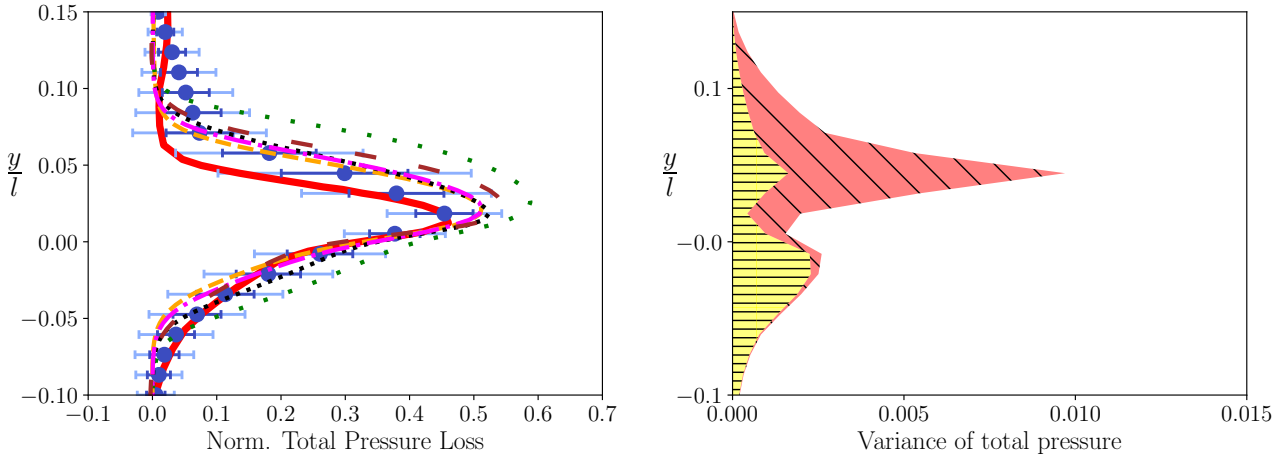

(b) Results obtained with $p(S_s)$ defined as in Eq. (5.9).

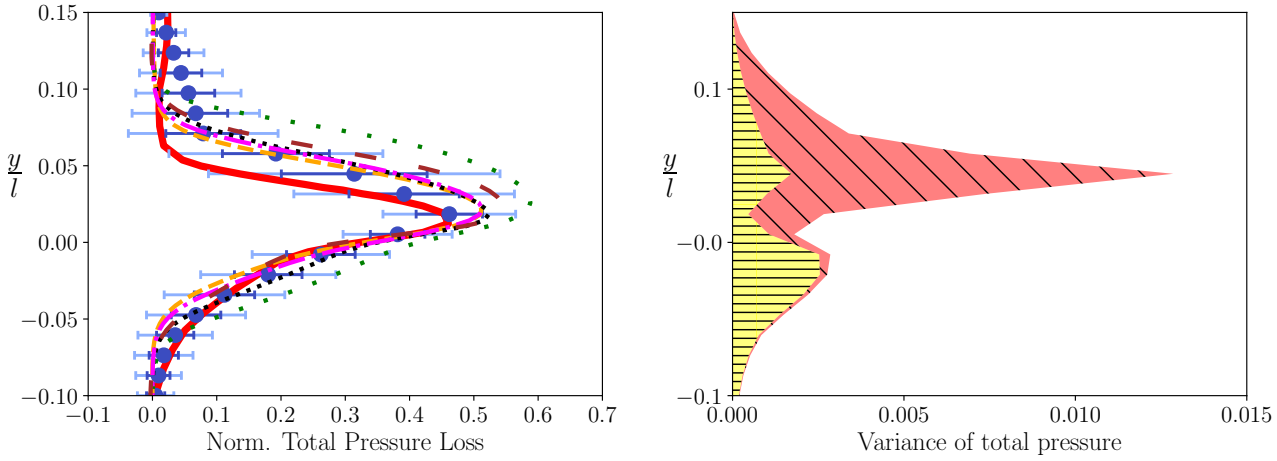

(c) Results obtained with $p(S_s)$ defined as in Eq. (5.10).

Figure 5.14: Prediction (left) and decomposition of the variance (right) for the normalized total pressure loss at $x/l = 1.10$ in the wake for scenario 2.
Left: LES data from Leggett *et al.* [7] (——), $E[\Delta|S'] \pm \sqrt{Var[\Delta|S']}$ (—●—), $E[\Delta|S'] \pm 2\sqrt{Var[\Delta|S']}$ (—●—), Baseline $k-\omega$ (·····), Baseline Spalart–Allmaras (- - -) and Baseline $k-\varepsilon$ (-·-·-), Baseline $k-l$ (-·-·-) and Baseline $EARSM$ $k-kL$ (- -) .
Right: ■ *within-model, within scenario variance*, ■ *between models, within scenario variance* and ■ *between scenario variance.*

5.5 Conclusions

In this chapter, the Bayesian framework is assessed for the quantification and reduction of modeling uncertainties in RANS-based simulations of turbomachinery flows. In this framework, modeling uncertainties are treated in terms of probabilities. Specifically, the closure coefficients associated with RANS models are treated as random variables, which are assigned an a priori probability distribution based on their nominal values and expert judgement. Bayesian inference from observed data for selected calibration variables is used to reduce the uncertainty ranges of the coefficients, leading to a posteriori distributions for the parameters. The latter can be propagated through the model by means of an Uncertainty Quantification (UQ) method to obtain predictions with quantified uncertainty of a new flow. Additionally, the proposed framework leverages information from a set of concurrent RANS models and a set of concurrent calibration scenarios to build a mixture model based on Bayesian Model & Scenario Averaging (BMSA).

First, BMSA models were constructed by initially averaging three linear-eddy viscosity models, then four linear-eddy viscosity models and one EARSM model widely used for industrial applications. A baseline mixture model, named $BMSA_1$, was constructed by using on-the-shelf sets of model coefficients calibrated for 14 turbulent flat-plate flow scenarios corresponding to different external pressure gradients [3]. A second model, named $BMSA_2$, was specifically tailored for the targeted flow configuration, *i.e.* the compressor cascade NACA 65 V103. In this case, each RANS model in the mixture was calibrated against reference LES data [4] available for 3 off-design scenarios and validated against data available for a fourth scenario, not included in the calibration set. The results show that, even if $BMSA_1$ was not calibrated for the flows of interest, the results obtained for a mildly off-design and a highly off-design scenario are globally not worst than the nominal models and the estimated confidence intervals encompass rather well the reference solution. On the other hand, the compressor-specific $BMSA_2$ model significantly improves the predictions compared to the baseline RANS models when it is used to predict scenario characterized by an intermediary inlet angle with respect to those included in the BMSA. Additionally, the predicted confidence intervals encompass the reference data. However, this strategy may lead to overfitting problems. When applied to a scenario with operating conditions leading to radically different flow features compared to the training scenarios, BMSA provides less accurate predictions than the baseline models. In addition, the confidence

intervals are strongly underestimated due to the insufficient diversity of models and scenarios included in the mixture.

Secondly, the choice of scenario weighting criteria is investigated. For that purpose, three empirical *a priori* probability mass functions (pmf) for the calibration scenarios were proposed. The first one assigns probability based on the agreement among the competing models applied to the prediction scenario. The second one assigns higher probability to scenarios that led to a better fit of the model output to the data in the calibration step. The last one is a naive weighting criterion assigning higher probability to scenarios closest to the prediction one in terms of operating conditions, based on expert judgment. The BMSA results were found to be little sensitive to the user-defined scenario-weighting criterion, both in terms of average prediction and of estimated confidence intervals. Interestingly, all criteria provided the same hierarchy of scenarios, even though the probabilities assigned by each criterion may differ. The naive criterion provides however less satisfactory results than statistical criteria. The criterion based on calibration accuracy is attractive in terms of computational cost, because it allows to discard a priori calibration scenarios that are not suitable for predicting the new flow at hand. It provides accurate results within the restricted range of flow scenarios considered in this study, but it may used with caution for predicting scenarios very different from the calibration ones. The scenario weighting criterion based on model agreement is the most accurate one, but also the more computationally expensive. Additionally, it may happen that all candidate models strongly agree on the wrong solution for some cases. This risk can be mitigated by mixing candidate models with sufficiently different structures.

Chapter 6

Space-dependent multi-model combination: application to the prediction of a compressor cascade

Contents

6.1 Introduction

As discussed in Chapter 3 and demonstrated in Chapter 5, BMA is a powerful tool for combining outputs from various competing models. Nevertheless, the models are weighted according to global measures of their capability to fit the data in the calibration scenario (posterior model probabilities),

thus neglecting the fact that different models may perform differently in different regions of the prediction domain. In the specific case of RANS models for instance, models as $k-\omega$ and Spalart-Allmaras tend to perform better in the near wall region that $k-\varepsilon$, while the latter is to be preferred far from the walls. This is the argument, for instance, which as led to the development of the well-known Menter's $k-\omega$ SST model [110]. A first attempt of using space-varing weights in BMSA can be found in [69], whereby scenario weights based on model agreement at different spanwise locations (instead of an average over the whole domain) are used to predict the M6 ONERA wing. Nevertheless, such approach is fully empirical and case-dependent.

In the present chapter, we propose and validate a novel space-dependent BMA algorithm, named XBMA. The algorithm is inspired from the *Clustered Bayesian Averaging* (CBA) algorithm initially proposed by Yu *et al.* [71], and designed for the purpose of making it suitable for CFD models. Specifically, while CBA is formulated in the geometric space, XBMA is formulated in a space of well-chosen features. We also simplified some steps of the original CBA algorithm to account for the high computational cost of calls to a CFD model. The resulting XBMA algorithm is then applied to the compressor cascade NACA65 V103 configuration. In the aim of establishing a proof of concept of the new algorithm, we first consider reference data obtained by simulating the cascade with the EARSM $k-kL$ turbulence model, as described in Chapter 4. This allows us to investigate the sensitivity of the proposed method to the number and location of the training data. In the last section of the chapter however, we drive the algorithm to its limits by considering the LES case, for which the data are limited in number and redundant in information.

As the EARSM model is considered for the generation of high-fidelity data, the ensemble of combined models is restricted to the four LEVM models described in Chapter 2, namely, the Wilcox' $k-\omega$, Launder–Sharma $k-\varepsilon$, Smith's $k-l$ and Spalart–Allmaras turbulence models. In reason of its different mathematical structure, the EARSM $k-kL$ model is well-suited for assessing XBMA potential for the prediction of a solution outside the range of LEVM models, thus mimicking the discrepancy between LEVM solutions and the LES.

The purpose of the present study is manifold: (*i*) we propose a cost-efficient space-dependent BMA algorithm for expensive flow computations; (*ii*) we investigate the predictive capability of such algorithm, both for the training scenario and for a scenario outside the training set; (*iii*) finally, we

discuss the sensitivity of XBMA to the number and spatial-location of the data.

The chapter is organized as follows. In Section 6.2, we present the XBMA algorithm. In Section 6.3, we describe the adaptation of the method to CFD, by formulating the average in a space of features, instead of the geometrical space. In Section 6.4, results are reported for three configurations and the benefits of the method are discussed. Finally, the main findings are discussed in Section 6.5, alongside concluding remarks.

6.2 XBMA methodology

In this section we first recall the CBA algorithm proposed by Yu *et al.* [71], then we propose modifications to make it suitable for CFD problems. This leads to the XBMA algorithm, presented in detail in Section 6.2.4, where the choice of the XBMA hyper-parameters is also discussed.

6.2.1 Clustered Bayesian Averaging (CBA) algorithm

A common experience in many industrial applications is that not only various competing models exist, but such models perform differently in different regions of the domain. For this reason, it makes sense to use different weights for BMA in different regions, since the local model probability is expected not to be the same.

In order to systematically account for spatial dependency within the BMA, Yu *et al.* [71] developed the *Clustered Bayesian Model Averaging*, based on the concept of *global partial update*. The CBA algorithm is briefly outlined in Alg. (1) when two models, M_1 and M_2, with identical prior model probabilities are considered. The key idea here is to compute local model probabilities by using only the subset of the dataset whose points belong to a specific region in the explanatory space (Yu *et al.* refer to the *covariate space*). For that purpose, the algorithm relies on the concept of Bayes factor and local Bayes factor. The former is defined by:

$$\mathcal{B}_{ij} = \frac{f\left(\tilde{\boldsymbol{\delta}} = \overline{\boldsymbol{\delta}} | M_i\right)}{f\left(\tilde{\boldsymbol{\delta}} = \overline{\boldsymbol{\delta}} | M_j\right)} \quad \text{such that} \quad \frac{p\left(M_i|\overline{\boldsymbol{\delta}}\right)}{p\left(M_j|\overline{\boldsymbol{\delta}}\right)} = \mathcal{B}_{ij}\frac{p\left(M_i\right)}{p\left(M_j\right)} \tag{6.1}$$

while the latter is:

$$\mathcal{B}_{ij}^{\overline{\boldsymbol{\delta}}_k} = \frac{f\left(\tilde{\boldsymbol{\delta}} = \overline{\boldsymbol{\delta}}_k | M_i\right)}{f\left(\tilde{\boldsymbol{\delta}} = \overline{\boldsymbol{\delta}}_k | M_j\right)} \tag{6.2}$$

Algorithm 1 *Clustered Bayesian Model Averaging* - Yu *et al.*

1: **for** q=1 **to** N_Q **do**

1.1: Randomly split the dataset in two :

$$(\mathbf{X}_1, \overline{\delta}_1) = \{(\mathbf{x}_d, \overline{\delta}_d)\}_{d=1}^{N_{\tilde{\boldsymbol{\delta}}}/2} \text{ and } (\mathbf{X}_2, \overline{\delta}_2) = \{(\mathbf{x}_d, \overline{\delta}_d)\}_{d=N_{\tilde{\boldsymbol{\delta}}}/2+1}^{N_{\tilde{\boldsymbol{\delta}}}} \tag{6.3}$$

1.2: Update $\boldsymbol{\theta}_m$ of the model M_m by calibrating from $\overline{\boldsymbol{\delta}}_1$ for the two models

$$f\left(\boldsymbol{\theta}_m|\tilde{\boldsymbol{\delta}} = \overline{\boldsymbol{\delta}}_1, M_m\right) = \frac{f\left(\tilde{\boldsymbol{\delta}} = \overline{\boldsymbol{\delta}}_1|M_m, \boldsymbol{\theta}_m\right) f\left(\boldsymbol{\theta}_m|M_m\right)}{f\left(\tilde{\boldsymbol{\delta}} = \overline{\boldsymbol{\delta}}_1|M_m\right)} \tag{6.4}$$

f can be model dependent.

1.3: For each pair $(\mathbf{x}_d, \overline{\delta}_d)$ in $\mathbf{X}_2$, compute:

$$\begin{aligned} f\left(\tilde{\delta}^* = \overline{\delta}_d|\tilde{\boldsymbol{\delta}} = \overline{\boldsymbol{\delta}}_1, M_m\right) &= \int_{\boldsymbol{\theta}_m} f\left(\tilde{\delta}^* = \overline{\delta}_d|\tilde{\boldsymbol{\delta}} = \overline{\boldsymbol{\delta}}_1, M_m, \boldsymbol{\theta}_m\right) f\left(\boldsymbol{\theta}_m|\tilde{\boldsymbol{\delta}} = \overline{\boldsymbol{\delta}}_1, M_m\right) d\theta_m \\ &= M_{md} \end{aligned} \tag{6.5}$$

1.4: Compute the log Bayes factor:

$$\ln\left(\mathcal{B}_{12}^{(d)}\right) = \ln\left(\frac{M_{1d}}{M_{2d}}\right),\ d = N_{\tilde{\boldsymbol{\delta}}}/2+1, ..., N_{\tilde{\boldsymbol{\delta}}} \tag{6.6}$$

1.5: Use CART regression tree algorithm (Breiman *et al.* [111]) for mapping $\{\mathbf{x}_d\}_{d=N_{\tilde{\boldsymbol{\delta}}}/2+1}^{N_{\tilde{\boldsymbol{\delta}}}}$ to $\{\ln\left(\mathcal{B}_{12}^{(d)}\right)\}_{d=N_{\tilde{\boldsymbol{\delta}}}/2+1}^{N_{\tilde{\boldsymbol{\delta}}}}$ and exhibiting different regions Λ_k of same values of $\ln\left(\mathcal{B}_{12}\right)$.

1.6: For each region Λ_k, compute the local log Bayes factor:

$$\ln\left(\mathcal{B}_{12k}\right) = \sum_{\substack{d=N_{\tilde{\boldsymbol{\delta}}}/2+1 \\ \mathbf{x}_d \in \Lambda_k}}^{N_{\tilde{\boldsymbol{\delta}}}} \ln\left(\mathcal{B}_{12}^{(d)}\right) \tag{6.7}$$

2: **end for**

3: Update $\boldsymbol{\theta}_m$ of the model M_m by calibrating from $\overline{\boldsymbol{\delta}}$ for the two models:

$$f\left(\boldsymbol{\theta}_m|\tilde{\boldsymbol{\delta}} = \overline{\boldsymbol{\delta}}, M_m\right) = \frac{f\left(\tilde{\boldsymbol{\delta}} = \overline{\boldsymbol{\delta}}|M_m, \boldsymbol{\theta}_m\right) f\left(\boldsymbol{\theta}_m|M_m\right)}{f\left(\tilde{\boldsymbol{\delta}} = \overline{\boldsymbol{\delta}}|M_m\right)} \tag{6.8}$$

4: For a new point $\mathbf{x}^*$ and each model M_m, compute the prediction of the model, and ultimately the final prediction in $\mathbf{x}^*$:

$$f\left(\tilde{\delta}^*|\tilde{\boldsymbol{\delta}} = \overline{\boldsymbol{\delta}}, M_m\right) = \int_{\boldsymbol{\theta}_m} f\left(\tilde{\delta}^*|\tilde{\boldsymbol{\delta}} = \overline{\boldsymbol{\delta}}, M_m, \boldsymbol{\theta}_m\right) f\left(\boldsymbol{\theta}_m|\tilde{\boldsymbol{\delta}} = \overline{\boldsymbol{\delta}}, M_m\right) d\theta_m \tag{6.9}$$

$$f\left(\tilde{\delta}^*|\tilde{\boldsymbol{\delta}}\right) = w_1^* f\left(\tilde{\delta}^*|\tilde{\boldsymbol{\delta}} = \overline{\boldsymbol{\delta}}, M_1\right) + (1 - w_1^*) f\left(\tilde{\delta}^*|\tilde{\boldsymbol{\delta}} = \overline{\boldsymbol{\delta}}, M_2\right),\ w_1^* = \frac{1}{N_Q} \sum_{\substack{q=1 \\ \mathbf{x}^* \in \Lambda_k}}^{N_Q} \frac{\mathcal{B}_{12k}^q}{1 + \mathcal{B}_{12k}^q} \tag{6.10}$$

where $\overline{\boldsymbol{\delta}}_k$ is a subset of $\overline{\boldsymbol{\delta}}$. By making a strong assumption of independence of the data, Yu *et al.* then compute the log Bayes factor by summing the local log Bayes factor:

$$\ln\left(\mathcal{B}_{ij}\right) = \sum_k \ln\left(\mathcal{B}_{ij}^{\overline{\boldsymbol{\delta}}_k}\right) \tag{6.11}$$

The other key point is the *global partial update* used at steps 1.2 and 1.3 of the algorithm with Eq. (6.4) and (6.5) for which the data used for updating $\boldsymbol{\theta}$ and computing the evidence are different.

In the context of CFD, however, this approach is computationally intractable, due to the simultaneous calibration of the models (update of $\boldsymbol{\theta}$ at stage (1.2)), which is randomly repeated several times. Such a step is not applicable for CFD models, unless a surrogate model is used. Even in that case, a surrogate of the full CFD fields would be required, which is far from a straightforward task, as discussed in the preceding chapter. Another difficulty comes from the assumption of independence of the data, which is somehow difficult to be argued. Finally, the local model probabilities learned from this algorithm are specific to a geometry and can not be used for a different one.

6.2.2 Presentation of the XBMA algorithm

In order to be applicable to complex CFD problems, the desired algorithm must learn spatially-dependent model weights similarly to the CBA, while avoiding the computational burden of calibrating the model parameters $\boldsymbol{\theta}$ at stage (1.2). From a Bayesian point of view, this means that $\boldsymbol{\theta}$ is no longer treated as a random variable.

First, let us give a new definition for the random variable $\tilde{\delta}$. From now on, $\tilde{\delta}$ is no longer continuous but a discrete random variable whose realizations are the outputs of the various models $\{\delta^m = M_m(\mathbf{x}; \boldsymbol{\theta}_m, S)\}_{m=1}^{N_M}$. Hence, the mean and the variance of $\tilde{\delta}$ writes:

$$E\left[\tilde{\delta}\right] = \sum_{m=1}^{N_M} p\left(\tilde{\delta} = \delta^m\right) \delta^m \tag{6.12}$$

and

$$Var\left[\tilde{\delta}\right] = \sum_{m=1}^{N_M} p\left(\tilde{\delta} = \delta^m\right) \left(\delta^m - E\left[\tilde{\delta}\right]\right)^2 \tag{6.13}$$

Here the variance is a kind of indicator of the consensus between the models: small variances result from a strong agreement between the predictions while large variances reveal a divergence.

Inspired by the BMA, the model probabilities are then computed by:

$$p\left(\tilde{\delta} = \delta^m\right) = \frac{g(\delta^m, \overline{\delta}) w(\delta^m)}{\sum_{i=1}^{N_M} g(\delta^i, \overline{\delta}) w(\delta^j)} \tag{6.14}$$

at each point $\mathbf{x}$ in the domain and where $\overline{\delta}$ is a measurement of $\widehat{\delta}$, g is a cost function that evaluates the difference between the prediction of the model and the observation, and w is a pmf-like user-defined function representing the a priori trust in M_m. In this chapter, no model is a priori favoured meaning that $w(\delta^m) = 1/N_M$. As measurements of $\widehat{\delta}$ are not available for the entire domain, g must be estimated from the available observations by a regression-like procedure detailed in Section 6.2.3 so that Eq. (6.14) writes:

$$p\left(\tilde{\delta} = \delta^m\right) = \frac{\widetilde{g}(\delta^m) w(\delta^m)}{\sum_{i=1}^{N_M} \widetilde{g}(\delta^i) w(\delta^j)} \tag{6.15}$$

where $\widetilde{g}(\delta^m, \overline{\delta})$ is an approximation of $g(\delta^m, \overline{\delta})$. For a QoI Δ different from the observed quantity, Eq. (6.12) and (6.13) simply write:

$$E\left[\Delta\right] = \sum_{m=1}^{N_M} p\left(\tilde{\delta} = \delta^m\right) \Delta^m \tag{6.16}$$

and

$$Var\left[\Delta\right] = \sum_{m=1}^{N_M} p\left(\tilde{\delta} = \delta^m\right) \left(\Delta^m - E\left[\Delta\right]\right)^2 \tag{6.17}$$

where Δ^m is the Δ output of the model M_m corresponding to δ^m.

The choice of the cost function is a crucial point in the procedure because g acts as a growth/-damping factor in the discrepancies between the models. Many of them have been proposed in the literature, in this chapter we choose a squared exponential cost function defined by:

$$g(\delta^m, \overline{\delta}) = \exp\left[-\frac{1}{2}\left(\frac{\delta^m - \overline{\delta}}{\sigma}\right)^2\right] \tag{6.18}$$

where σ is a user-defined parameter. g is chosen such as to take a value which equals 1 or tends to 0 when the output of M^m and $\overline{\delta}$ perfectly match or are drifting apart respectively. Using a squared exponential function provides a smooth decrease of g as a function of $M^m - \overline{\delta}$, since the function is infinitely derivable. The parameter σ then controls how fast departure of the model prediction δ^m from the observed data $\overline{\delta}$ is penalized by the cost function g.

To emphasize the influence of σ on the cost function g, let us consider the following toy problem where two models are considered and indexed with 1 and 2. Fig. 6.1a illustrates the difference between

the cost functions $g(\delta^1, \overline{\delta}; \sigma)$ - $g(\delta^2, \overline{\delta}; \sigma)$ as a function of σ. It is straightforward that the function $g(\delta^1, \overline{\delta}; \sigma)$ - $g(\delta^2, \overline{\delta}; \sigma)$ admits one maximum for $\sigma = \sigma^*$. This value σ^* is optimal in the sense that it maximizes the discrimination between the models. For various values of the parameter σ, Fig. 6.1b plots the corresponding superposed cost functions $g(\delta^m, \overline{\delta}; \sigma)$ as a function of the model prediction δ^m. For the same model predictions (red and green vertical lines), the function $g(\delta^m, \overline{\delta}; \sigma^*)$ is the most desirable one, as this one allows the selection of the models to be the sharpest. From this toy problem, it seems clear that σ has a critical impact on the success of the approach. To ensure a well-behaved cost function, it is reasonable to choose σ as being of the same order of magnitude as $\delta^m - \overline{\delta}$. However, $\delta^m - \overline{\delta}$ varies from one point in space $\mathbf{x}$ to another. The median of the $(\delta^m - \overline{\delta})$ values taken on each of the spatial locations $\mathbf{x}$ appears to be a good trade-off for the choice of σ. A more complete discussion on the influence of σ on the XBMA algorithm for more than two models is presented in Section 6.2.4, with a focus on its asymptotic influence.

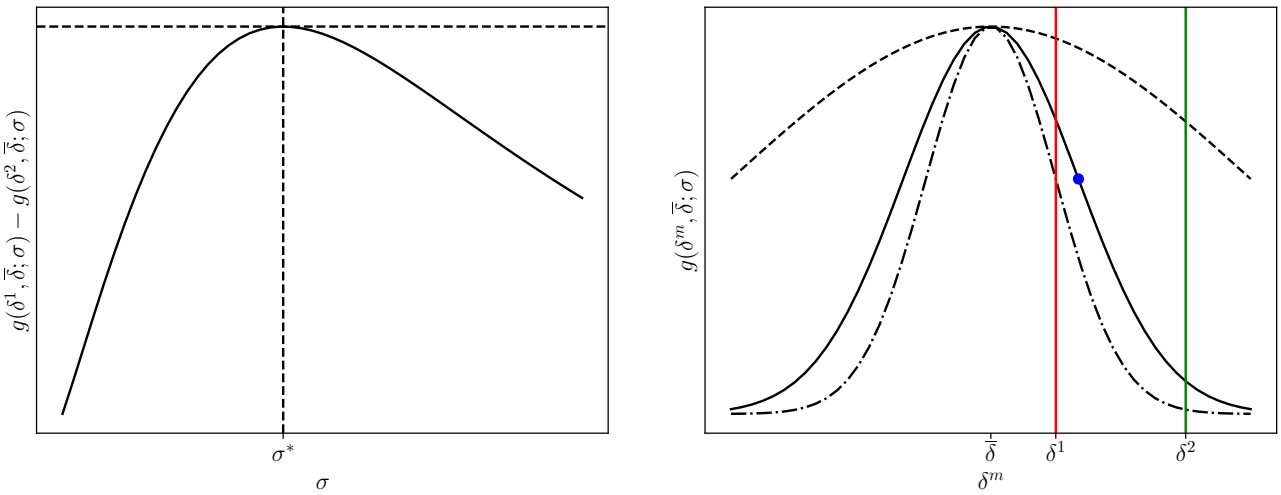

(a) Optimal value σ^* of σ.

(b) Plots of $g(\delta^m, \overline{\delta}; \sigma)$ for various values of σ $\sigma = \sigma^*$ (——) , $\sigma > \sigma^*$ (- - -), $\sigma < \sigma^*$ (-·-·-). inflexion point (•).

Figure 6.1: Influence of the parameter σ on the cost function g.

6.2.3 Supervised regression

As measurements of the quantity $\widehat{\delta}$ are not available for all points in the domain, a supervised regression is used to evaluate the cost function g at any point $\mathbf{x}$. Supervised regression refers to situations where a set of input-output pairs (the training data set) is provided, the goal being to learn the

function that maps inputs to outputs [112]. Supervised Machine Learning (ML) is a wide and well-discussed topic in the literature. Many very well-known model class algorithms fall into this category: linear models from the simplest least squares to complex non-linear regression [113], Support Vector Machine (SVM) and kernel methods [114], Gaussian Process Regression (also known as Kriging and used as metamodels in Chapter 5) [92], Ensemble Methods based on trees [115] or Neural Networks [116] are a few of them.

In the rest of the study, the supervised regression is based on Random Forests for three main reasons. First, they are well-adapted to large number of data and input features. As we wish to evaluate the influence of very large data sets on the prediction, the regressor must be adequately chosen for that purpose. The second reason is that we expect non-linear behavior in the regression, with possibly sharp variations and consequent gradients. As random forests are based on regression trees, they are well-fitted to capture this kind of behavior. Finally, Random Forests have produced good generalization results when applied in context of CFD [5, 38] and are a natural evolution of the ensemble of CART trees used by Yu *et al.* in their original algorithm [71]. As a reminder, Random Forests are an ensemble method that combine the prediction of multiple base models or (weak models) - in this case decision trees - to produce a robust prediction. Ensemble methods are particularly needed in the case of decisions trees are they remain very likely to overfit the data and thus lead to a biased prediction. More specifically, Random forests use bagging (sampling with replacement from the original training data set) to construct a randomized data set for each tree of the forest and randomly select a fixed number of input variable considered for the split at each node of each tree. This diversity on both the input variables and the training example considerably reduce variance in the prediction, while combining multiple predictions already reduce its bias. Random Forests are also efficient to build as they do not need pruning to prevent over-fitting (as decision trees do) and can be easily parallelized. Finally, four Random Forest hyper-parameters are considered here: the number of trees considered, the number of input features and the criterion evaluated for the choice of a split at each node and the minimum number of elements in each terminal leaves. The values of those parameters are chosen via cross-validation.

For the XBMA algorithm, we aim at generalising the model probabilities learnt on a peculiar

geometry to a different one, provided that the physics involved in the latter is reasonably similar to that of the training data set. Consequently, we base our regression on a feature space $\mathcal{H}$ rather than the physical space $\mathbb{R}^3$. Those features are meant to represent the local characteristics of the flow and are further detailed in Section 6.3.2. Hence, for a set of measures $\overline{\boldsymbol{\delta}} = (\overline{\delta}_1, ..., \overline{\delta}_d, ..., \overline{\delta}_{N_{\overline{\boldsymbol{\delta}}}})^T$ of $\widehat{\delta}$ at points $\mathbf{X} = \{\mathbf{x}_d\}_{d=1}^{N_{\overline{\boldsymbol{\delta}}}}$, we first map the vectors $\mathbf{x}_d$ into the feature space $\mathbf{x}_d \rightarrow \boldsymbol{\eta}_d = (\eta_{d1}, ..., \eta_{dh}, ..., \eta_{dN_{\mathcal{H}}})^T$, and then define a training set of input-output pairs $\mathbf{C}_m = \{(\boldsymbol{\eta}_{d,m}, g(\delta_d^m, \overline{\delta}_d))\}_{d=1}^{N_{\overline{\boldsymbol{\delta}}}}$ where $\delta_d^m = M_m(\mathbf{x}_d; \boldsymbol{\theta}_m, S)$. Note that $\mathbf{C}$ and $\boldsymbol{\eta}_d$ are indexed by m because the feature space might be different for each model M_m while $\mathbf{X}$ is identical.

A secondary data set is considered for the purpose of the prediction: it may or may not be the same as the training data set. If they are different, we expect the regression to be able to generalize to the new prediction data set. We call $\mathbf{P}_m = \{\boldsymbol{\eta}_{j,m}\}_{j=1}^{N_{\mathbf{P}}}$ the prediction data set.

6.2.4 XBMA algorithm

The XBMA algorithm is presented in the following Alg. 2. For the sake of clarity the standardization in step 2.1, the filtering in step 4 as well as a discussion on the effect of considering asymptotic values for the parameter σ are discussed hereafter.

First, we call standardization the step in which the training data set is reduced to a standard distribution, *i.e.* $\mathcal{N}(0, 1)$. This step is generally not considered helpful for Random Forest regression but is necessary in this case, as the reference data $\overline{\boldsymbol{\delta}}$ may gather different quantities of calibration. Those quantities must therefore be standardized to ensure that every reference data is treated accordingly.

Second, the need for a filtering in the 4^{th} step is further detailed now. We have observed that a few elements of the prediction data set $\mathbf{P}_m$ were causing a very low values of $\widetilde{g}$ for every model in the mixing. For those elements, the model probability computed through Eq. (6.15) was very unstable, as a small variation of the cost function of one model could create peaks or drops in the probabilities of every models through the normalization happening in the 5^{th} step. For those elements, a low value of the cost function for every model means that we, *de facto*, have very low confidence in the result predicted by the different models. Instead of assigning an unstable model probabilities in which we do not have confidence, we wish the XBMA to simply gets back to the naive choice for model mixing.

Algorithm 2 XBMA algorithm

1: Specify value for σ
2: **for** each model M_m: **do**
  2.1: Standardize the model predictions in $\mathbf{C}_m$
  2.2: Evaluate the cost function g for every calibration data set $\mathbf{C}_m$ using $\overline{\boldsymbol{\delta}}$
  2.3: Train the Random Forest to learn the regression between the inputs $\boldsymbol{\eta}_{d,m}$ and outputs $g(\delta_d^m, \overline{\delta}_d)$
  2.4: Use the Random Forest to predict the cost function $\widetilde{g}$ on the prediction data set $\mathbf{P}_d$
3: **end for**
4: Filter probabilities for every model whose cost function is smaller than the cutoff limit C
5: Compute $p(\tilde{\delta} = \delta^m)$ by Eq. (6.15)
6: Reconstruct the expected value and the variance of Δ from the baseline predictions of each model and Eq. (6.12) and (6.13)

By doing so, we treat the naive choice for model mixing as a prior on the model probabilities. We therefore set a cutoff-limit C on the cost functions of the models. If the cost function of every model is smaller than the cutoff-limit C for an element of the prediction data set $\mathbf{P}_m$, the XBMA returns to its prior probability of models *i.e.* $p(\mathcal{M} = \delta^m) = 1/N_M$. We have conducted a sensitivity analysis on the value of the cutoff-limit C and observed very little influence on the result for $C \in [0.02, 0.20]$. The value $C = 0.05$ is thus chosen for the rest of the study.

As previously discussed, small and large values of the parameter σ strongly affect the cost functions and, ultimately, the model probabilities. For values of σ close to zero, the cost function tends to assign a zero value to every element in $\mathbf{P}_m$ and every model. The normalization required to produce model probabilities in Eq. (6.15) can then be tricky for zones in which every cost function is given relatively low values. In those zones, a slight variation of the local errors $(\delta_d^m - \overline{\delta}_d)$ of one model produces peaks and drops in every model probability. The filtering occurring in 4^{rd} step negates this effect by producing a model probability of $1/N_M$ for those elements. In the rest of the prediction data set $\mathbf{P}_m$, one model is chosen at the expense of every other model. On that case, the XBMA is more a model selection method than a model averaging method.

On the contrary, asymptotically large values of σ will result in the argument of the exponential to be asymptotically close to zero and will lead to a cost function to be asymptotically equal to unity for every element of the training data set. The normalization step then produce a model probability of $1/N_M$ for every model and every element of the prediction data set. Large values of σ are therefore

associated with the naive choice for model mixing, *i.e.* giving the same probability to every model in the mixing. This behavior is desired as we do not trust the models in these areas and thus place a small confidence in the information provided by those data.

In the context of XBMA, the σ parameter is regulating the amount of trust put in the data, and consequently the amount of belief that one model should be chosen or neglected in the model mixing. Ideally, we would like the XBMA to give a chance to every model, while also effectively informing the probabilities of each model. For this reason, the parameters σ represents a trade-off between two competing forces, and need to be specified. We observed on the training scenarios that the $(\delta^m - \overline{\delta})$ values were roughly the same for the 4 RANS models considered, and of the order of 0.1. For this reason, we consider $\sigma = 0.1$ in the rest of the chapter.

6.3 Data generation and input features

The XBMA algorithm is a general method for assigning space-dependent model probabilities to an ensemble of models which can be deployed for a wide range of physical problem. The objectives of this section is to describe the necessary adjustments for the application of XBMA to a compressor cascade configuration. We first describe the reference data generation strategy with the intent of evaluating the influence of the number of elements in the training data set on the quality of the prediction. Then, we present in Section 6.3.2 the major adjustment for CFD, namely the input feature space. This set of inputs is based on local model predictions and greatly enhance the generalization capabilities of the method.

6.3.1 Scenarios and reference data

In this chapter, we use the EARSM reference data described in Chapter 4. In practice, one reference data set $\overline{\boldsymbol{\delta}}$ is first assembled from EARSM calculations on each of the four NACA 65 scenarios presented in Table 4.2. This data set is required for the evaluation of the cost function at step 2.2 of the XBMA algorithm. The effect of assimilating various kinds of data (velocity, total pressure, eddy viscosity and temperature data) to infer the XBMA model weights has been investigated. We observed that the total pressure was the most informative quantity. The reason for that can be that total pressure depends on both static pressure and velocity, and therefore carries more information

N_{thin}	1	2	3	4	6	8	10	12
Number of data $N_{\tilde{\boldsymbol{\delta}}}$	40080	10328	4870	2737	1361	820	562	416

Table 6.1: Number of data for each subset of the EARSM reference data produced on one scenario.

about the flow than pressure or velocity separately. For this reason, the data considered in the training data set $\overline{\boldsymbol{\delta}}$ for the rest of the study, also named quantity of calibration, is the total pressure.

For each of the four LEVM models in the mixing, one CFD calculation is initially run for each scenario in $\{S_1, S_2, S_3, S_4\}$, corresponding to the initial data set. We then constructed eight different subsets from this initial reference data set, each corresponding to a specific amount of data. The subsets were created by selecting one over N_{thin} elements on both the x-axis and the y-axis of the complete 2D-mesh. The value $N_{thin} = 1$ corresponds to the complete mesh, and therefore the complete data set. The values of the N_{thin} parameter and the corresponding total number of data in the subset are presented in Table 6.1. For illustration purpose, we present in Fig. 6.2 the arrangement of the probes in the case of $N_{thin} = 8$. We could have added intelligence in the data selection process, with the consideration of methods borrowed from the Optimal Sensor Placement community (OSP), or from physical knowledge on the flow. Nonetheless, we adopt a more systematic method for the sampling of the data, for three main reasons. First, this approach has the benefit of providing a parametric way to build the data sets. It is also relatively robust and easy to implement. Finally, the method maintains the same ratio of points close to the blade compared to the far-field. This ratio is indeed desirable to maintain within the training data set because basic CFD understanding assure that more information on the flow-physics is contained in the boundary layer rather than far from it. The drawback of this method is perhaps the redundancy of some points of the flow: there is little interest in the consideration of a large number of points far from the blade, as the information available in this zone is easily learned on a few points. Reducing the number of probes by leveraging OSP methods could be the purpose of a future work, but will not be explored in this chapter. As described in Alg. 2, the XBMA is agnostic of the concept of scenario as it uses one calibration data set $\mathbf{C}_m$ per model M_m. When only one scenario is considered, the training data set $\mathbf{C}_m$ is simply the subset of the corresponding scenario, model and desired number of data. When multiple scenarios are considered in the training, data sets corresponding to each scenarios are concatenated in the training data set

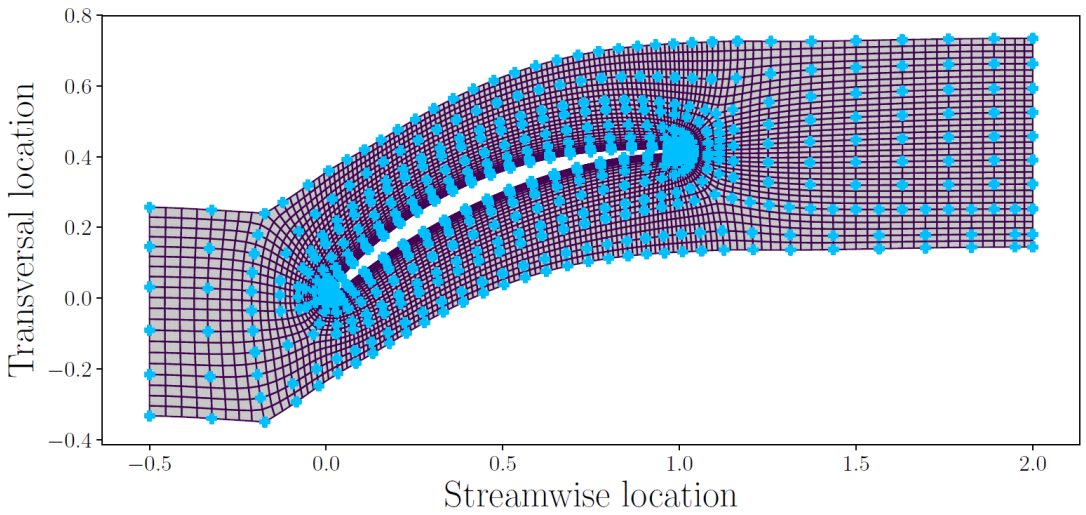

Figure 6.2: Locations of the elements of the data set corresponding to $N_{thin} = 8$. For representation purpose, only one over four mesh vertices are presented.

$\mathbf{C}_m$. When doing so, we use the same amount of data from each scenario to avoid over-representing one scenario.

6.3.2 Input Features formulation

As presented in the introduction, switching from the space of geometrical coordinates to the space of the input features is an effective method for generalizing prediction to a new unseen geometry.

In their early work, Ling and Templeton [5] laid down the foundations of efficient features selection in the context of numerical fluid mechanics. In particular, they presented a set of 12 features for their physical relevance and proper methodology for the design of the feature space. In order to be applicable to RANS models, the features should first be formulated only from the mean flow quantities in order to keep their relevance when no high-fidelity data is available. The second valuable property of the set of feature is their transferability to an other geometry. For this reason the input features should be Galilean invariant, non-dimensional and constructed from local flow quantities that are independent of the grid. The features should therefore be constructed from the mean pressure P, the mean velocity U, the mean density ρ and their gradients, along with the molecular viscosity ν, the eddy viscosity ν_T and the distance to the nearest wall λ.

The set of input features used in this work are presented in Table 6.2. To be clear, the input $\boldsymbol{\eta}_{d,m}$ in the training data sets are described by the vector $\boldsymbol{\eta} = (\eta_1, ..., \eta_h, ..., \eta_{N_\mathcal{H}})^T$, corresponding to the

10 features from Table 6.2. This set of features has been largely drawn from [5] with a few notable exceptions. First, the "vortex stretching" feature is excluded as it is non-zero only for tri-dimensional flows and our test scenarios are 2-D. We also excluded the "cubic eddy viscosity comparison" as the models in the mixing all are linear, in reason of their use of the Boussinesq hypothesis. In more recent works, Wang *et al.* [38] have proposed an additional feature based on the streamline curvature, normalized by a user-specified characteristic length scale of the mean flow. This feature has led to interesting results, however it is not considered in this work as we choose to keep features independent of any characteristic length scale. Finally, the η_2 feature is not strictly speaking Galilean invariant in reason of the normalization term $0.5U_iU_i$. In a context of a compressor with rotating parts, such feature should have been adapted to ensure invariance. However in the context of a fixed NACA 65 $V103$ compressor cascade, we use the η_2 as described in [5].

We also adopt the normalization from Ling and Templeton [5] for the set of features. Each normalized feature η_h (except for η_3) of the input vector $\boldsymbol{\eta}$ is formulated as

$$\eta_h = \frac{A_h}{|A_h| + |B_h|} \tag{6.19}$$

with A_h the raw input feature and B_h the normalization factor. This normalization has multiple benefits such as guarantying that the input features range in $[-1.0, 1.0]$ and thus reducing the probability of extrapolating for an unseen scenario, while limiting the values of η_h approaching zero. There is no additional normalization for η_3 as this feature is natively non-dimensional and in a restricted range, *i.e.* $[0.0, 2.0]$. Such normalization is well known in the machine-learning community and consistently applied to enhance the prediction of classical regression methods.

The features presented in Table 6.2 are classical quantities for the RANS modeling community. We present here three of the features for illustrative purpose. The first feature η_1 is the well-known Q-criterion, a Galilean invariant often used for the identification of vortices. The third feature η_3 is the turbulence Reynolds number, which is a natural quantity for describing turbulent flows. Finally, the sixth feature η_6 is a laminar (ν) to turbulent (ν_T) viscosity ratio and therefore directly based on the model output.

For the sake of completeness, let us note that Ling *et al.* [117] have since proposed a more general approach to the feature selection problem. The goal is to mitigate the subjectivity of the user choice by automatically constructing a set of features for the Reynolds stress from a basis of invariants of

Feature	Description	Formula	Feature	Description	Formula
η_1	Normalized Q criterion	$\frac{\|\|\mathbf{\Omega}\|\|^2 - \|\|\mathbf{S}\|\|^2}{\|\|\mathbf{\Omega}\|\|^2 + \|\|\mathbf{S}\|\|^2}$	η_6	Viscosity ratio	$\frac{\nu_T}{100\nu + \nu_T}$
η_2	Turbulence intensity	$\frac{k}{0.5U_iU_i + k}$	η_7	Ratio of pressure normal stresses to normal shear stresses	$\frac{\sqrt{\frac{\partial P}{\partial x_i}\frac{\partial P}{\partial x_i}}}{\sqrt{\frac{\partial P}{\partial x_j}\frac{\partial P}{\partial x_j}} + 0.5\rho\frac{\partial U_k^2}{\partial x_k}}$
η_3	Turbulent Reynolds number	$\min\left(\frac{\sqrt{k}\lambda}{50\nu}, 2\right)$	η_8	Non-orthogonality marker between velocity and its gradient [28]	$\frac{\left\|U_kU_l\frac{\partial U_k}{\partial x_l}\right\|}{\sqrt{U_nU_nU_i\frac{\partial U_i}{\partial x_j}U_m\frac{\partial U_m}{\partial x_j}} + \left\|U_iU_j\frac{\partial U_i}{\partial x_j}\right\|}$
η_4	Pressure gradient along streamline	$\frac{U_k\frac{\partial P}{\partial x_k}}{\sqrt{\frac{\partial P}{\partial x_j}\frac{\partial P}{\partial x_j}U_iU_i} + \left\|U_l\frac{\partial P}{\partial x_l}\right\|}$	η_9	Ratio of convection to production of k	$\frac{U_i\frac{\partial k}{\partial x_i}}{\|\overline{u_j'u_l'}S_{jl}\| + U_l\frac{\partial k}{\partial x_l}}$
η_5	Ratio of turbulent time scale to mean strain time scale	$\frac{\|\|\mathbf{S}\|\|k}{\|\|\mathbf{S}\|\|k + \varepsilon}$	η_{10}	Ratio of total Reynolds stresses to normal Reynolds stresses	$\frac{\|\|\overline{u_i'u_j'}\|\|}{k + \|\|\overline{u_i'u_j'}\|\|}$

Table 6.2: Ensemble of input features used in this study. The features were largely drawn from [5].

the input tensors $\mathcal{Q} = \{\mathbf{S}, \mathbf{\Omega}\}$, respectively the strain-rate and rotation-rate tensors, by means of the Cayley-Hamilton theorem [118]. It results in a basis of 6 non-trivial invariants, which are then used as features. This method has the advantage of being universal and easily transferable to new physics, but naturally lacks physical intuition for the problem at hand. In order to address this lack of physical input in the choice of the features, Wu *et al.* [39] added the pressure gradient ∇P and the TKE gradient ∇k to the basis of tensors $\mathcal{Q}$, *i.e.* $\mathcal{Q} = \{\mathbf{S}, \mathbf{\Omega}, \nabla P, \nabla k\}$, which leads to a basis of invariants consisting of 47 features. Finally, they considered three additional features from the original work of Ling and Templeton (corresponding to η_3, η_5 and η_2 in Table 6.2) in reason of their clear physical interpretations, increasing the number of features up to 50. The major downside of this method is evidently the dimensionality of the input features vector, which can be repellent if the beneficial gain is not straightforward. In this chapter, we stick with the original paper from Ling and Templeton [5] and use the 10 features presented in Table 6.2.

6.4 Results

In this section, we present various XBMA predictions for two of the selected NACA 65 V103 configuration scenarios and the 4 LEVM RANS models described in Chapter 2, namely, the Spalart–Allmaras, Wilcox' $k-\omega$, Launder–Sharma $k-\varepsilon$ and Smith's $k-l$ turbulence models.

First the predictive capability of the method is assessed on a simple case: the XBMA is trained on scenario S_2 and tested on S_2. This configuration is the most likely to be successful, and therefore

should help us highlight the influence of the parameters of the algorithm. In a second step, the XBMA method is confronted with the challenge of predicting flows outside the set of training scenarios: we train the XBMA on three scenarios and predict on the fourth. We choose to train the algorithm on scenarios $\{S_2, S_3, S_4\}$ and predict on S_1, in order to have the angle of attack of the prediction scenario outside the range of the angle of attacks of the training scenarios. As described in Chapter 4, S_1 has a severely off-design angle of attack and also the lowest of the four available scenarios which makes this scenario in extrapolation with respect to the training scenarios. For this reason, training on scenarios $\{S_2, S_3, S_4\}$ and predicting on S_1 represents a challenging configuration for assessing XBMA predictions outside the training set.

These two first steps are based on the EARSM $k-kL$ reference data, which allows us to evaluate the influence of the number of data on the XBMA, with the following methodology. A full-data XBMA, noted $XBMA_1$, is first constructed by fitting the XBMA on a complete data set, *i.e.* 40080 data per scenario, which corresponds to the configuration where $N_{thin} = 1$ in Table 6.1. This prediction should be considered as the limit of the method: as the fitting is made on the complete data set, it is expected that $XBMA_1$ would be the most accurate for the prediction on the same scenario, but could lead to overfitting for a prediction on an unseen scenario. This configuration has also the clear benefit of mimicking the case in which numerical high-fidelity data such as LES are available and used for the training phase. Unfortunately, full LES data remains rare for turbomachinery configurations, and XBMA predictive capability should therefore be tested in context of rare data. We construct a second XBMA model, noted $XBMA_2$, using 820 data per scenario, which corresponds to the configuration where $N_{thin} = 8$ in Table 6.1. This number of data is compatible with the use of experimental data and roughly the same as in a well resolved experimental campaign.

Finally, we would like to push the XBMA method to the limit by considering a very unfavorable context, which corresponds to the case of learning on the six LES profiles available in the work of Leggett alone, for the prediction on an unseen scenario. This case is indeed the most challenging, as it involves both prediction for a scenario outside the training set and training on few and very localized data, *i.e.* a data set only sparsely describing the input features space. We refer to this XBMA model as the $XBMA_3$.

In the following of this section, we focus on a vector of prediction QoIs consisting of a profile of

the tangential velocity on the suction side (normalized with the maximum velocity for each profile) and one of the normalized total pressure loss in the wake. For each QoI, the $XBMA$ results are first compared on the model probabilities maps and the vector of prediction QoIs. Finally, an histogram summarizes the mean-squared error (MSE) of the XBMA models and compares them with the baseline RANS models. In the rest of this chapter, we present the XBMA prediction in blue color, with one or two standard deviation confidence interval in the same color. Red color is reserved for the reference data described in Section 6.3.1. Green, orange, yellow and gray colors are used respectively for the baseline $k-\varepsilon$, $k-\omega$, $k-l$ and Spalart - Allmaras models. It includes both model probability $p\left(\delta^m\right)$, when model probabilities profiles are presented, and baseline RANS predictions, when QoI profiles are presented. Finally, the XBMA prediction being a convex weighted average of the predictions of the four RANS models, it cannot lie outside of the hull bounded by the four RANS predictions. In the rest of the chapter, this hull is delimited by the gray-shaded area and called the accessible area.

6.4.1 Prediction on the same scenario S_2

In this section, the XBMA algorithm is trained on EARSM $k-kL$ reference data data coming from scenario S_2 and used for the prediction on the same scenario.

6.4.1.1 Maps of probabilities

Fig. 6.3 presents the maps of the probabilities of models $p\left(\delta^m\right)$ produced with the $XBMA_1$ for the 4 RANS models in the mixing. The prediction have been obtained in the feature space and then brought back in the physical space (x, y, z) to produce visualizations. The first observation is that each model is given a probability of 0.25 far from the blade. This is a desired property as the theory of RANS modeling states that RANS models give the same results on potential flows and therefore should be given the same cost function in these regions.

However, the probabilities of models are significantly diverging from the reference value of 0.25 in the vicinity of the blade and in the wake. Fig. 6.3a shows that the $k-\varepsilon$ model is generally associated with lower probabilities in the wake and on the suction and pressure sides. The $XBMA_1$ has learned that the $k-\varepsilon$ model is the less likely to accurately predict the reference data far from the blade. On the contrary, the three remaining models are globally given higher probabilities. First, the Spalart-Allmaras model presented in Fig. 6.3b is given a very high probability on the pressure side and a high

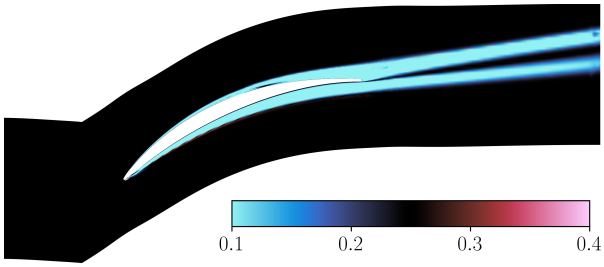

(a) Probability of the $k - \varepsilon$ model.

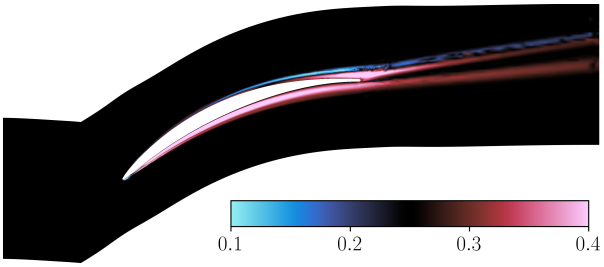

(b) Probability of the Spalart-Allmaras model.

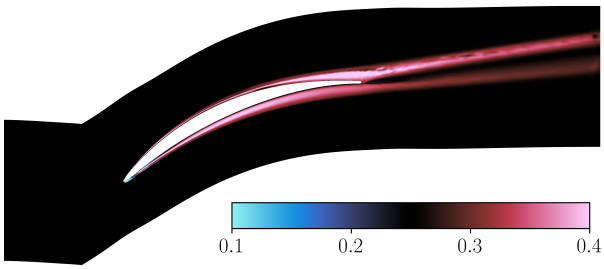

(c) Probability of the $k - l$ model.

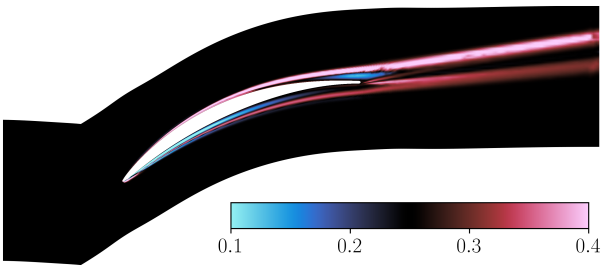

(d) Probability of the $k - \omega$ model.

Figure 6.3: Probability of the four RANS models obtained with $XBMA_1$ for a prediction on S_2, after training on S_2.

probability around the upper part of the trailing edge but a probability closer to the reference in the wake. Similarly the $k - l$ model (Fig. 6.3c) is given a very high probability on the suction side and a rather high probability on the pressure side. We also notice a very high probability in the wake which corresponds to the expected behaviour as the dynamics in the wake is mostly the result of the viscosity created upstream close to the blade. It is therefore an expected property of the algorithm that high probabilities in source regions lead to a high probability in target regions. Seeing a continuity on the model probability between the blade and the wake shows that the XBMA is effectively predicting on the underlying physics. The same observations naturally hold for the other models. Finally, the Fig. 6.3d presents the probability of the $k - \omega$ model. This model is given the highest probability on the first half of the suction side, which is then continued by a thin and detached band of low probability on the second half of the suction side. This figure also illustrates one of the positive aspect of the method, namely the precision in the description of the physical phenomena at stake. The lower part of Fig. 6.3d is also presenting the same result, with a thin layer of low probability close to the blade, superposed with a thin layer of high probability. Those results clearly indicate that each RANS model has an area for which it best performs at predicting the EARSM reference data. The Spalart-Allmaras

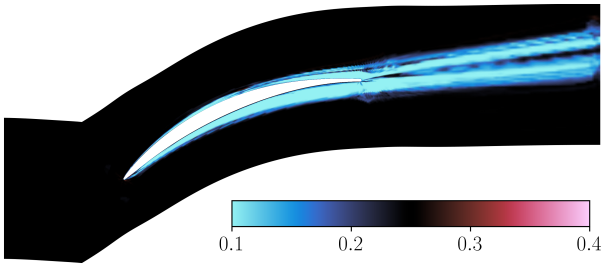

(a) Probability of the $k - \varepsilon$ model.

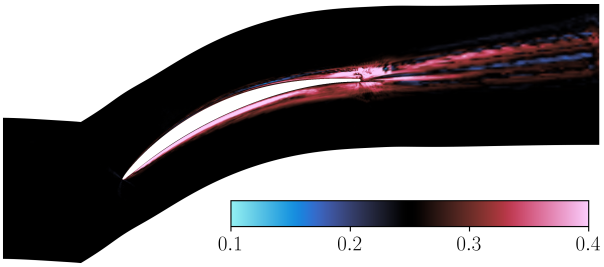

(b) Probability of the Spalart-Allmaras model.

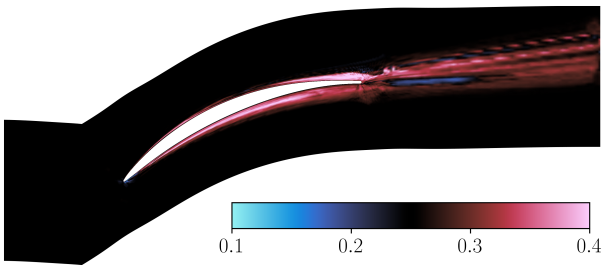

(c) Probability of the $k - l$ model.

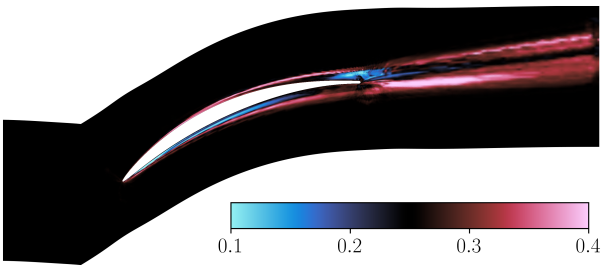

(d) Probability of the $k - \omega$ model.

Figure 6.4: Probability of the four RANS models obtained with $XBMA_2$ for a prediction on S_2, after training on S_2.

model is the most probable model on the pressure side. The $k - \omega$ model over-predicts turbulence levels close to the blade but produces accurate predictions in the outer part of the boundary layer. On the contrary, both Spalart-Allmaras and $k - l$ models are able to accurately predict inner part of the boundary layer on both the suction side and the pressure side. However, one should not too hasty conclude that the $k - l$ model is the best performing RANS model: RANS models predictive capabilities differ from one scenario to another as presented in the next section 6.4.2.

Fig. 6.4 presents the maps of the model probability obtained with the $XBMA_2$, *i.e.* the XBMA trained on 820 data. Similarly to Fig. 6.3a, the $k - \varepsilon$ model is given an overall lower probability than the other models. The Spalart-Allmaras model is preferred on the pressure side and close to the trailing edge while the $k - l$ model is assigned a high probability practically all around the blade. Finally the $k - \omega$ model is assigned low probability in the inner part of the boundary layer and high probability in the outer part, like in Fig. 6.3d. It is clear that those maps exhibit the same general results as the maps obtained after training on the complete data set, albeit a bit noisier. The observed noise is mostly caused by the interpolation error which occurs in the prediction data set. As the

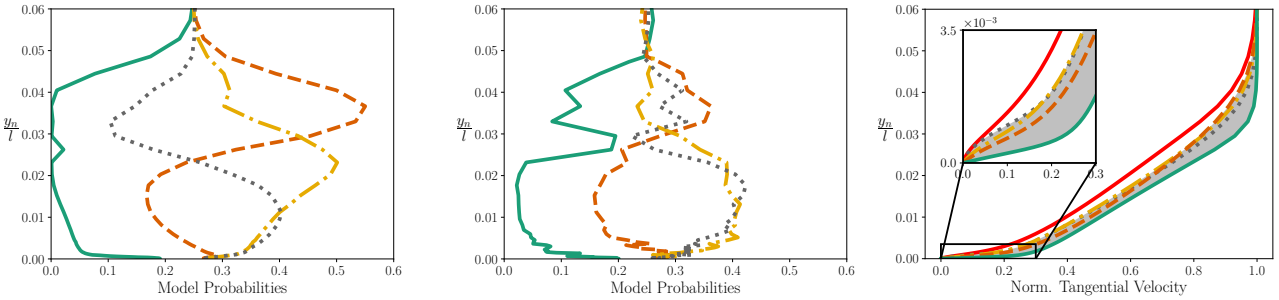

(a) Model probabilities obtained with $XBMA_1$.

(b) Model probabilities obtained with $XBMA_2$.

(c) RANS predictions and reference profile.

Figure 6.5: Prediction of the model probabilities of the normalized tangential velocity profile at $\frac{x}{l} = 0.90$ for $XBMA_1$ and $XBMA_2$, for a prediction on S_2 and training on S_2.
$k-\varepsilon$ model (——), $k-\omega$ model (- - -), $k-l$ model (-·-·-) and Spalart-Allmaras model (·····). Accessible area appears in ▭ and reference data in (——).

learning was made on fewer samples, the feature space is less likely to be completely described than in the context of $XBMA_1$ and local variations appear in the model probabilities maps. Seeing the results obtained with 820 data chosen without optimal sensor placement (OSP) methods makes us optimistic that a XBMA harnessing OPS could lead to results even closer to the ones obtained with $XBMA_1$ with a fraction of the probes used in $XBMA_2$. Nevertheless we must say that noisy maps are not a problem, as the space-dependent probabilities $p(\delta^m)$ are not physical quantities, such as velocity or pressure, that need to be continuous, but a mathematical distribution; the reconstructed QoI do need to be continuous - what they are - but the continuity requirement should be relaxed for the model probabilities.

6.4.1.2 Prediction of QoI profiles

As explained in subsection 6.2.2, the XBMA algorithm produces space-dependent model probabilities from which any desired QoI can be reconstructed. In the following paragraphs, two one-dimensional profiles reconstructed from the model probabilities in Figures 6.3 and 6.4, and the RANS baseline predictions, are presented. The two profiles are the normalized tangential velocity on the suction side at $\frac{x}{l} = 0.90$ and the normalized total pressure in the wake at $\frac{x}{l} = 1.20$, l being the axial chord. The same general conclusions hold for other QoIs and other locations in the flow, not presented here for the sake of conciseness. Fig. 6.5 is illustrating the prediction of the model probabilities of the normalized tangential velocity profile at $\frac{x}{l} = 0.90$. Figures 6.5a and 6.5b show the model probabilities

for $XBMA_1$ and $XBMA_2$, and Fig. 6.5c illustrates the comparison between the RANS baselines and the reference data on this profile. The y-axis represents the normalized distance to the wall y_n/l, y_n being the distance to the blade, and the x-axis represents the model probabilities, for Figures 6.5a and 6.5b, and the normalized tangential velocity, for 6.5c.

The Figure 6.5a shows the model probabilities on this profile in case of $XBMA_1$. In coherence with Fig. 6.3, each model is given a 0.25 probability outside of the boundary layer. The $k-\varepsilon$ model is given a lower probability than the other models, falling to zero on the large majority of the boundary layer. The three other models reach their maximum probability at different distances from the wall: the Spalart-Allmaras, $k-l$ and $k-\omega$ model are respectively assigned a higher probability in the lower, mid and upper part of the boundary layer. The $k-\omega$ model is for example given a probability lower than 0.25 close to the blade, but the highest probability around 0.50 for $\frac{y_n}{l} = 0.035$.

The Figure 6.5b presents the model probabilities obtained with $XBMA_2$. The probabilities assigned to each model in this figure are in good agreement with the results produced by $XBMA_1$, the XBMA trained on the complete data set. The $k-\varepsilon$ model is consistently assigned lower probability on the complete boundary layer. On the contrary, the $k-l$ and Spalart-Allmaras models are preferred in the inner part of the boundary layer and the $k-\omega$ model in the outer part. The difference between the model probabilities produced by $XBMA_1$ or $XBMA_2$ lies in the amplitude of the predictions: XBMA trained on fewer data remains closer to the 0.25 value, while XBMA trained on complete data set assigns more extreme values to the models. This result seems to indicate that the model probabilities in this case lacks information about the flow. Sensor placement methods from the OPS community could help select probes providing more information on the flow, while maintaining (or even reducing) the number of sensors used for the training. One of those regions seems to appear around $\frac{y_n}{l} = 0.03$, with all models returning briefly to 0.25 without easily explainable reasons. Considering additional data in this regions would prevent such responses and would further bring model probabilities from Fig. 6.5b closer to model probabilities from Fig. 6.5a.

The Figure 6.5c helps understand why the space-dependent model probabilities provided above are meaningful. The idea behind the XBMA algorithm is simply to rank the models in each region of the flow. It is therefore useful to evaluate if the model probabilities indeed correspond to the predictive accuracy of each model. This figure shows the reference data, the four RANS baseline predictions along with the accessible area : the space delimited by the different baseline predictions. As the XBMA is a

convex linear combination between the RANS models, the XBMA prediction must lie within the space delimited by the models. The presence of this zone enables the comparison of the XBMA prediction with the best possible prediction in the rest of the figures. On Fig. 6.5c the $k-\varepsilon$ model is rightfully assigned lower probabilities as it is the worst performing model in this case. The three other RANS models are closer to the reference, but we can see on the zoomed figure that the $k-\omega$ model is worse performing than the Spalart-Allmaras and $k-l$ models close to the blade, which explains the lower probability it received in that corresponding region of Figures 6.5a and 6.5b. Similarly, the Spalart-Allmaras prediction is slightly deteriorating in the outer part of the boundary layer, in accordance with the drop in its probability around $\frac{y_n}{l} = 0.03$ for both $XBMA_1$ and $XBMA_2$.

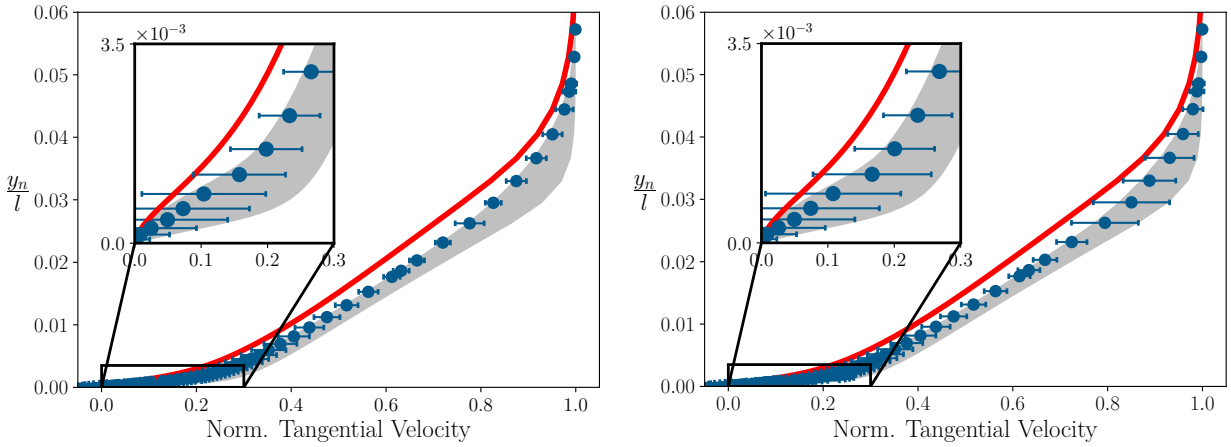

(a) $XBMA_1$ prediction.

(b) $XBMA_2$ prediction.

Figure 6.6: Reconstruction of the normalized tangential velocity profile at $\frac{x}{l} = 0.90$ for $XBMA_1$ and $XBMA_2$, after the training and prediction on S_2.
Reference data (—), Accessible area ▭ , $E[\Delta] \pm 2\sqrt{Var[\Delta]}$ (-●-).

Fig. 6.6 is illustrating the corresponding reconstructed normalized tangential velocity profile at $\frac{x}{l} = 0.90$ for the $XBMA_1$ and $XBMA_2$. In those figures, the same y-axis as in Figures 6.5a and 6.5b is adopted for clarity. On the other hand, the x-axis represents the normalized tangential velocity.

First the reconstructed $XBMA_1$ prediction and confidence interval are presented in Fig. 6.6a. In this case the confidence intervals illustrates what previous authors [3] have called the *within models* variance: it is a measure of the influence of the disagreement between the models on the variance of the prediction. It must serve as a spatial marker, identifying regions of the flow in which models are in good agreement (typically far from the blades) or in strong discordance. This confidence interval is to

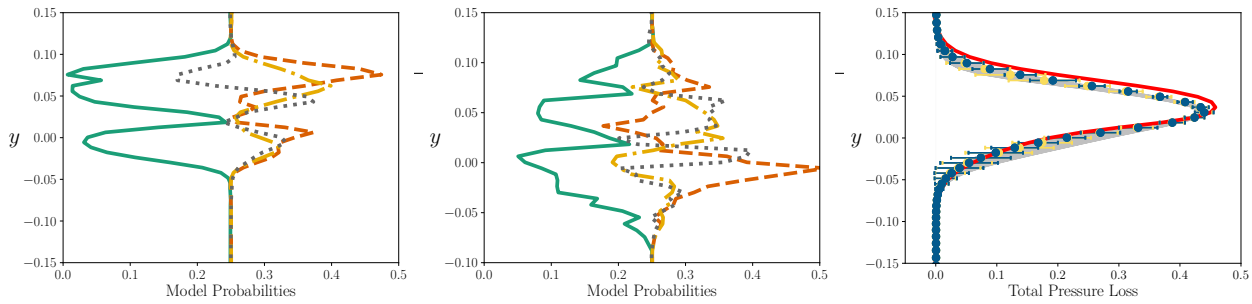

(a) Model probabilities obtained with $XBMA_1$.

(b) Model probabilities obtained with $XBMA_2$.

(c) $XBMA_1$ and $XBMA_2$ predictions superposed.

Figure 6.7: Prediction of the model probabilities and reconstruction of the corresponding QoI in case of the normalized total pressure wake profile at $\frac{x}{l} = 1.20$ for $XBMA_1$ and $XBMA_2$, after training and prediction on S_2.
$k-\varepsilon$ model (—), $k-\omega$ model (- - -), $k-l$ model (-·-) and Spalart-Allmaras model (·····). Reference data appears in (—). Accessible area ▭ , $E[\Delta] \pm 2\sqrt{Var[\Delta]}$ for $XBMA_1$ (—●—), $E[\Delta] \pm 2\sqrt{Var[\Delta]}$ for $XBMA_2$ (—●—).

be considered in relation to the accessible area: regions where models are in strong disagreement are likely to have a large accessible area and confidence intervals, and vice-versa. The XBMA prediction yields good results, consistently selecting the adequate border of the accessible area. None of the baseline RANS models being able to reach the reference data, the prediction simply cannot be more accurate. The confidence intervals capture well the reference data in the vicinity of the blade, but fail to in the upper part of the boundary layer. One solution to improve both the prediction and the confidence intervals might be to further expand the ensemble of models $\mathcal{M}$. This extension would increase the diversity in the baseline predictions and would thus help the accessible area reach the reference data. This would ultimately allow the XBMA prediction to get closer to the reference data, while simultaneously making the confidence intervals to encompass the reference data. However this step is not trivial in our case, as others Boussinesq models are less than likely to be able to capture the reference data, mostly because of the linear mathematical structure shared by this class of models. This behavior will be even harder to achieve for 3-D flows with complex physics.

Fig. 6.6b presents the $XBMA_2$ prediction and confidence interval for the same QoI profile. This prediction is really close to the prediction from Fig. 6.6a: this is an expected behavior since the predictions are constructed from the model predictions, the latter being very similar. The influence of the drop of probability around $\frac{y_n}{l} = 0.03$ is visible on the prediction: as the model probabilities are locally close to 0.25, the accuracy of the prediction is deteriorated and the variance of the prediction is clearly increased.

We now present in Fig. 6.7 the model probabilities and XBMA reconstruction for the normal-

ized total pressure loss profile in the wake at $\frac{x}{l} = 1.20$. In those figures the y-axis represents the transverse position centered on the trailing edge and the x-axis represents the model probabilities, for Figures 6.7a and 6.7b, and the normalized total pressure loss, for Fig. 6.7c. Fig. 6.7a presents the model probabilities for the $XBMA_1$. In coherence with Figures 6.3 and 6.4 each model is assigned a standard probability of 0.25 outside the wake. Model probabilities then follow the same pattern on each side of the wake: low probability for the $k-\varepsilon$ model, while the 3 other RANS models are given approximately the same higher value. One interesting result is that the outer part of the wake (corresponding to the suction side) presents exactly the same model probability profiles as the suction side at $\frac{x}{l} = 0.90$ on Fig. 6.5a. This is due to the fact that the features are functions of the invariants of the mean flow. As those quantities are advected through the flow, so are the features built upon. The cost function, and ultimately the model probabilities, being tested on these features, it produces the same response as in Fig. 6.5a. This result indicates that the XBMA method is able to deliver a prediction deeply rooted in the underlying physics, as desired when using local features.

On Fig. 6.7b the model probabilities for the $XBMA_2$ model are presented. They are in good agreement, although noisier, with the model probabilities presented in Fig. 6.7a. The $k-\varepsilon$ model is assigned lower probabilities on both sides of the wake with a peak around $y = 0.07$ which could also result from a lack of information in the training data set. The model probabilities for both the Spalart-Allmaras and $k-l$ models are of the same order of magnitude than for $XBMA_1$. On the other hand, $k-\omega$ is assigned a very high probability on the lower side of the wake, close to the top of the wake. This behavior is not observed on Fig. 6.7a. It turns out that this difference does not affect the XBMA prediction as every RANS model in this region gives the same prediction. We do not show an equivalent to Fig. 6.5c in this case for brevity concerns but the results are similar.

Finally, the Fig. 6.7c presents the two XBMA prediction superposed for the normalized total pressure loss profile in the wake at $\frac{x}{l} = 1.20$, the x-axis being the total pressure loss. In contrast with Fig. 6.6a, where the reference data remains on the inner side of the accessible area, in this case it is switched from the inner side of the wake for $y \leq 0.03$ to the outer side of the wake for $y \geq 0.03$. The XBMA predictions (respectively blue for the $XBMA_1$ and light-yellow for the $XBMA_2$) are nevertheless successful at predicting the reference data, within the limits of the accessible area. For $y \leq 0.03$ the accessible area encompass the reference data, which allows both XBMA predictions to accurately predict the reference data. On the contrary, the reference data lies outside the accessible

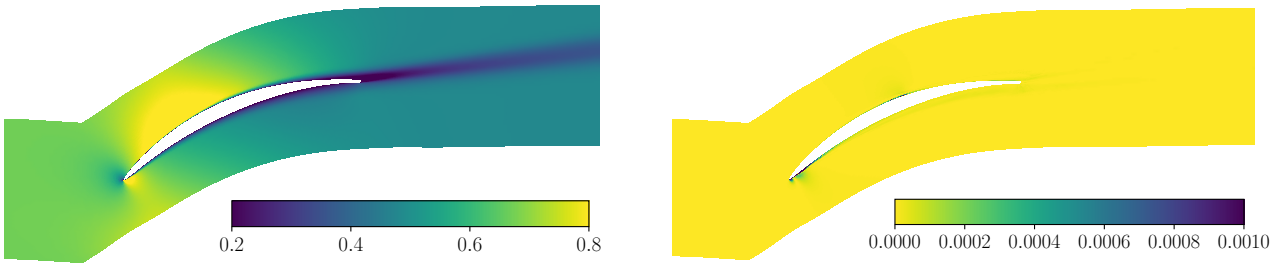

(a) Mean of the prediction.

(b) Variance of the prediction.

Figure 6.8: 2-D contours of the Mach number field obtained with $XBMA_2$, after training and prediction on S_2.

area for $y \geq 0.03$. In this region, the $XBMA_1$ is better at predicting the reference than $XBMA_2$, adequately capturing the right side of the accessible area. The reason for the drop in performance for the $XBMA_2$ in this region is clear on Fig. 6.7b. In this area, the $k-\varepsilon$ model is assigned a probability of roughly 0.15, when the $XBMA_1$ predicts a probability close to zero. The $k-\varepsilon$ model being less accurate than the other models, the XBMA prediction is deteriorating. Ultimately, the $XBMA$ is generally accurate at predicting the reference data and produce very convincing results. As previously explained, the maximum of the probability of $k-\omega$ for $XBMA_2$ around $y = 0.00$ has no clear effect on the final prediction as the baselines are very close to each other in this region. The confidence intervals capture the reference data on the the lower part of the wake while they fail for $y \geq 0.03$.

For the sake of completeness, we present in Fig. 6.8 the 2-D field reconstruction of the mean and variance of the Mach number obtained with $XBMA_2$. The 2-D fields are smoothly reconstructed, without any instability. This observation holds for other QoI as well.

6.4.1.3 Error comparisons on multiple QoIs

As a concluding remark on this case, Fig. 6.9 shows the MSE for four different QoIs, averaged over the complete mesh and normalized by the error of the $k-\varepsilon$ model, which has consistently the largest error. The four QoIs are velocity, pressure, skin friction and total pressure. Green, orange, yellow and gray colors are again used respectively for the baseline $k-\varepsilon$, $k-\omega$, $k-l$ and Spalart-Allmaras models. The lighter pink and darker magenta are used respectively for the $XBMA_1$ and $XBMA_2$.

First, this figure indicates that RANS models sometimes give very different predictions, even for 2-D configuration like the NACA 65 compressor cascade. For the velocity for example, the Spalart-

Allmaras model is found to be the closer to our reference, while the $k-\omega$ model is associated with the larger error, with the exception of the $k-\varepsilon$. On the other hand, the $k-\omega$ model is found to be the closer to our reference for the skin friction, and the Spalart-Allmaras model is less accurate. It means that some RANS models are better a predicting some quantities than others. The $k-\varepsilon$ is the less accurate baseline model for each QoIs, which is in accordance with Figures 6.3a and 6.4a where this model is systematically assigned a lower probability. It is a positive signal for the algorithm to be able to accurately identify the least performing model and to assign it a low probabilities. The Spalart-Allmaras model is found to be the best performing model on velocity, pressure and total pressure. The $k-l$ model is the second worst performing model on pressure, skin friction and total pressure and the second best performing on the velocity. Finally the $k-\omega$ model has the lowest MSE for the total pressure and the skin friction, the second lowest for pressure and the second highest for velocity. It is particularly interesting to compare the MSE of the velocity and the skin friction, which is effectively computed from the gradient of the velocity close to the blade. The $k-\omega$ has the lowest MSE for the skin friction, while the Spalart-Allmaras model has the lowest MSE for the velocity. This result indicates that while being more accurate at predicting the velocity and its gradient close to the blade, the $k-\omega$ has a higher MSE on the rest of the domain than the Spalart-Allmaras model. The $k-l$ model is associated with the second larger error on the skin friction, which could appear to be in contradiction with Figures 6.3c and 6.4c where the model is highly likely all over the blade. Further investigations have shown that this is due to the very poor performance of the $k-l$ model on the suction side close to the leading edge, which radically deteriorates its average performance.

Finally, some ML models applied in physical problems have the disadvantage of being very efficient on the quantities they have been trained on, while deteriorating the prediction on other QoIs. Fig. 6.9 proves that the XBMA algorithm does not behave like this. Both of the XBMA predictions perform really well for each QoI : for velocity, pressure and skin friction both predictions are as good as the best performing baseline model. When it comes from the quantity of calibration, *i.e.* total pressure, the XBMA clearly improves predictions with respect to the best RANS model. The same result is observed for $XBMA_1$ and for $XBMA_2$ to a lesser extent. This is worth being pointed out: the prediction for the calibration variable is better than the best baseline model, while guaranteeing the same level of accuracy than the best baseline model on the other QoIs. In addition, the XBMA seems not to lose in predictive accuracy when using a limited number of data in the training, as illustrated

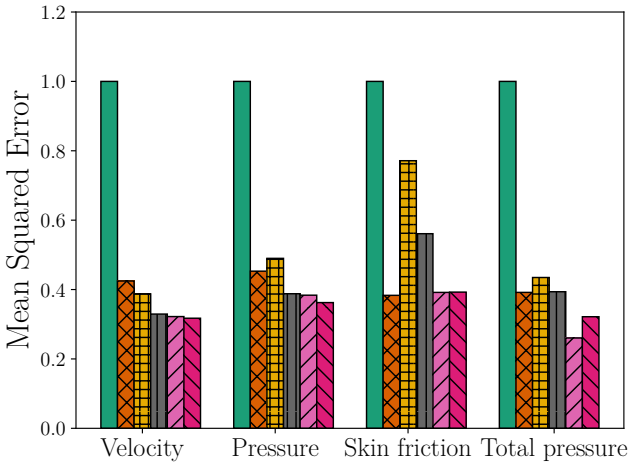

Figure 6.9: Mean-squared error of the four QoIs normalized by the MSE of the $k-\varepsilon$ model, after the training and prediction on S_2.
$k-\varepsilon$ model (), $k-\omega$ model (), $k-l$ model ( ) and Spalart-Allmaras model (), $XBMA_1$ () , $XBMA_2$ ()

by the $XBMA_2$ results.

6.4.2 Prediction for an unseen scenario

The XBMA method has been proven efficient at training and predicting on the same scenario. The next step is to evaluate its ability to predict flows outside the set of training scenarios. In the following subsection, XBMA algorithm has been trained on data from scenarios $\{S_2, S_3, S_4\}$ and used for prediction on the unseen scenario S_1. As the training is made on multiple scenario, the creation of the training data sets must first be detailed. From now on, $XBMA_1$ refers to the XBMA trained on the complete EARSM reference data sets of each scenario (*i.e.* 120240 data in total) and $XBMA_2$ refers to the XBMA trained on 820 data of each scenario (*i.e.* 2460 data in total). We choose S_1 as the prediction scenario because it is the only one for which the accessible area incorporates the reference data. Predictions on the other three scenarios bring results which are similar to the prediction on a seen scenario.

6.4.2.1 Maps of probabilities

Fig. 6.10 presents 2-D fields for the model probabilities $p\left(\delta^m\right)$ as a function of the physical space for the four RANS models considered in the case of the $XBMA_1$. The maps obtained for $XBMA_2$

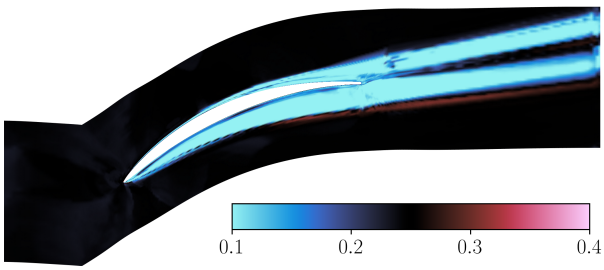

(a) Probability of the $k-\varepsilon$ model.

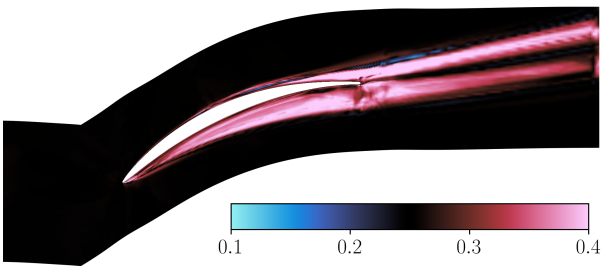

(b) Probability of the Spalart-Allmaras model.

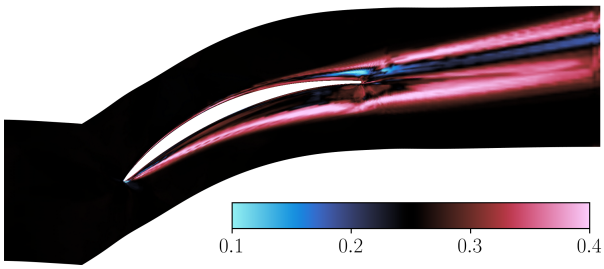

(c) Probability of the $k-l$ model.

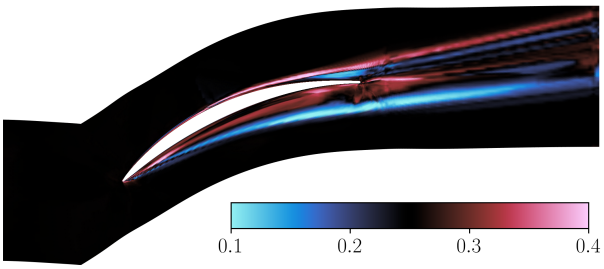

(d) Probability of the $k-\omega$ model.

Figure 6.10: Probability of the four RANS models obtained with $XBMA_1$ after training on $\{S_2, S_3, S_4\}$ and prediction on S_1.

are very similar to the maps presented in Fig. 6.10 and therefore not reported here for the sake of brevity. The wake in this case is significantly wider and lower than the wake in Fig. 6.3. This is due to the fact that the angle of attack for S_1 is severely lower than the angle of attack of the rest of the scenarios. As for $k-\varepsilon$ maps obtained in the case of a prediction on S_2, the $k-\varepsilon$ model is assigned low probabilities on Fig. 6.10a both in the vicinity of the blade and in the wake. The Spalart-Allmaras model in Fig. 6.10b is assigned high probabilities on both pressure and suction side, as well as in the wake. The region close to the trailing edge is particularly associated with high probabilities, by contrast with the other models that are systematically assigned lower probabilities. In contrast with the prediction on S_2, Fig. 6.10c shows that the $k-l$ model is assigned high probability only in the outer parts of the suction and pressure side boundary layers, but an intermediate probability of 0.25 on the pressure side and even low probability on the suction side close to the trailing edge. Finally, Fig. 6.10d shows that the $k-\omega$ model is assigned higher probabilities on the suction side for the outer part of the boundary layer and lower probabilities on its inner part, as in Fig. 6.3d. On the pressure side on the contrary, the $k-\omega$ model seems to be better performing on the inner part of the boundary layer rather than in the outer part, in opposition with Fig. 6.3d.

6.4.2.2 Prediction of QoI profiles

Fig. 6.11 presents the normalized total pressure in the wake at $\frac{x}{l} = 1.20$, the y-axis representing the transverse position centered on the trailing edge. On this figure, the model probabilities of $XBMA_1$ and $XBMA_2$ are presented on respectively Fig. 6.11a and Fig. 6.11b. In those figures the x-axis is the model probabilities. Both figures are very similar meaning that enough information is available after training on fewer data. As observed in the case of the prediction on scenario S_2, the XBMA trained on additional data has sharper model probabilities. On both of those figures, the $k-\varepsilon$ model is assigned lower probabilities, except for the center of the wake located around $y = 0.05$. The $k-\omega$ model is assigned very low probabilities in the lower part of the wake and higher probabilities on the upper part. Finally Spalart-Allmaras and $k-l$ models are assigned probabilities higher than 0.30, with the Spalart-Allmaras model reaching a probability close to 0.50. The Figure 6.11c presents the reconstructed prediction for $XBMA_1$ and $XBMA_2$, respectively in blue and light-yellow color. Both predictions are very close, which stems from the similarity of the model probabilities in Figures 6.11a and 6.11b. It is worth noticing that, for both XBMA models, the algorithm is able to predict the reference data almost perfectly whereas S_1 has not been included in the training data set. The XBMA thus exhibit strong generalization properties, even for a prediction scenario in extrapolation with the training scenarios.

In a stark contrast with Fig. 6.7c, Fig. 6.11c presents a large variance on the prediction. This behavior can be sourced in two main reasons. The first reason is that the RANS models are producing divergent predictions on this configuration, as indicated by the large accessible area - models are in closer agreement in the case of prediction on the same scenario S_2. The second reason is that the model probabilities are less informed on this configuration than on the same scenario configuration. Altogether the XBMA is shown to be very effective at predicting QoIs for which reference data lies within the accessible area.

For the sake of completeness, Fig. 6.12 shows the model probabilities and predictions for the normalized tangential velocity profile at $\frac{x}{l} = 0.90$. Figs. 6.12a and 6.12b show model probabilities while Fig. 6.12c shows the reconstructed predictions. Model probabilities presented in Fig. 6.12a are in close agreement leading to relatively similar XBMA predictions. The prediction presented in Fig. 6.12c is able to correctly estimate the reference data, even if both XBMA are not as successful

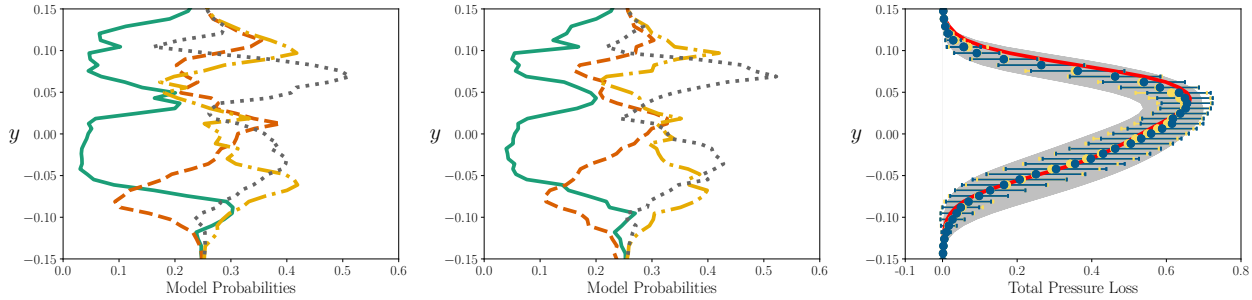

(a) Model probabilities obtained with $XBMA_1$.

(b) Model probabilities obtained with $XBMA_2$.

(c) $XBMA_1$ and $XBMA_2$ predictions superposed.

Figure 6.11: Prediction of the model probabilities and reconstruction of the normalized pressure wake profile at $\frac{x}{l} = 1.20$ for the $XBMA_1$ and $XBMA_2$ after training on $\{S_2, S_3, S_4\}$ and prediction on S_1. $k-\varepsilon$ model (—), $k-\omega$ model (- - -), $k-l$ model (-·-) and Spalart-Allmaras model (·····). Reference data (—), Accessible area ▭ , $E[\Delta] \pm \sqrt{Var[\Delta]}$ for $XBMA_1$ (—●—), $E[\Delta] \pm \sqrt{Var[\Delta]}$ for $XBMA_2$ (—●—).

at predicting this QoI for it is in the wake. The drop in predictive performance when comparing to Fig. 6.11 probably comes from the training, which used total pressure as the reference data and not velocity.

6.4.2.3 Error comparisons on multiple QoIs

Finally, we present in Fig. 6.13 the MSE for the same QoIs as in Fig. 6.9, but normalized by the error of the $k-l$ model, as it is the baseline model with the largest error on 3 out of 4 QoIs. This figure helps put into perspective the arguments that establish a baseline model as the most efficient RANS model. As previously observed in Fig. 6.9, the various RANS models are better performing on different QoIs. It is also worth noticing that the best RANS model for the prediction of a QoI heavily depends on the prediction scenario. For example, the average MSE on the pressure is the lowest for the Spalart-Allmaras model when predicting on S_2 but is now better described by the $k-\varepsilon$ model. For the same QoI, the $k-l$ model, which is in the performance range of the $k-\omega$ and Spalart-Allmaras model on S_2, is the worst performing model by far for the prediction on S_1. Observing large discrepancies within RANS predictions helps emphasize the need for a multi-model approach when studying CFD.

In Figure 6.13, the two XBMA predictions present clear improvements compared to the best RANS models, regardless of the QoI presented. For example, the MSE for the velocity is reduced by almost a third with respect to the best RANS model. Similarly to Fig. 6.9, $XBMA_1$ and $XBMA_2$ produce

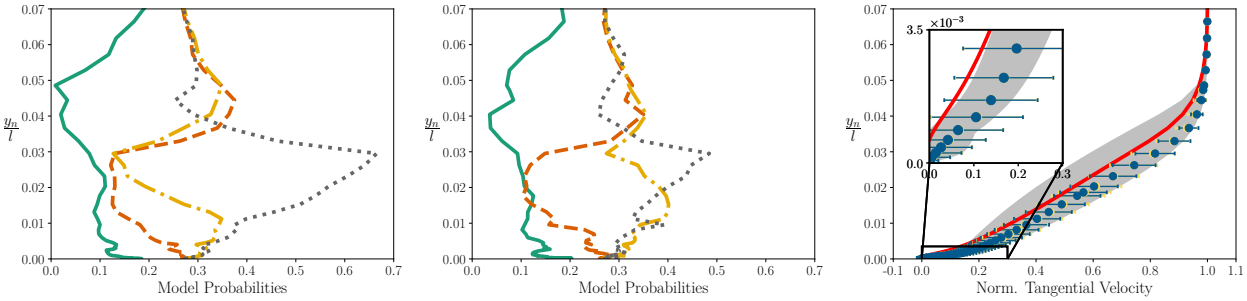

(a) Model probabilities obtained with $XBMA_1$.

(b) Model probabilities obtained with $XBMA_2$.

(c) $XBMA_1$ and $XBMA_2$ predictions superposed.

Figure 6.12: Prediction of the model probabilities and reconstruction of the normalized tangential velocity profile at $\frac{x}{l} = 0.90$ for the $XBMA_1$ and $XBMA_2$ after training on $\{S_2, S_3, S_4\}$ and prediction on S_1.
$k-\varepsilon$ model (—), $k-\omega$ model (- - -), $k-l$ model (-·-) and Spalart-Allmaras model (·····). Reference data (—), Accessible area ▭ , $E[\Delta] \pm 2\sqrt{Var[\Delta]}$ (—●—).

the same overall MSE average, which shows that large amounts of data might not be needed for an improvement of the prediction of those QoIs.

6.4.3 Prediction for an unseen scenario with very sparse LES data

In this section, the XBMA method is fed with a very sparse LES data set. The six profiles that are presented for the four scenarios S_1, S_2, S_3 and S_4 come from Leggett *et al.* [4] and are used as training sets for the XBMA. Note that only the results obtained after training on $\{S_2, S_3, S_4\}$ and predicting on S_1 are presented. This scenario is chosen to illustrate a challenging case in coherence with the rest of the study.

The six profiles considered are described in Chapter 4: they are composed of the four normalized tangential velocity profiles on the suction side taken at the 4 streamwise positions, at $\frac{x}{l} = 0.56,\ 0.64,\ 0.76$ and 0.99, and of the two normalized total pressure loss profiles at two positions downstream of the trailing edge ($\frac{x}{l} = 1.02$ and 1.10). This selection process results in selecting respectively 91, 90, 90 and 87 pieces of data for each velocity profiles, and respectively 137 and 79 in the wake. Ultimately, each scenario is described by 574 pieces of data. The position of the profiles are presented in Fig. 6.14. The probes are mostly located on the suction side, at the expense of the pressure side. However, the use of the feature space is supposed to help alleviate negative effects due to the lack of information coming from the pressure side: if the physics developing on the suction side can be

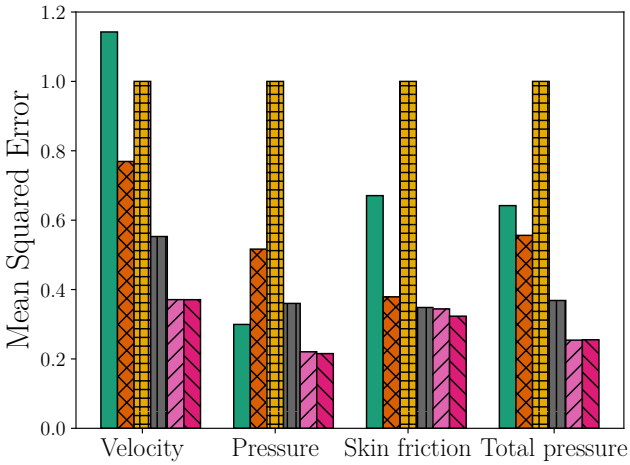

Figure 6.13: Mean-squared error of the four QoIs, normalized by the MSE of the $k-l$ model after training on $\{S_2, S_3, S_4\}$ and prediction on S_1.
$k-\varepsilon$ model (■), $k-\omega$ model (■), $k-l$ model (■) and Spalart-Allmaras model (■),$XBMA_1$ (■) , $XBMA_2$ (■).

described as an interpolation between the physics described in the 6 profiles and if the feature space is correctly describing this physics, then probes located on the pressure side may not be necessarily needed. Nevertheless, expecting the feature space to be accurately described by 6 localized profiles is unrealistically demanding. The close spatial localization of the profiles will lead to a close localization in the space of features, in reason of the continuity of the features. The division of the data in the feature space seems to be far from optimal for the regression setup considered in this study, but will certainly be useful as a challenging case for assessing the robustness of XBMA for very sparse data.

6.4.3.1 Maps of probabilities

Fig. 6.15 shows the maps of model probabilities $p(\delta^m)$ obtained after training on the LES data. The $k-\varepsilon$ model is assigned an overall lower probability than the other models. Nevertheless it has a higher probability on the lower border of the wake and close to the trailing edge on the pressure side. It could be interesting to see if incorporating data from the suction side tends to remove or rather reinforce this trend. The Spalart-Allmaras model is credited of a high probability especially close to the blade. This region of high probability is followed by a trail in the center of the wake. Contrary to the Spalart-Allmaras model, the $k-l$ model is assigned large probabilities on the outer part of the wake and a low probability close to the trailing edge. Finally, the $k-\omega$ model is assigned lower

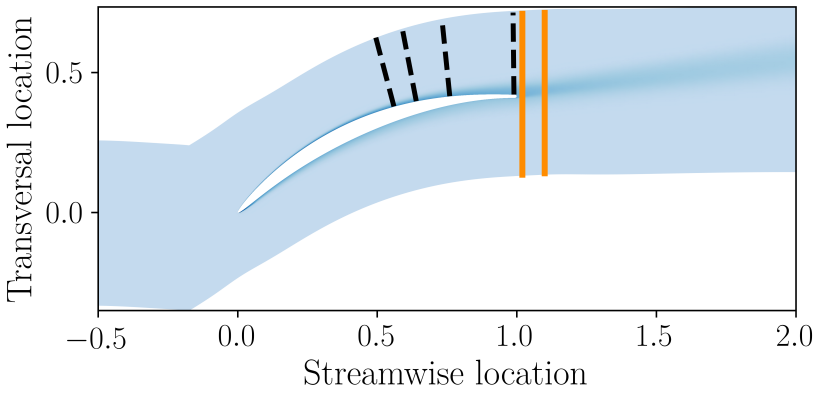

Figure 6.14: Location of the LES profiles from [4].
Tangential velocity (- - -) Total pressure loss profiles (—)

probabilities, most notably on the lower part of the wake. The last two figures show that the model probabilities on the lower part of the pressure side have been well informed from data mostly placed on the suction side. It seems to indicate that the feature space is rather correctly working as a way to produce an informed prediction from an algorithm trained on another part of the flow. Unfortunately we cannot evaluate the quality of this prediction as there is no available reference in this region to compare with. In the next paragraph, we use one of the six available LES profiles for the comparison of the XBMA prediction and the reference data.

6.4.3.2 Prediction of QoI profiles

Fig. 6.16 illustrates the model probabilities and the tangential velocity at $\frac{x}{l} = 0.76$ on the suction side, the conclusions being similar for other profiles. Fig. 6.16a presents the model probabilities for this profile. In the outer part of the boundary layer, the $k-\omega$ and $k-l$ models are preferred, while the $k-\varepsilon$ and Spalart-Allmaras models are assigned lower probabilities. Nevertheless the model probabilities presented here do not deviate strongly from the value of 0.25. When comparing the general form of the model probabilities with Fig. 6.5a, the model probabilities seem significantly less informed in this case. The tangential velocity profile reconstructed from the model probabilities is presented on Fig. 6.16b. The XBMA prediction is not able to select the border of the accessible area as for Fig. 6.6a but is nonetheless able to select the correct side of the accessible area. The variance associated with the prediction is also consequent for this QoI, which was expected as there is a large diversity in the model predictions and the model probabilities are close to 0.25. The two results cause a clear model

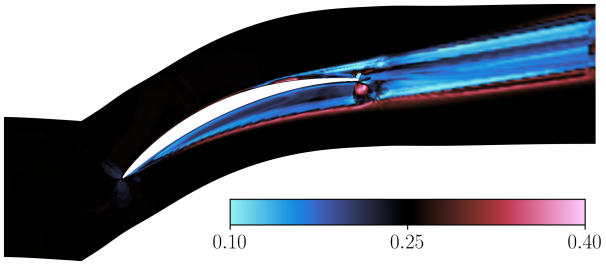

(a) Probability of the $k-\varepsilon$ model.

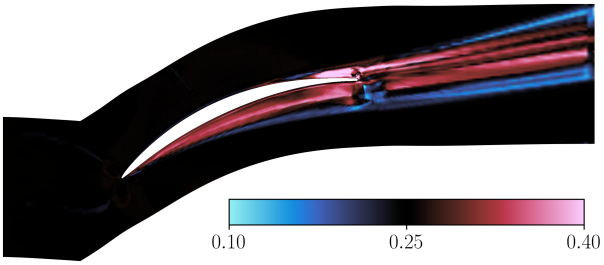

(b) Probability of the Spalart-Allmaras model.

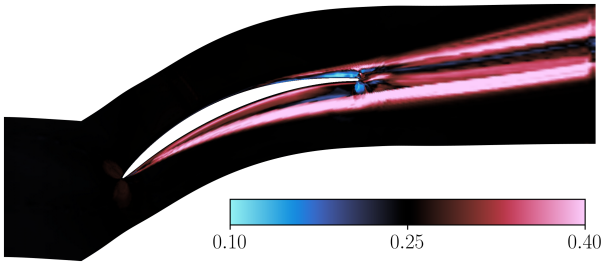

(c) Probability of the $k-l$ model.

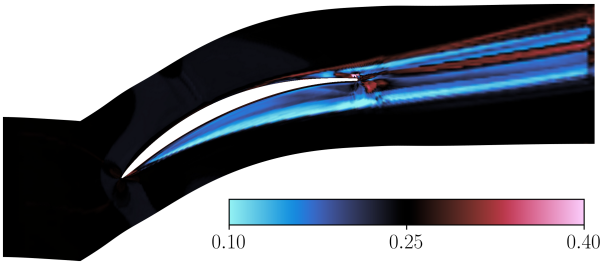

(d) Probability of the $k-\omega$ model.

Figure 6.15: Probability of the four RANS models when only LES data are considered in the training. Training on $\{S_2, S_3, S_4\}$ and prediction on S_1.

uncertainty on the choice of the model, which leads to an inflated variance.

6.4.3.3 Error comparisons on multiple QoIs

Finally, Fig. 6.17 illustrates the MSE averaged on 3 out of the 6 profiles, normalized by the MSE of the $k-\varepsilon$ model. The profiles presented here are two tangential velocities on the suction side at $\frac{x}{l} = 0.56$ and $\frac{x}{l} = 0.76$, and one profile of total pressure loss in the wake at $\frac{x}{l} = 1.10$. The profiles are chosen for their ability to generalize their results to the rest of the profiles. The $k-\varepsilon$ model is the generally associated with the largest MSE, and therefore chosen as the normalization value for each profile. For the first profile, the MSE associated with the $k-\varepsilon$ model is significantly larger than any other RANS models, for which the MSE is around 40% of the $k-\varepsilon$ value. The XBMA significantly improves the MSE on this profile with a reduction of about 50% of the MSE with respect to the best performing RANS models. On the second profile, the XBMA prediction does not fall too far from the 3 best RANS models, but nonetheless scores the fourth best prediction on the MSE criterion. It is also noteworthy that the XBMA is significantly closer to the best model than to the worst one on this profile. Finally the last profile shows the $k-l$ model significantly outperforms every other

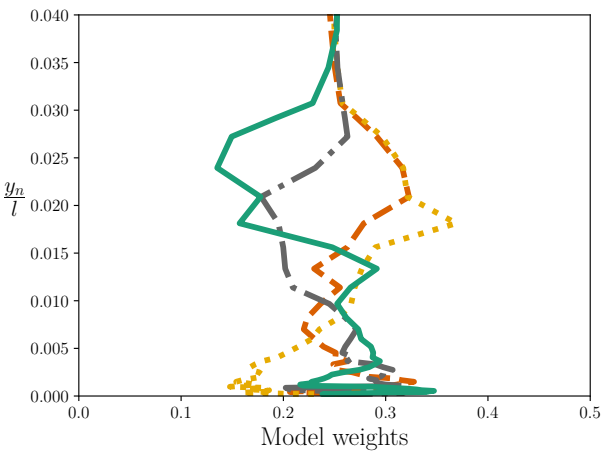

(a) Model probabilities.

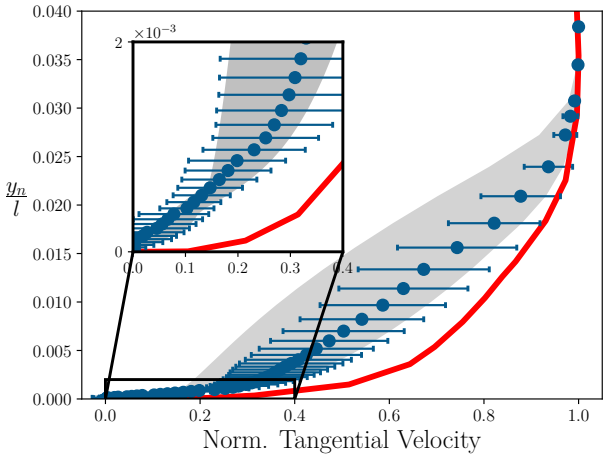

(b) Reconstruction of the QoI.

Figure 6.16: Prediction of the model probabilities and reconstruction of the normalized tangential velocity profile at $\frac{x}{l} = 0.76$ when only LES data are considered in the training. Training on $\{S_2, S_3, S_4\}$ and prediction on S_1.
Model probabilities appears: $k-\varepsilon$ model (—), $k-\omega$ model (- - -), $k-l$ model (-·-·-) and the Spalart-Allmaras (·····). Reference data from [4] appears in (—). Accessible area ▢ , $E[\Delta] \pm \sqrt{Var[\Delta]}$ (-●-).

models, while the $k-\omega$ and the Spalart-Allmaras have high MSE, and $k-\varepsilon$ model still is the worst performing model. In this case, the XBMA provides a prediction in clear improvement with the $k-\omega$, Spalart-Allmaras and $k-\varepsilon$ models, second only to the $k-l$ model.

Using only 6 located profiles in the data set seems to cause the XBMA prediction to lack predictive accuracy. In case of the prediction after training on EARSM reference data, the average MSE presented on Fig. 6.9 and Fig. 6.13 are at least as good as the best RANS model for every QoI predicted. In this case, while the XBMA can sometimes clearly reduce the average MSE, it can also provide predictions with higher error than 3 out of the 4 models considered in the mixing. Even if XBMA is not as well performing than the best RANS model, it is reassuring to note that one never observe the XBMA to be as poorly performing as the worst RANS model.

As previously explained, the case described in this section could be considered as particularly challenging for the XBMA: the very sparse data considered in the training data set leads to a poor description of the feature space, and ultimately inadequately informs model probabilities. Despite these adversarial factors, the XBMA produces reliable predictions, in average improvement with the naive model mixing assigning 0.25 to every model. This result makes us confident on the ability of the

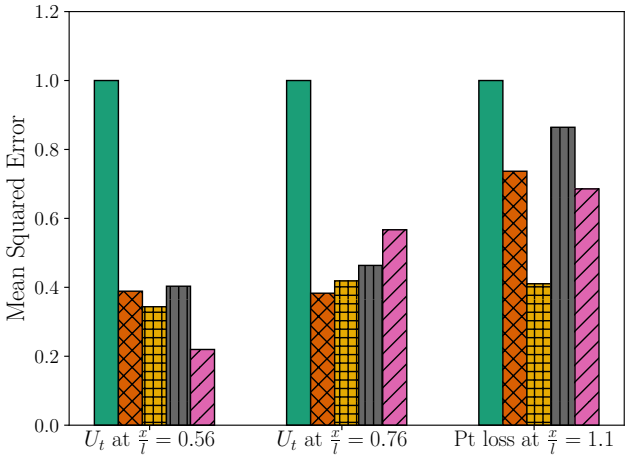

Figure 6.17: Mean-squared error of the four QoIs, normalized by the MSE of the $k-\varepsilon$ model when only LES data are considered in the training. Training on $\{S_2, S_3, S_4\}$ and prediction on S_1.
$k-\varepsilon$ model (■), $k-\omega$ model (▩), $k-l$ model (▦) and Spalart-Allmaras model (▥), XBMA trained on the 6 LES profiles (▨).

XBMA to make accurate predictions even with a relatively low number of data, provided that those data effectively offers extra information on the flow.

6.5 Conclusions

In this chapter, we proposed a novel space-dependent Bayesian Model Averaging (XBMA) algorithm. The XBMA method is based on a supervised regression that learns local model probabilities on a known configuration and evaluates the local model probabilities for an unseen configuration for a set of four RANS models. Complete 2D-fields of multiple QoIs are then reconstructed from the local model probabilities. A set of functions of the mean flow quantities inspired from Ling and Templeton [5] are deployed to serve as inputs of the regression. We chose a Random Forests regressor in reason of the peculiarities of the XBMA problem formulation. The data used in the study are derived from a set of 4 substantially different NACA 65 V103 scenarios, and sourced from an EARSM reference model for the two first test cases and from LES high-fidelity data [7] in the third case. When we used the EARSM model, the influence of the number of elements in the training data set was evaluated by constructing two competing XBMA, one on the complete data set for each scenario and one more realistic of real-life situations using a subset of 820 data per scenario. The method consistently improves overall predictions and provides consistent estimates of the confidence intervals.

The XBMA method has been validated for 3 configurations. We initially used EARSM reference data for the training and the prediction on the same scenario S_2. The influence of the σ parameter on the result was discussed and prediction results were presented. In the second configuration, we used EARSM reference data from three scenarios S_2, S_3 and S_4 to train the XBMA for the prediction on the last unseen scenario S_1. Finally, we used the scarce LES data from S_2, S_3 and S_4 for the prediction on S_1. The results obtained for the first two configurations demonstrate the effectiveness of the XBMA even when few relatively well-distributed data are provided. In addition, the XBMA is able to deliver very accurate predictions when the reference data is contained within the predictions of the models. For the third configuration, XBMA improves RANS predictions on some QoI but not for all quantities. This observation illustrates the crucial role of the features in the regression. When the data used in the training step does not accurately describe the feature space, the XBMA prediction is deteriorated. Nevertheless, the results obtained for EARSM reference cases illustrates that the XBMA does not require a large number of data to be effective, but only that the data be well-distributed in the feature space. An elementary measure of the information learned on the training data can be found by comparing the model probabilities to the reference value of 0.25. Model probabilities significantly differing from this value usually means more informed predictions.

Conclusion and perspectives

In this thesis we investigated some methodologies for the quantification and reduction of parametric and modeling uncertainties in Computational Fluid Dynamics (CFD), with special focus on turbomachinery flows. More specifically, we adopt a Bayesian viewpoint to characterize both the parametric and model-form uncertainties arising from turbulence closures for the Reynolds-Averaged Navier–Stokes equations, widely employed for turbomachinery aerodynamic design. Particular effort is put into the quantification and reduction of model-form uncertainties, i.e. uncertainties related to the imperfect knowledge of the turbulence model more suitable for predicting accurately a given flow.

In the aim of leveraging as much as possible turbulence models already well-established in the industrial use while accounting for the uncertainty in the selection of a single "best" model for all flows of interest, we construct Bayesian Model Averages (BMA) of a set of competing models. Such approach naturally provides an estimate of the uncertainty associated with the prediction.

Two approaches are considered in the study. The first method, initially proposed in [88] extends BMA to encompass the concept of scenarios, to account for the uncertainty in the choice of the flow scenario used to train a model before predicting an unseen flow configuration. The resulting methodology is called Bayesian Model-Scenario Averaging (BMSA). In the present work, we further investigate BMSA in the context of turbomachinery flows. First, we propose a surrogate-model-based calibration procedure to infer model parameters from data available for complex turbomachinery configurations while alleviating computational cost related to recurrent calls to the costly CFD model. Secondly, we investigate various criteria for defining a probability mass function for competing calibration scenarios. We find that 1) the predictions are overall weakly sensitive to the chosen scenario-weighting criterions and 2) a criterion based on model errors for the calibration scenario provides satisfactory results while avoiding to propagate all models for a new scenario, if some model is found to perform poorly already for the calibration scenario.

The second methodology is an original contribution of this thesis, and it consists in building a space-dependent combination of models by leveraging local information on the flow. The proposed algorithm, christened XBMA, combines a set of competing models with fixed parameters (in contrast to BMSA that requires a preliminary –and costly, despite the use of a surrogate model– calibration step) by using a local error measure to evaluate model weights. Afterwards, data are used to train a random forest regressor of such weights in a space of flow features, i.e. a set of flow properties characterizing the behavior of the turbulent flow. Such regressor is finally used to estimate local model weights in the physical space for an unseen configuration and to make predictions with associated uncertainty intervals. XBMA is shown to assign higher weights to models that perform better in a given flow region, preferring consistently the model that delivers the solution closest to the reference data. The result is an improved prediction throughout. XBMA is also shown to provide satisfactory results even with the number of data used for training the model weights is rather small, provided that the data cover a wide variety of flow conditions. If all training data are localised in a given region, XBMA performance is still better than the performance of single models, but the improvements in accuracy are less significant, because only a small portion of the feature space is informed. In region where the competing models offer comparable performance and in regions little covered by data, XMBA assigns equal weights to each model in the mixture.

Although BMSA and especially XBMA represent promising tool for predicting turbulent flows with quantified model-form uncertainty, there are still multiple doors to unlock before their industrial use is possible.

First, the question of the models included in the mixing should be addressed. As any model-mixing method, the accuracy of both BMSA and XBMA strongly depends in the predictive capabilities of the underlying models used to build the mixture. Ideally for XBMA, we would like the ensemble of models to cover a large predictive range, in order for the accessible area to encompass the reference data. In the case of turbomachinery flows, the most widely-used models generally rely on a linear eddy viscosity, i.e. use the same linear constitutive equation for the Reynolds stresses. A possibility to widen the variety of model structures is to include non-linear models such as EARSM or RSM models. Preliminary results for BMSA (Chapter 5) including the EARSM $k - kL$ model alongside LEVM models does not improve over a mixture of purely linear models significanrly. However, is is

expected that EARSM deliver more accurate predictions for 3-D flows, which needs to be investigated in the future. One could also artificially increase the number of models to be combined by considering LEVM models calibrated on specific configurations, as in Chapter 5, instead of baselines. Such models have been demonstrated to deliver accurate predictions of turbomachinery flows in Chapter 5. The downside to a large variety of model is that they will most likely not agree on their predictions, thus maybe unnecessarily inflating the prediction variance. One way to leverage large accessible area while conserving informative variance is simply to better inform the model probabilities, which brings us to the second door to be unlocked.

In the case of XBMA, if effective information of model probabilities is to be attained, it must be through a more efficient regression on the features space. Multiple solution naturally arise from this observation. First, the use of Optimal Sensor Placement (OPS) methods for the data probes location seems to be an interesting path to pursue: it could help us maximize the amount of information drawn from the training flows while avoiding redundancy and inflation of the overall amount of data, which can be prejudicial to the performance of the methods in 3-D cases for example. Alternatively, when OPS methods are not available, such as for data deriving from an experimental campaign or when only preselected LES profiles are available, one could think of one *a posteriori* evaluation of the dispersion of the input features corresponding to the prediction scenario from the space of features described in the training data set. This could lead to a measurement of the trust when put on the regression, *i.e.* a quantification on the uncertainty on the model weights and ultimately a variance on the reconstructed QoI. Such evaluation of the trust in the regression could also be applied on each of the scenarios considered in the training data set separately, thus producing a space-dependent scenario-weighting criterion, bringing BMSA and XBMA even closer together. Additionally, the features space could be extended to suit the specific need of turbomachinery flows. To our knowledge, there is no trace of a proposed feature built from $\nabla\rho$ in the literature. Such feature could be very useful for the turbomachinery context, potentially indicating shocks in compressors or even a thickening of the boundary layer before its detachment. Considering a $\nabla\rho$ based feature would thus allow the features space to encompass a wider range of physics and help us further generalize the method.

Finally, the extension to more complex flows must be examined. The computations presented on this work are proposed for a 2-D NACA 65 V103 compressor cascade configuration. Although complex, such scenarios lacks 3-D effects that are crucial for tip and leakage effects in a real-life compressor.

Next step for the development of XBMA and BMSA methods should include a larger number of scenarios, with different operating conditions and maybe more complex geometries. The extension of XBMA and BMSA methods to 3-D and unsteady flows are certainly worthy being investigated in the future.

Chapter 7

Introduction (français)

7.1 Contexte de la thèse

Dans le secteur de l'aéronautique, aucun compromis n'est accepté en matière de sécurité des vols. Les autorités aéronautiques sont donc chargées d'appliquer les réglementations les plus strictes aux avionneurs et examinent soigneusement chaque pièce volante d'un avion pour garantir sa conformité, peu importe qu'il s'agisse d'un composant physique ou d'un logiciel. Outre la priorité accordée à la sécurité, une sous-estimation des performances attendues d'un composant ou de son risque de défaillance peut nuire gravement à la réputation d'un constructeur aéronautique (OEM) et entraîner des mois de retard et des millions d'euros de pertes en pénalités contractuelles si ces engagements ne sont pas honorés. Afin de garantir ces performances à un coût minimal, les OEM appliquent des méthodes de gestion des risques à leurs produits, de la phase de conception à la livraison. Dans le cas des moteurs d'avions par exemple, des méthodes itératives longues et coûteuses sont utilisées pour concevoir chaque composant, dans l'espoir de dérisquer autant que possible les phases de prototypage et d'essais réels, qui sont souvent considérées comme des moments de vérité pour les produits. C'est le cas notamment pour les composants turbomachines, le cas d'intérêt de cette thèse.

Dans le contexte décrit précédemment, les méthodes de quantification d'incertitudes (QI ou UQ en anglais) ont suscité un intérêt considérable de la part des industriels de l'aéronautique, ceux-ci cherchant à intégrer les méthodes UQ au plus tôt dans leur processus de conception. En addition de la prédiction, la grande force ces méthodes réside en effet dans leurs capacités à fournir des intervalles de confiance crédibles sur cette prédiction. En tant que telles, elles constituent un outil d'aide à la décision très utile pour les décideurs, et leur permettent de réduire les risques très tôt dans la phase

de conception, bien avant les essais en conditions réelles.

Avant de plonger plus avant dans notre sujet, précisons d'abord le sens que nous donnons au mot "incertitudes". Nous suivons ici les définitions données par l'*American Institute of Aeronautics and Astronautics* (AIAA) [8]:

Definition 3 *Incertitude: Une déficience potentielle dans toute phase ou activité du processus de modélisation liée à un manque de connaissances sur le système.*

Les incertitudes sont donc différentes des erreurs, auxquelles on attribue la définition suivante:

Definition 4 *Erreur: Une déficience reconnaissable dans toute phase ou activité de modélisation et de simulation qui n'est pas due à un manque de connaissances sur le système.*

Nous suivons en outre Walters et Huyse [9] en distinguant l'incertitude *aléatoire* (ou *inhérente*) de l'incertitude *épistémique*. Alors que la première découle du caractère aléatoire intrinsèque du système, et ne peut donc pas être réduite, la seconde peut l'être en considérant de meilleurs modèles ou de meilleures données par exemple. Dans leur contribution au numéro spécial de l'AIAA de 1998 consacré aux simulations numériques crédibles d'écoulements ("Credible Computational Fluid Dynamics Simulations"), Oberkampf et Blottner [10] ont identifié quatre sources principales d'incertitude et d'erreur découlant de la simulation numérique d'un problème physique régi par toute équation différentielle partielle (EDP). Ces quatre sources sont décrites ci-dessous:

1. Modélisation physique: cette incertitude est liée aux hypothèses faites sur le problème (comme l'hypothèse d'incompressibilité de l'écoulement dans le cas de la mécanique des fluides numérique par exemple), à la définition des conditions aux limites ou à l'utilisation de modèles physiques auxiliaires, tels que des modèles de réaction chimique ou de turbulence par exemple.

2. Erreurs de discrétisation et de résolution: elles sont liées aux erreurs numériques sur la géométrie du problème, à la convergence en temps et en espace de la résolution, aux erreurs associées à l'inversion de grandes matrices issues de la discrétisation des équations gouvernantes et aux erreurs de troncature associées au schéma numérique utilisé.

3. Erreurs d'arrondis numériques: ces erreurs correspondent à la précision finie de la machine de calculs.

4. Erreurs de programmation et utilisateurs.

Les deux derniers types d'erreurs sont généralement considérés négligeables lorsqu'une arithmétique de haute précision est utilisée pour les calculs. On suppose aussi que le code informatique et la configuration numérique ont été soigneusement préparés et débogués.

Dans la suite du manuscrit, nous nous concentrons sur les outils de conception des compresseurs de moteurs d'avion, et plus particulièrement sur les solveurs de dynamique des fluides numériques (DFN ou CFD en anglais). La CFD est devenue la pierre angulaire de l'analyse des écoulements, tant dans les études universitaires que dans les applications d'ingénierie, principalement en raison de sa capacité à fournir des informations fiables sur l'écoulement lorsque ces informations ne sont pas facilement accessibles par des campagnes expérimentales ou des raisonnements théoriques. Malgré cela, l'application des approches UQ au domaine de la CFD reste relativement récente, contrairement aux domaines de la mécanique des structures ou des méthodes de navigation et de guidage par exemple, qui ont depuis longtemps employé ces méthodes [9]. Cela peut s'expliquer à la fois par l'émergence tardive de la CFD en tant que discipline, mais surtout par le coût de calcul beaucoup plus élevé des simulations CFD par rapport aux simulations de mécanique des solides par exemple. L'augmentation constante de la rapidité et de la puissance des systèmes informatiques rend désormais possible l'application des méthodes UQ dans la conception CFD de configurations complexes. Dans le contexte de cette thèse, nous nous concentrerons exclusivement sur la première source d'incertitude en CFD, *i.e.* l'incertitude liée à la modélisation physique, car la deuxième source d'erreur (liée au processus de discrétisation) est considérée hors du cadre de cette étude.

7.2 Incertitudes en Mécanique des Fluides Numérique et modélisation RANS

Les équations de Navier-Stokes (NS) régissent la dynamique des écoulements à toutes les échelles mais conduisent, en raison de leur nature non linéaire, à des solutions complexes et chaotiques pour des écoulements caractérisés par des valeurs élevées du nombre de Reynolds (Re), ce qui est le cas pour les configurations d'intérêt industriel. Ceci est particulièrement vrai pour les écoulements en turbomachines qui nous intéressent ici. Ceux-ci sont en effet principalement turbulents, bien que la transition puisse également jouer un rôle important dans la physique de l'écoulement. Les simulations

numériques directes (SND ou DNS en anglais) pourraient être utilisées, en théorie, pour résoudre toutes les échelles de la turbulence, mais les calculs sont excessivement coûteux, puisque le nombre requis de points de maillage augmente avec $\mathbf{Re}^{9/4}$ [11]. Ce comportement limite l'application de la DNS à des configurations académiques simples pour des nombres de Reynolds faibles à modérés, alors qu'elle reste hors de portée pour les nombres de Reynolds élevés typiquement rencontrés dans les problèmes d'ingénierie. Une alternative intéressante consiste à ne résoudre que les échelles les plus grandes et les plus énergétiques de la turbulence, tout en modélisant les plus petites. Une telle approche, connue sous le nom de simulation aux grandes échelles (SGE ou LES en anglais), permet de réduire considérablement les coûts de calcul par rapport à la DNS pour les simulations à nombres de Reynolds modérés, puisque le nombre de points de maillage nécessaire est maintenant de l'ordre de $\mathbf{Re}^{0.4}$ pour les écoulements à cisaillement. Malheureusement, la LES reste excessivement coûteuse pour les écoulements d'intérêt à nombre de Reynolds élevé, en raison des petites échelles énergétiques qui dominent la dynamique dans les régions proches des parois [12]. Par conséquent, la seule stratégie abordable pour une utilisation routinière dans les bureaux d'études reste l'approche Navier-Stokes moyennée par Reynolds (RANS), qui modélise la gamme complète des échelles d'écoulement turbulent. Bien qu'elle présente de nombreuses lacunes - en particulier pour les écoulements sévèrement hors-équilibre et éventuellement transitoires comme ceux qui nous intéressent dans ce travail -, son coût de calcul nettement inférieur fait de la modélisation RANS le fer de lance de la conception des turbomachines.

Les incertitudes de la modélisation RANS peuvent être classées en quatre niveaux [13]: (1) incertitudes liées à la validité du processus de moyennage lui-même ; (2) incertitudes dans la représentation du tenseur de Reynolds en fonction du champ moyen ; (3) incertitudes dans la représentation mathématique des lois utilisées pour relier le tenseur de Reynolds au champ moyen et des équations de transport auxiliaires pour les propriétés de la turbulence (par exemple pour l'énergie cinétique turbulente ou la dissipation) ; (4) incertitudes dans la valeur des paramètres intervenants dans la fermeture, à une représentation mathématique donnée.

Les incertitudes décrites au point (3) sont souvent appelées incertitudes "structurelles" ou "de forme de modèle", tandis que celles du point (4) sont appelées incertitudes paramétriques [14]. Dans ce manuscrit, on s'efforce de fournir un cadre probabiliste bayésien pour les prédictions d'écoulements turbulents basées sur les hypothèses RANS, à la fois pour les incertitudes paramétriques (4) et les

incertitudes de forme de modèle (3). C'est pourquoi nous nous concentrons principalement sur ce type d'approches dans la suite de ce chapitre. Le lecteur est invité à consulter [14] pour une revue plus complète des incertitudes de modèle dans la modélisation RANS.

7.3 Incertitudes paramétriques

Un cadre naturel pour la quantification d'incertitudes paramétriques est celui de l'inférence bayésienne. Dans celle-ci, les coefficients du modèle se voient attribuer des distributions de probabilité a priori (basées par exemple sur des données de la littérature ou des avis d'experts) qui sont ensuite mises à jour par l'observation de données, ce qui conduit à l'estimation d'une distribution de probabilité jointe dite *a posteriori*. Avec des coefficients de modèle représentés par des variables aléatoires suivant une certaine distribution de probabilité, la sortie du modèle est également une quantité aléatoire caractérisée par une distribution de probabilité. Dans ce cadre, la prédiction du modèle est naturellement dotés d'intervalles d'incertitude. Plus de détails sur la quantification bayésienne d'incertitude sont donnés au chapitre 3 de ce manuscrit.

Outre la possibilité de déterminer des intervalles de confiance, l'inférence bayésienne apparaît comme particulièrement adaptée au problème posé, et ceci pour trois raisons principales. Premièrement, les coefficients des modèles RANS ont été initialement calibrés pour des écoulements canoniques simples (la décroissance de la turbulence homogène et isotrope, les couches limites sur plaques planes ou les écoulements de cisaillement simples par exemple), qui restent assez éloignés des configurations d'écoulement en turbomachine. Deuxièmement, les méthodes bayésiennes sont bien adaptées aux méthodes d'assimilation de données tout en tenant compte des erreurs d'observation sur les données utilisées dans la calibration. Si ces dernières sont relativement limitées en nombre et bruitées, elle pourront ensuite être successivement mises à jour dès que de nouvelles ou de meilleures données seront disponibles [15]. Enfin, l'inférence bayésienne fournit des informations sur la sensibilité du modèle aux coefficients de fermeture et sur l'universalité (ou non) de ces derniers.

En raison de leur coût considérable, l'application des méthodes de calibration bayésienne aux modèles RANS est plutôt récente. La première tentative d'une telle entreprise se trouve dans le travail de Cheung *et al.* [16], dans lequel les coefficients du modèle de turbulence de Spalart-Allmaras ont été

calibrés pour les modèles d'écoulement sur plaques planes. Oliver et Moser [17], ont étendu ce travail en considérant trois modèles RANS supplémentaires, à savoir les modèles de Baldwin-Lomax, de $k-\varepsilon$ Chien et le v^2-f. Edeling *et al.* [3] ont ensuite calibré cinq modèles RANS sur 14 écoulements turbulents de plaque plane soumis à divers gradients de pression externe. Margheri *et al.* [18] ont étudié l'incertitude paramétrique associée à deux modèles largement utilisés, *i.e.* le $k-\varepsilon$ Launder-Sharma et le $k-\omega$ Menter SST, en utilisant des contraintes physiques et des données collectées dans la littérature pour construire des distributions de probabilité pour les paramètres des modèles. Papadimitriou et Papadimitriou [19] ont utilisé des méthodes adjointes pour calibrer efficacement le modèle Spalart-Allmaras sur une plaque plane, tandis que Guillas *et al.* [20] ont recalibré le modèle $k-\varepsilon$ sur un écoulement urbain. De même, Shaefer *et al.* [21] ont étudié les incertitudes paramétriques du modèle de Spalart-Allmaras sur les écoulements transsoniques limités par des parois et souligné les larges intervalles épistémiques sur ces valeurs.

7.4 Incertitudes de forme de modèle

La pratique habituelle en CFD, qui consiste à sélectionner un seul modèle de turbulence parmi tous les modèles disponibles et à supposer que ce dernier est le meilleur modèle possible, tend à sous-estimer l'incertitude réelle sur la prédiction de ce modèle. Ce problème a d'abord été décrit par des statisticiens, en l'occurrence Draper [22], qui a une fois de plus adopté une approche bayésienne pour tenir compte de l'incertitude sur la forme du modèle. En suivant [14], nous classons les approches actuelles de quantification d'incertitudes de forme de modèle RANS en deux catégories: l'une non paramétrique et l'autre paramétrique, selon l'endroit où les incertitudes sont introduites. En général, il n'est pas possible de traiter un ensemble infini et continu de modèles alternatifs, et l'incertitude du modèle est estimée en considérant un ensemble de modèles RANS concurrents.

Premièrement, les approches non paramétriques introduisent des incertitudes directement dans la formulation mathématique des modèles. Dans le contexte CFD, cela peut signifier modifier la viscosité turbulente, les termes sources dans les équations de transport des quantités turbulentes ou même le tenseur de Reynolds elle-même. Cette option est la plus puissante, car elle permet de tenir compte des incertitudes sur les hypothèses mathématiques fondant les modèles, mais elle est souvent intrusive et plus coûteuse en termes de calcul. Au contraire, l'approche paramétrique introduit des incertitudes par le biais de la représentation stochastique du modèle, c'est-à-dire qu'il est maintenant vu comme

une réalisation d'une distribution (continue ou discrète) de modèles alternatifs. Pour cette raison, l'approche paramétrique de l'incertitude de la forme de modèle est souvent adaptée à un cadre dédié à la quantification de l'incertitude paramétrique (4), car les deux sont très proches. Par rapport à l'approche non paramétrique, l'approche paramétrique présente l'avantage considérable d'être non-intrusive (aucune modification du solveur CFD n'est requise), à condition que les coefficients du modèle RANS puissent être prescrits comme variables d'entrée du calcul. Cependant, l'incertitude n'est estimée qu'à travers les paramètres incertains et les structures alternatives de l'ensemble du modèle, et aucune autre forme de modèle ne peut être capturée.

7.4.1 Approches non paramétriques

Les approches non paramétriques visent à évaluer directement l'erreur associée à la structure du modèle, c'est-à-dire à la forme mathématique du modèle. Par exemple, les modèles de turbulence les plus utilisés reposent sur l'analogie de Boussinesq (voir chapitre 2), c'est-à-dire sur l'hypothèque que le tenseur de Reynolds s'écrit linéairement en fonction des gradients de vitesse, ce qui les empêche de prédire les écoulements secondaires dans un conduit carré, quels que soient les coefficients du modèle. Le but des approches paramétriques est ainsi d'estimer l'erreur induite par cette approximation par rapport à une solution de référence fournie, par exemple, par un champ DNS ou LES (appelé champ haute-fidélité). A l'inverse les approches non-paramétriques ne se contentent pas de quantifier cette erreur, mais proposent de la réduire.

Un premier exemple d'une telle approche se trouve dans le travail de Dow et Wang [23], qui ont inféré un champ de viscosité turbulente à partir d'un champ complet de vitesse dans un canal plan obtenu via DNS. Un métamodèle par processus gaussien (aussi connu sous le nom de Krigeage) a ensuite été construit, dans le but de prédire une correction du champ de ν_t obtenu par modèle RANS. Singh et Duraisamy [24] ont proposé de corriger l'équation de transport du modèle Spalart-Allmaras en appliquant une fonction multiplicative $\beta(x)$ au terme de production. Cette méthode s'est avérée plus efficace pour prédire les données DNS sur un ensemble d'écoulements de canaux, d'interactions choc-couche limite et d'écoulements avec courbure et séparation que le modèle Spalart-Allmaras non modifié.

Enfin, la dernière famille d'approches non-paramétriques vise à directement estimer une correction du tenseur de Reynolds. La première tentative dans cette direction a été formulée par Oliver et Moser

[25], qui ont introduit un tenseur de discorde δ_T associé au tenseur de Reynolds pour tenir compte de l'incertitude quant à la forme du modèle et l'ont ensuite propagé à travers les équations gouvernantes. Une telle approche s'est avérée fructueuse dans des écoulements en canal plan à différents nombres de Reynolds. Le cadre proposé par Oliver et Moser a ensuite été repris dans de nombreux travaux visant à quantifier et réduire les incertitudes liées à la forme du modèle RANS. La piste la plus utilisée consiste cependant à appliquer des perturbations directement au tenseur de Reynolds. Emory, Iaccarino et al. [26, 27, 28] se sont d'abord appuyés sur des travaux antérieurs portants sur la réalisabilité du tenseur de Reynolds [29, 30, 31], et plus particulièrement sur la nécessité pour le tenseur d'être symétrique défini semi-positif, et ont proposé de perturber le tenseur de Reynolds en tenant compte des contraintes physiques, au moyen de sa décomposition sur le triangle barycentrique [32] ou le triangle de Lumley [29].

Xiao et al. [33] ont étendu cette méthode en proposant un cadre statistique dans lequel le tenseur de Reynolds est modélisé comme un champ aléatoire centré sur le tenseur de Reynolds RANS. Des perturbations correctement paramétrées et réalisables sont ensuite appliquées au tenseur, afin d'explorer l'espace incertain. Bien que cette méthode ait produit des résultats intéressants, elle ne permet de perturber que la magnitude et la forme du tenseur, mais pas son orientation. Dans leur papier suivant, Xiao et al. [34] ont fait évolué cette méthode en modélisant le tenseur de Reynolds par une matrice aléatoire 3×3 centrée sur la contrainte RANS, et en injectant les perturbations directement sous la forme d'une matrice aléatoire. Cette méthode présente le grand avantage de perturber à la fois l'amplitude, la forme et l'orientation du tenseur de Reynolds, même s'il est plus difficile d'intégrer ainsi les connaissances physiques disponibles sur un écoulement spécifique. Les deux approches ont ensuite été comparées [35], avec des résultats similaires.

Ling et al. [36] ont également choisi de déduire les corrections du tenseur de Reynolds en décomposant la contrainte sur une base d'invariants du vecteur gradient de vitesse, pour ensuite reconstruire les coefficients de la décomposition par une régression via réseau de neurones. De même, Weatheritt et Sandberg [37] ont utilisé des algorithmes génétiques pour prédire les coefficients de la même décomposition. Une telle approche finit par converger vers des modèles EARSM, une classe de modèles RANS utilisant des relations constitutives non linéaires pour le tenseur de Reynolds. D'autre part, Wang et al. [38] ont développé une stratégie plus systématique pour prédire les corrections de la magnitude, de l'anisotropie et de l'orientation du tenseur de Reynolds, en considérant une base étendue d'invariants

basés sur le gradient de vitesse, le gradient de pression et le gradient d'énergie cinétique turbulente. Wu et al. [39] ont complété ce travail en apprenant séparément les parties linéaire et non linéaire de la contrainte de Reynolds, la partie linéaire étant traitée implicitement pour améliorer le conditionnement du modèle. Enfin, Schmelzer et al. [40] ont proposé une méthode de régression parcimonieuse pour la prédiction du terme d'anisotropie du tenseur de Reynolds directement à partir de données haute-fidélité. Un modèle $k-\omega$ SST augmenté via cette méthode est ensuite construit et fourni des prédictions plus précises que le modèle de base pour un ensemble d'écoulements séparés. Ben Hassan Saïdi et al. [41] ont généralisé cette méthode à des configurations pour lesquelles les champs complets de statistiques turbulentes de premier et second ordre ne sont pas disponibles, comme les bases de données expérimentales par exemple.

Les approches non paramétriques sont indéniablement prometteuses et ont, à juste titre, suscité un intérêt considérable de la part de la communauté CFD en raison de leur potentiel d'apprentissage automatisé de modèles RANS à partir de données. Cependant, elles souffrent des limitations suivantes : (1) elles ont tendance à manquer de capacité de généralisation, c'est-à-dire qu'elles fonctionnent bien pour des écoulements similaires à ceux de la base d'apprentissage mais peuvent difficilement être extrapolées à des écoulements différents ; (2) elles nécessitent une quantité importante de données haute-fidélité (généralement coûteuses à obtenir et limitées à des configurations simples à faible nombre de Reynolds) et ne sont pas bien adaptés aux données incomplètes et bruitées telles que les données expérimentales; (3) elles conduisent, dans la plupart des cas, à des prédictions déterministes et ne fournissent pas d'estimations des intervalles de confiance en raison des incertitudes persistants à la fois dans la forme du modèle et dans les coefficients de fermeture. Pour la conception de turbomachines industrielles (et pour la conception technique en général), les intervalles de confiance sur les quantités d'intérêt (QoI) prédites représentent une information aussi précieuse que la QoI elle-même, puisqu'ils permettent d'estimer les incertitudes sur la performance attendue du système dès le début de la phase de conception. C'est pourquoi, dans ce travail, nous nous concentrons plutôt sur les approches de quantification d'incertitude paramétriques, telles que décrites dans le paragraphe suivant.

7.4.2 Approches paramétriques par mélange de modèles

Bien que les approches paramétriques infèrent uniquement les distributions a posteriori des coefficients du modèle, elles peuvent également être utilisées pour estimer, dans une certaine mesure, les incertitudes du modèle. Tout d'abord, on peut étendre le cadre stochastique construit pour l'incertitude paramétrique afin d'englober l'incertitude du modèle, en fournissant une représentation stochastique de cette incertitude, comme dans le travail précurseur de Kennedy et O'Hagan [42]. Cela nécessite la formulation d'un terme stochastique d'erreur de modèle à ajouter à la sortie du modèle, dont les hyperparamètres sont ensuite calibrés en même temps que les coefficients du modèle physique. Par exemple, Cheung et al. [16] ont non seulement recalibré les coefficients du modèle Spalart-Allmaras, mais ont également formulé trois représentations stochastiques de l'erreur de modèle en fonction de la quantité utilisée pour les calibrations (la vitesse d'écoulement moyenne), et ont calibré les hyperparamètres correspondants. Oliver et Moser [17] ont étudié différentes représentations de ce terme d'erreur de modèle et les ont comparés à l'aide de données DNS pour des écoulements en canal plan. Malheureusement, le terme d'erreur ainsi estimé ne peut pas être directement réutilisé pour une configuration géométrique ou un QoI différent de ceux utilisés dans l'étape de calibration.

Dans le contexte de la conception des turbomachines, les ingénieurs choisissent généralement un seul modèle RANS en se basant sur un compromis entre la précision, le coût de calcul et le jugement d'un expert. Cette pratique ignore alors l'incertitude du modèle, ce qui peut conduire à des prédictions artificiellement trop confiantes. A l'inverse, il est possible de reconnaître l'existence de plusieurs modèles concurrents, qui fournissent chacun des solutions différentes mais également plausibles au même problème, par la même constituant une source d'incertitude sur le choix du modèle. Une façon de rendre compte de cela, consiste à adopter un point de vue multi-modèles.

Il existe plusieurs méthodes d'ensemble multi-modèles. Toutes ces méthodes reposent sur l'idée que la combinaison des modèles augmente généralement la précision, la fiabilité et la cohérence des prévisions des modèles. Ces méthodes ont été utilisées pour une large variété d'applications. On peut citer entre autres le secteur de la santé publique (par exemple, la malaria dans Thomson et al. [43]), de l'agriculture (par exemple, le rendement des cultures dans Cantelaube et Terres [44]), et des sciences du climat (par exemple, Palmer et al. [45]). Dans le contexte de la modélisation RANS, Poroseva et al. [46] ont exploré le potentiel de la théorie de la preuve de Dempster-Shafer [47] pour quantifier

l'incertitude des modèles $k-\varepsilon$ and $k-\omega$. Dans tous les cas, l'information combinée de plusieurs modèles s'avère supérieure à celle obtenue par un modèle unique.

Dans le cadre bayésien, la méthode multi-modèle la plus naturelle est le Bayesian Model Averaging (BMA), initialement proposé par Box et Tiao [48] et revisité plus tard par Draper [22], qui a largement contribué à la popularité de la méthode. La BMA fournit un formalisme cohérent et systématique pour prendre en compte l'incertitude du modèle, et peut être décrite [22] comme "la solution bayésienne au problème de l'incapacité à évaluer et à propager l'erreur de modèle". Dans la BMA, les prédictions de plusieurs modèles sont combinées en utilisant les probabilités a posteriori du modèle comme poids, ce qui fournit une mesure de l'erreur de modèle. L'évaluation des probabilités a posteriori du modèle était historiquement difficile à calculer, ce qui a entravé le développement de la méthode dans les communauté scientifiques hors de celle des statistiques bayésiennes. Dans une tentative de surmonter cette limite, Mosleh et Apostolakis [49] ont proposé la méthode des facteurs d'ajustement, qui étend la portée de l'inférence bayésienne à de telles applications en remplaçant les calculs des probabilités du modèle par des opinions d'experts. Cette approche a ensuite été étendue par Zio et Apostolakis [50] pour tenir compte différentes structures de modèles. Cependant ces méthodes n'eurent que peu de succès.

Dans la seconde moitié des années 1990, les progrès des capacités de calcul ont considérablement réduit la charge de calcul associée à la BMA, ce qui a provoqué une renaissance de la méthode, sous l'impulsion de Draper, Madigan et Raftery [22, 51]. Hoeting et al. [52] ont formulé un tutoriel complet pour la BMA en mettant l'accent sur la mise en oeuvre et les questions pratiques. Leur travail essentiel a conduit à l'adoption de la BMA dans un large éventail de domaines en dehors de sa communauté d'origine: dans leur étude systématique, Fragoso et al. [53] ont recensé 820 articles sur la BMA publiés dans plus de 300 revues ou conférences entre 1997 et 2016. Les thèmes abordés vont de l'économétrie, où elle est utilisée pour prévoir de futurs taux d'échanges [54], à l'oncologie, où elle est utilisée pour estimer le nombre de cas de cancer [55].

Dans le domaine de l'ingénierie, la BMA a été principalement utilisée en hydrologie et en météorologie suite aux travaux de Raftery et al. [56], dans lesquels la BMA a été étendue aux systèmes dynamiques, et plus particulièrement aux prévisions météorologiques. Les résultats ont montré une capacité de prédiction améliorée, avec des prédictions beaucoup mieux calibrées et des intervalles de confiance plus resserrés. Suite à ces travaux, la BMA a été utilisée à de nombreuses reprises en

météorologie et en hydrologie [57, 58, 59, 60, 61, 62, 63, 64], avec des résultats convaincants.

En plus de leurs bonnes performances, des propriétés mathématiques solides soutiennent l'utilisation de la BMA. Dans leur travail, Madigan et Raftery [51] ont prouvé que l'utilisation de la BMA donne lieu à une meilleure prédiction (évaluée par une règle de notation logarithmique) que tout modèle unique considéré. Dans le cas d'intérêt de cette étude, où l'on sait que la "vérité" est hors de la portée des modèles RANS considérés, la BMA sélectionnera asymptotiquement le modèle unique de l'ensemble qui est le plus proche de la vérité en termes de divergence de Kullback-Leibler [65].

Cependant, d'autres méthodes de combinaison de modèles peuvent être mieux adaptées à un objectif différent. Tout comme la BMA, le stacking [66] est une combinaison linéaire et convexe de modèles, ce qui signifie que les poids des modèles sont dans $[0, 1]$ et que leur somme est égale à un. Contrairement à la BMA, le stacking utilise des méthodes d'optimisation pour évaluer les poids des modèles qui minimisent une fonction de coût, (souvent l'erreur quadratique moyenne (EQM) leave-one-out (LOO)), sous la contrainte de leur convexité. Par définition, le stacking surpasse typiquement la BMA lorsque le critère considéré est la MSE [67] car la BMA n'est pas optimisée pour cette tâche et illustre plutôt l'ajustement aux données [68]. Néanmoins, le stacking reste moins utilisé que la BMA car le stacking classique ne fournit que des estimations ponctuelles, et non la distribution postérieure entière [65].

Une extension importante de la méthode BMA est représentée par le Bayesian Model and Scenario Averaging (BMSA), qui introduit le concept de scénario dans le formalisme BMA. Cette idée était initialement présente dans les travaux de Draper [22] mais a été formellement décrit pour la première fois par Meyer et al. [57]. Dans ce cas, un scénario est défini comme "une déclaration générale sur des avenirs possibles" et illustré par l'exemple suivant : un scénario de changement climatique est une déclaration générale décrivant un changement réaliste du climat. Comme la BMA, la BMSA combine les prédictions de plusieurs modèles, fournissant ainsi une mesure de l'incertitude du modèle, en utilisant les distributions a posteriori des coefficients déduits séparément de différents scénarios de calibration. Bien que la BMSA ait été employée avec succès dans le contexte hydrologique [57, 61], Rojas et al. ayant remarqué que l'utilisation de scénarios conduisait à des estimations plus réalistes et plus fiables de l'incertitude de prediction, la méthode reposait à l'époque entièrement sur le jugement d'experts pour l'évaluation des probabilités des scénarios. Edeling et al. [3] ont proposé une nouvelle formulation de la BMSA, plus facile à mettre en oeuvre, dans laquelle les probabilités de

scénario sont évaluées à partir d'un critère objectif, indépendant de tout jugement d'expert et basé sur l'accord entre les modèles. Dans le même travail, les scénarios sont définis comme des "exemples d'une classe d'écoulements pour lesquels nous souhaitons faire des prédictions fiables", mais toujours définis à partir de leurs variables explicatives, à savoir la géométrie ou les conditions aux limites par exemple. Cette formulation fait des scénarios un concept très bien adapté à la CFD. Une telle BMSA a ensuite été construite en moyennant cinq modèles RANS calibrés sur 14 scénarios, correspondant à des écoulements turbulents de plaque plane soumis à divers gradients de pression externes. La méthode BMSA, calibrée sur les scénarios issus de [3], a ensuite été appliqué avec succès à une configuration d'aile transsonique dans [69]. Merle et al. [70] ont proposé un critère alternatif pour les probabilités de scénario, qui prend en compte la qualité de la calibration pour chaque scénario concurrent. Ces résultats prometteurs ont été produits sur des cas académiques simples, mais leur capacité à prédire des écoulements plus complexes tels que ceux des turbomachines reste à voir. De plus, les différents critères de probabilités des scénarios n'ont pas encore été comparés et on peut se demander lequel choisir.

D'autre part, il existe un large consensus dans la communauté de la modélisation RANS selon lequel il n'existe pas de meilleur modèle RANS universel, mais qu'il existe des modèles connus pour être plus performants dans certaines situations et moins performants dans d'autres. Ces performances disparates peuvent même se produire au sein d'un même écoulement, où un modèle RANS peut être mieux adapté à la prédiction d'une région de l'écoulement et moins bien dans une autre. Récemment, dans le domaine des statistiques appliquées, Yu et al. [71] ont proposé un nouvel algorithme, baptisé Clustered Bayesian Averaging (CBA), qui vise à combiner des modèles concurrents en utilisant des poids de modèle variant dans l'espace. Cela contraste avec le BMA et le BMSA, qui appliquent des poids constants tout au long de l'écoulement, exception faite du calcul de l'aile de [69] où des poids de scénario différents ont été appliqués à différents positions sur l'aile. La méthode CBA a depuis été appliquée avec succès aux modèles météorologiques [72, 73], mais aucune extension aux problèmes CFD n'a été envisagée à ce jour.

7.5 Objectifs

Dans le présent travail, nous étudions en profondeur l'approche de mélange de modèle bayésienne dans le but de fournir des prédictions robustes des écoulements turbulents de turbomachines, sous un ensemble de modèles RANS incertains. Plus précisément, les objectifs de la thèse sont les suivants :

1. Dans un premier temps, nous développons une stratégie de calibration pour les simulations coûteuses d'écoulements en turbomachines, et nous étudions pour la première fois le potentiel d'une BMSA pour de telles configurations en nous concentrant sur une cascade de compresseurs.

2. Deuxièmement, nous étudions différentes stratégies de pondération des scénarios pour la BMSA, dans le but de réduire les coûts de calcul tout en améliorant la précision des résultats.

3. Enfin, nous explorons l'idée d'une combinaison de modèles variant dans l'espace en proposant un algorithme inspiré de la CBA de Yu et al. [71] et bien adapté aux applications CFD.

La thèse est structurée comme suit. Dans le chapitre 2, nous rappelons les équations RANS et les modèles RANS utilisés dans ce travail. Dans le chapitre 3, nous présentons le cadre bayésien, en mettant l'accent sur son application aux calculs CFD. Dans le chapitre 4, nous décrivons les cas de test de calibration et de validation et les données utilisées pour l'inférence. Le chapitre 5 est consacré aux deux premiers objectifs de cette thèse: tout d'abord, la méthodologie BMSA est évaluée pour une cascade de compresseurs. Ensuite, le choix des critères de probabilité des scénarios est étudié pour le même cas. Enfin, le chapitre 6 aborde le troisième objectif de l'étude : l'algorithme proposé est décrit en détail et évalué de manière approfondie pour le cas du flux de compresseurs. Les conclusions et les perspectives découlant de ce travail sont proposées dans le dernier chapitre.

Conclusion et perspectives (français)

Dans cette thèse, nous évaluons certaines méthodologies pour la quantification et la réduction des incertitudes paramétriques et de modèle dans le cadre de la dynamique des fluides numérique (CFD), avec un accent placé sur les écoulements en turbomachines. Plus précisément, nous adoptons ici un point de vue bayésien pour caractériser les incertitudes paramétriques et de modèle découlant des fermetures des modèles de turbulence pour les équations RANS largement utilisées pour la conception aérodynamique des turbomachines. Un effort particulier est placé sur les incertitudes de forme de modèle, c'est-à-dire les incertitudes liées à la connaissance imparfaite du modèle de turbulence le plus approprié pour prédire avec précision un écoulement donné.

Afin de tirer parti autant que possible des modèles de turbulence déjà bien établis dans l'industrie tout en tenant compte de l'incertitude dans la sélection d'un seul "meilleur" modèle pour tous les écoulements d'intérêt, nous construisons ici une prédiction bayésienne moyennée (BMA) à partir d'un ensemble de modèles concurrents. Cette approche fournit naturellement une estimation de l'incertitude associée à la prédiction.

Deux approches sont considérées dans cette étude. La première méthode, initialement proposée dans [88], étend la BMA au concept de scénarios. La prédiction tient ainsi compte de l'incertitude dans le choix du scénario d'écoulement utilisé pour entraîner un modèle, avant de prédire un second scénario d'écoulement non vue. Cette méthode est appelée Bayesian Model-Scenario Averaging (BMSA). Dans le présent travail, nous étudions plus en détail la BMSA dans le contexte des écoulements en turbomachines. Premièrement, nous proposons une procédure de calibration basée sur un méta-modèle afin d'inférer les paramètres du modèle à partir des données disponibles sur des configurations turbomachines complexes. Cette méthode permet aussi de réduire les coûts de calcul liés aux appels récurrents au modèle CFD coûteux. Ensuite, nous étudions différents critères pour définir une fonction de masse probabiliste associée aux scénarios de calibration en concurrence. Nous constatons

d'abord que les prédictions sont globalement peu sensibles au choix de critère de pondération des scénarios et ensuite qu'un critère basé sur les erreurs de modèle pour le scénario de calibration fournit des résultats satisfaisants tout en évitant de propager tous les modèles pour un nouveau scénario, si un modèle s'avère déjà peu performant pour le scénario de calibration.

La seconde méthodologie représente une contribution originale de cette thèse, et elle consiste à construire une combinaison de modèles dépendant de l'espace en exploitant les informations locales sur l'écoulement. L'algorithme proposé, baptisé XBMA, combine un ensemble de modèles concurrents avec des paramètres fixés (contrairement à la BMSA qui nécessite une étape de calibration préliminaire et coûteuse, malgré l'utilisation d'un modèle de substitution) et évalue les poids des modèles à partir d'une mesure de leur erreur locale. Les données disponibles sont ensuite utilisées pour entraîner une régression par forêt aléatoire de ces poids dans un espace de features de l'écoulement, c'est-à-dire un ensemble de propriétés de l'écoulement caractérisant son comportement turbulent. Cette régression est finalement utilisée pour estimer localement les poids de modèle pour une configuration non vue et ainsi prédire les quantités d'intérêts de l'écoulement en moyenne et les intervalles de confiance associés. Il est démontré que la XBMA attribue des poids plus élevés aux modèles les plus performants dans une région de l'écoulement donnée, en préférant systématiquement le modèle qui fournit la solution la plus proche des données de référence. Le résultat est une prédiction améliorée pour toutes les quantités d'intérêt considérées. Il est également démontré que XBMA fournit des résultats satisfaisants même si le nombre de données utilisées lors de l'entraînement des poids du modèle est plutôt faible, à condition que les données couvrent une grande zone de l'espace des conditions d'écoulement. Si toutes les données d'entraînement sont localisées dans une région de l'écoulement donnée, les performances de XBMA restent meilleures que celles des modèles RANS pris individuellement, mais le gain de précision sur la prédiction est moins important car seule une petite partie de l'espace des features est décrite. Dans les régions où les modèles concurrents offrent des performances comparables et dans les régions peu couvertes par les données, la XMBA attribue un poids égal à chaque modèle du mélange.

Bien que la BMSA et plus encore la XBMA soient des outils qui tiennent compte de l'incertitude sur la forme du modèle et prometteurs pour la prédiction des écoulements turbulents, il reste encore de nombreuses étapes à franchir avant que leur utilisation industrielle ne soit possible.

Tout d'abord, il convient d'aborder la question des modèles inclus dans le mélange. Comme toute

méthode de mélange de modèles, la précision de la BMSA et de la XBMA dépend fortement de la capacité prédictive des modèles sous-jacents utilisés dans le mélange. Idéalement pour la XBMA, nous aimerions que l'ensemble des modèles couvre une large gamme prédictive, afin que la zone accessible englobe les données de référence. Dans le cas des écoulements en turbomachines, les modèles les plus utilisés reposent généralement sur une viscosité tourbillonnaire linéaire, c'est-à-dire qu'ils utilisent la même équation constitutive linéaire pour les contraintes de Reynolds. Une piste intéressante consiste à élargir la variété des représentations mathématiques utilisées dans les modèles et d'inclure des modèles non linéaires tels que les modèles EARSM ou RSM. Les résultats préliminaires pour la BMSA (chapitre 5) incluant le modèle EARSM $k - kL$ aux modèles linéaire ne semblent pas indiquer d'amélioration significative de la prédiction par rapport à la prédiction basée sur un ensemble de modèles purement linéaires. Cependant, on s'attend à ce que les modèles EARSM fournissent des prédictions plus précises pour les écoulements tridimensionnels, une piste de recherche pour l'avenir. On pourrait aussi augmenter artificiellement le nombre de modèles à combiner en considérant des modèles linéaires calibrés sur des configurations spécifiques, comme dans le chapitre 5, au lieu des modèles de base. Il a été démontré que de tels modèles fournissent des prédictions précises des écoulements en turbomachines dans ce même chapitre. L'inconvénient d'une grande variété de modèles reste qu'ils peuvent demeurer en désaccord sur leurs prédictions, ce qui pourrait gonfler inutilement la variance de la prédiction. Une façon d'exploiter la grande surface accessible à la prédiction tout en conservant une variance informative est simplement de mieux informer les probabilités du modèle, ce qui nous amène à la deuxième étape qu'il reste à franchir.

Dans le cas de la XBMA, si l'on veut obtenir des informations utiles sur les probabilités de modèle, il faut passer par une régression plus efficace sur l'espace des features. De multiples réflexions découlent naturellement de cette observation. Tout d'abord, l'utilisation de méthodes de placement optimal des capteurs (OPS) pour le choix de l'emplacement des sondes semble être une voie intéressante à poursuivre : elle pourrait nous aider à maximiser la quantité d'informations tirées des écoulements d'apprentissage tout en évitant la redondance et l'inflation de la quantité globale de données, ce qui peut être préjudiciable à la performance des méthodes, dans les cas tridimensionnels par exemple. Alternativement, lorsque les méthodes OPS ne sont pas disponibles comme pour les données issues d'une campagne expérimentale ou lorsque seuls des profils LES présélectionnés sont disponibles, on peut penser à une évaluation a posteriori de la dispersion des features correspondant au scénario de

prédiction par rapport à l'espace des features décrites dans l'ensemble des scénarios d'entraînement. Cela pourrait conduire à une mesure de la confiance accordée à la régression, c'est-à-dire à une quantification de l'incertitude sur les poids du modèle et, en fin de compte, à une variance sur le QoI reconstruit. Cette évaluation de la confiance dans la régression pourrait également être appliquée à chacun des scénarios considérés dans l'ensemble de données d'entraînement séparément, produisant ainsi un critère de pondération des scénarios dépendant de l'espace, rapprochant toujours plus BMSA et XBMA. En outre, l'espace des features pourrait s'étendre pour répondre aux besoins spécifiques des écoulements en turbomachines. A notre connaissance, il n'y a pas de trace d'une proposition de feature construite à partir de $\nabla\rho$ dans la littérature. Une telle feature pourrait être très utile pour le contexte des turbomachines, indiquant potentiellement la présence de chocs dans les compresseurs ou même un épaississement de la couche limite avant son détachement. Envisager une feature basée sur $\nabla\rho$ permettrait donc à l'espace des caractéristiques d'englober un plus large éventail de physique et nous aiderait à généraliser davantage la méthode.

Enfin, l'extension de ces méthodes à des écoulements plus complexes est un défi intéressant à poursuivre. Les calculs présentés dans ce travail sont proposés pour une configuration 2-D de cascade de compresseurs NACA 65 V103. Bien que complexes, de tels scénarios ne disposent pas d'effets 3-D qui sont cruciaux pour la prédiction d'un compresseur réel. La prochaine étape du développement des méthodes XBMA et BMSA est donc celle de l'inclusion d'un plus grand nombre de scénarios, correspondants à des points de fonctionnement différents et à des géométries plus complexes. L'extension des méthodes XBMA et BMSA aux écoulements tridimensionnels et instationnaires mérite aussi certainement d'être étudiée dans la suite de ce travail.

Bibliography

[1] D. C. Wilcox, "Comparison of two-equation turbulence models for boundary layers with pressure gradient," *AIAA journal*, vol. 31, no. 8, pp. 1414–1421, 1993.

[2] S. Kline, D. Coles, and E. Hirst, *Computation of Turbulent Boundary Layers–1968 AFOSR-IFP-Stanford Conference: Proceedings*. Thermosciences Division, Stanford University, 1969.

[3] W. Edeling, P. Cinnella, and R. Dwight, "Predictive RANS simulations via Bayesian model-scenario averaging," *Journal of Computational Physics*, vol. 275, pp. 65–91, 2014.

[4] J. Leggett, "Detailed investigation of loss prediction of an axial compressor cascade at off-design conditions in the presence of incident free-stream disturbances using large eddy simulations," Ph.D. dissertation, University of Southampton, April 2018. [Online]. Available: https://eprints.soton.ac.uk/422285/

[5] J. Ling and J. Templeton, "Evaluation of machine learning algorithms for prediction of regions of high Reynolds averaged Navier Stokes uncertainty," *Physics of Fluids*, vol. 27, no. 8, p. 085103, 2015.

[6] L. Hilgenfeld, P. Cardamone, and L. Fottner, "Boundary layer investigations on a highly loaded transonic compressor cascade with shock/laminar boundary layer interactions," *Proceedings of the Institution of Mechanical Engineers, Part A: Journal of Power and Energy*, vol. 217, no. 4, pp. 349–356, 2003.

[7] J. Leggett *et al.*, "Detailed investigation of rans and les predictions of loss generation in an axial compressor cascade at off design incidences," in *ASME Turbo Expo 2016: Turbomachinery Technical Conference and Exposition*. American Society of Mechanical Engineers Digital Collection, 2016.

[8] C. F. D. Committee, *Guide for the Verification and Validation of Computational Fluid Dynamics Simulations (AIAA G-077-1998 (2002))*. American Institute of Aeronautics and Astronautics, Inc., 1998.

[9] R. W. Walters and L. Huyse, "Uncertainty analysis for fluid mechanics with applications," 2002.

[10] W. L. Oberkampf and F. G. Blottner, "Issues in computational fluid dynamics code verification and validation," *AIAA journal*, vol. 36, no. 5, pp. 687–695, 1998.

[11] S. B. Pope and S. B. Pope, *Turbulent flows*. Cambridge university press, 2000.

[12] P. R. Spalart, "Detached-eddy simulation," *Annual review of fluid mechanics*, vol. 41, pp. 181–202, 2009.

[13] K. Duraisamy, G. Iaccarino, and H. Xiao, "Turbulence modeling in the age of data," *Annual Review of Fluid Mechanics*, vol. 51, 2019, doi: 10.1146/annurev-fluid-010518-040547.

[14] X. Heng and P. Cinnella, "Quantification of model uncertainty in RANS simulations: A review," *Progress in Aerospace Sciences*, vol. 108, pp. 1–31, 2019.

[15] A. Gelman *et al.*, *Bayesian Data Analysis. 3rd edition*. Chapman and Hall/CRC., 2013.

[16] S. Cheung *et al.*, "Bayesian uncertainty analysis with applications to turbulence modeling," *Reliability Engineering & System Safety - RELIAB ENG SYST SAFETY*, vol. 96, pp. 1137–1149, 09 2011.

[17] T. A. Oliver and R. D. Moser, "Bayesian uncertainty quantification applied to RANS turbulence models," in *Journal of Physics: Conference Series*, vol. 318, no. 4. IOP Publishing, 2011, p. 042032.

[18] L. Margheri *et al.*, "Epistemic uncertainties in RANS model free coefficients," *Computers & Fluids*, vol. 102, pp. 315–335, 2014.

[19] D. I. Papadimitriou and C. Papadimitriou, "Bayesian uncertainty quantification of turbulence models based on high-order adjoint," *Computers & Fluids*, vol. 120, pp. 82–97, 2015.

[20] S. Guillas, N. Glover, and L. Malki-Epshtein, "Bayesian calibration of the constants of the k–ε turbulence model for a CFD model of street canyon flow," *Computer methods in applied mechanics and engineering*, vol. 279, pp. 536–553, 2014.

[21] J. A. Schaefer *et al.*, "Uncertainty quantification and sensitivity analysis of SA turbulence model coefficients in two and three dimensions," in *55th AIAA Aerospace Sciences Meeting*, 2017, p. 1710.

[22] D. Draper, "Assessment and propagation of model uncertainty," *Journal of the Royal Statistical Society: Series B (Methodological)*, vol. 57, no. 1, pp. 45–70, 1995.

[23] E. Dow and Q. Wang, "Quantification of structural uncertainties in the k-w turbulence model," in *52nd AIAA/ASME/ASCE/AHS/ASC Structures, structural dynamics and materials conference 19th AIAA/ASME/AHS adaptive structures conference 13t*, 2011.

[24] A. P. Singh and K. Duraisamy, "Using field inversion to quantify functional errors in turbulence closures," *Physics of Fluids*, 2016.

[25] T. Oliver and R. Moser, "Uncertainty quantification for RANS turbulence model predictions," in *APS division of fluid dynamics meeting abstracts*, vol. 62, 2009, pp. LC–004.

[26] M. Emory, R. Pecnik, and G. Iaccarino, "Modeling structural uncertainties in Reynolds-averaged computations of shock/boundary layer interactions," in *49th AIAA Aerospace sciences meeting including the new horizons forum and aerospace exposition*, 2011, p. 479.

[27] M. Emory, J. Larsson, and G. Iaccarino, "Modeling of structural uncertainties in Reynolds-averaged Navier-Stokes closures," *Physics of Fluids*, vol. 25, no. 11, p. 110822, 2013.

[28] C. Gorle, M. Emory, and G. Iaccarino, "RANS modeling of turbulent mixing for a jet in supersonic cross flow: model evaluation and uncertainty quantification," in *THMT-12. Proceedings of the Seventh International Symposium On Turbulence Heat and Mass Transfer*, 2012.

[29] J. L. Lumley, "Computational modeling of turbulent flows," in *Advances in applied mechanics*. Elsevier, 1979, vol. 18, pp. 123–176.

[30] U. Schumann, "Realizability of Reynolds-stress turbulence models," *The Physics of Fluids*, vol. 20, no. 5, pp. 721–725, 1977.

[31] S. B. Pope, "Pdf methods for turbulent reactive flows," *Progress in energy and combustion science*, vol. 11, no. 2, pp. 119–192, 1985.

[32] S. Banerjee *et al.*, "Presentation of anisotropy properties of turbulence, invariants versus eigenvalue approaches," *Journal of Turbulence*, no. 8, p. N32, 2007.

[33] H. Xiao *et al.*, "Quantifying and reducing model-form uncertainties in Reynolds-averaged Navier–Stokes simulations: A data-driven, physics-informed Bayesian approach," *Journal of Computational Physics*, vol. 324, pp. 115–136, 2016.

[34] H. Xiao, J.-X. Wang, and R. G. Ghanem, "A random matrix approach for quantifying model-form uncertainties in turbulence modeling," *Computer Methods in Applied Mechanics and Engineering*, vol. 313, pp. 941–965, 2017.

[35] J.-X. Wang, R. Sun, and H. Xiao, "Quantification of uncertainties in turbulence modeling: A comparison of physics-based and random matrix theoretic approaches," *International Journal of Heat and Fluid Flow*, vol. 62, pp. 577–592, 2016.

[36] J. Ling, A. Kurzawski, and J. Templeton, "Reynolds averaged turbulence modelling using deep neural networks with embedded invariance," *Journal of Fluid Mechanics*, vol. 807, pp. 155–166, 2016.

[37] J. Weatheritt and R. Sandberg, "A novel evolutionary algorithm applied to algebraic modifications of the RANS stress–strain relationship," *Journal of Computational Physics*, vol. 325, pp. 22–37, 2016.

[38] J.-X. Wang, J.-L. Wu, and H. Xiao, "Physics-informed machine learning approach for reconstructing Reynolds stress modeling discrepancies based on DNS data," *Physical Review Fluids*, vol. 2, no. 3, p. 034603, 2017.

[39] J.-L. Wu, H. Xiao, and E. Paterson, "Physics-informed machine learning approach for augmenting turbulence models: A comprehensive framework," *Physical Review Fluids*, vol. 3, no. 7, p. 074602, 2018.

[40] M. Schmelzer, R. P. Dwight, and P. Cinnella, "Discovery of algebraic Reynolds-stress models using sparse symbolic regression," *Flow, Turbulence and Combustion*, vol. 104, no. 2, pp. 579–603, 2020.

[41] I. Saïdi *et al.*, "CFD-driven symbolic identification of algebraic Reynolds-stress models," *arXiv preprint arXiv:2104.09187*, 2021.

[42] M. C. Kennedy and A. O'Hagan, "Bayesian calibration of computer models," *Journal of the Royal Statistical Society: Series B (Statistical Methodology)*, vol. 63, no. 3, pp. 425–464, 2001.

[43] M. C. Thomson *et al.*, "Malaria early warnings based on seasonal climate forecasts from multi-model ensembles," *Nature*, vol. 439, no. 7076, pp. 576–579, 2006.

[44] P. Cantelaube and J.-M. Terres, "Seasonal weather forecasts for crop yield modelling in Europe," *Tellus A: Dynamic Meteorology and Oceanography*, vol. 57, no. 3, pp. 476–487, 2005.

[45] T. Palmer *et al.*, "Probabilistic prediction of climate using multi-model ensembles: from basics to applications," *Philosophical Transactions of the Royal Society B: Biological Sciences*, vol. 360, no. 1463, pp. 1991–1998, 2005.

[46] S. V. Poroseva, M. Y. Hussaini, and S. L. Woodruff, "Improving the predictive capability of turbulence models using evidence theory," *AIAA Journal*, vol. 44, no. 6, pp. 1220–1228, 2006.

[47] G. Shafer, *A mathematical theory of evidence*. Princeton university press, 1976.

[48] G. E. Box and G. C. Tiao, "A further look at robustness via Bayes's theorem," *Biometrika*, vol. 49, no. 3/4, pp. 419–432, 1962.

[49] A. Mosleh and G. Apostolakis, "The assessment of probability distributions from expert opinions with an application to seismic fragility curves," *Risk analysis*, vol. 6, no. 4, pp. 447–461, 1986.

[50] E. Zio and G. Apostolakis, "Two methods for the structured assessment of model uncertainty by experts in performance assessments of radioactive waste repositories," *Reliability Engineering & System Safety*, vol. 54, no. 2-3, pp. 225–241, 1996.

[51] D. Madigan and A. E. Raftery, "Model selection and accounting for model uncertainty in graphical models using Occam's window," *Journal of the American Statistical Association*, 1994.

[52] J. A. Hoeting *et al.*, "Bayesian model averaging: a tutorial," *Statistical science*, vol. 14, no. 4, pp. 382–401, 1999.

[53] T. M. Fragoso, W. Bertoli, and F. Louzada, "Bayesian model averaging: A systematic review and conceptual classification," *International Statistical Review*, vol. 86, no. 1, pp. 1–28, 2018.

[54] J. H. Wright, "Bayesian Model Averaging and exchange rate forecasts," *Journal of Econometrics*, vol. 146, 2008.

[55] L. Bailly *et al.*, "Bayesian estimation of a cancer population by capture-recapture with individual capture heterogeneity and small sample," *BMC medical research methodology*, vol. 15, no. 1, pp. 1–11, 2015.

[56] A. E. Raftery *et al.*, "Using Bayesian model averaging to calibrate forecast ensembles," *Monthly weather review*, vol. 133, no. 5, pp. 1155–1174, 2005.

[57] P. Meyer *et al.*, "Combined estimation of hydrogeologic conceptual model, parameter, and scenario uncertainty with application to uranium transport at the Hanford Site 300 Area," Pacific Northwest National Lab.(PNNL), Richland, WA (United States), Tech. Rep., 2007.

[58] Q. Duan *et al.*, "Multi-model ensemble hydrologic prediction using Bayesian model averaging," *Advances in Water Resources*, vol. 30, no. 5, pp. 1371–1386, 2007.

[59] C. Tebaldi and R. Knutti, "The use of the multi-model ensemble in probabilistic climate projections," *Philosophical Transactions of the Royal Society of London A: Mathematical, Physical and Engineering Sciences*, vol. 365, no. 1857, pp. 2053–2075, 2007.

[60] T. Diomede *et al.*, "Discharge prediction based on multi-model precipitation forecasts," *Meteorology and Atmospheric Physics*, vol. 101, no. 3-4, pp. 245–265, 2008.

[61] R. R. *et al.*, "Application of a multimodel approach to account for conceptual model and scenario uncertainties in groundwater modelling," *Journal of Hydrology*, vol. 394, no. 3-4, pp. 416–435, 2010.

[62] T. Wöhling *et al.*, "Bayesian model averaging to explore the worth of data for soil-plant model selection and prediction," *Water Resources Research*, vol. 51, no. 4, pp. 2825–2846, 2015.

[63] N. Chitsazan and F. T.-C. Tsai, "A hierarchical Bayesian model averaging framework for groundwater prediction under uncertainty," *Groundwater*, vol. 53, no. 2, pp. 305–316, 2015.

[64] S. Baran and A. Möller, "Joint probabilistic forecasting of wind speed and temperature using Bayesian model averaging," *Environmetrics*, vol. 26, no. 2, pp. 120–132, 2015.

[65] Y. Yao *et al.*, "Using stacking to average Bayesian predictive distributions (with discussion)," *Bayesian Analysis*, vol. 13, no. 3, pp. 917–1007, 2018.

[66] L. Breiman, "Stacked regressions," *Machine learning*, vol. 24, no. 1, pp. 49–64, 1996.

[67] B. Clarke, "Comparing Bayes model averaging and stacking when model approximation error cannot be ignored," *Journal of Machine Learning Research*, vol. 4, no. Oct, pp. 683–712, 2003.

[68] H. Wong and B. Clarke, "Improvement over Bayes prediction in small samples in the presence of model uncertainty," *Canadian Journal of Statistics*, vol. 32, no. 3, pp. 269–283, 2004.

[69] W. Edeling *et al.*, "Bayesian predictions of Reynolds-averaged Navier–Stokes uncertainties using maximum a posteriori estimates," *AIAA Journal*, vol. 56, no. 5, pp. 2018–2029, 2018.

[70] X. Merle and P. Cinnella, "Robust prediction of dense gas flows under uncertain thermodynamic models," *Reliability Engineering & System Safety*, vol. 183, pp. 400–421, 2019.

[71] Q. Yu, S. N. MacEachern, and M. Peruggia, "Clustered Bayesian model averaging," *Bayesian Analysis*, vol. 8, no. 4, pp. 883–908, 2013.

[72] I. Abdallah, K. Tatsis, and E. Chatzi, "Unsupervised local cluster-weighted bootstrap aggregating the output from multiple stochastic simulators," *Reliability Engineering & System Safety*, vol. 199, p. 106876, 2020.

[73] K. U. Rahman *et al.*, "Hydrological evaluation of merged satellite precipitation datasets for streamflow simulation using SWAT: A case study of Potohar Plateau, Pakistan," *Journal of Hydrology*, vol. 587, p. 125040, 2020.

[74] D. C. Wilcox, *Turbulence modeling for CFD*. DCW Industries , La Canada, CA, 2006.

[75] B. E. Launder and B. Sharma, "Application of the energy-dissipation model of turbulence to the calculation of flow near a spinning disc," *Letters in heat and mass transfer*, vol. 1, no. 2, pp. 131–137, 1974.

[76] B. Smith, "A near wall model for the k-l two equation turbulence model," in *Fluid Dynamics Conference*, 1994, p. 2386.

[77] P. R. Spalart and S. R. Allmaras, "One-equation turbulence model for aerodynamic flows," *Recherche aerospatiale*, no. 1, pp. 5–21, 1994.

[78] B. Smith, "The k-kL turbulence model and wall layer model for compressible flows," in *AIAA Paper 90-1483*, 1990.

[79] H. Bézard and T. Daris, "Calibrating the length scale equation with an explicit algebraic Reynolds stress constitutive relation," in *Engineering turbulence modelling and experiments 6*. Elsevier, 2005, pp. 77–86.

[80] S. Wallin and A. Johansson, "An explicit algebraic Reynolds stress model for incompressible and compressible turbulent flows," *Journal of Fluid Mechanics*, vol. 403, p. 89–132, 2000.

[81] L. Cambier, S. Heib, and S. Plot, "The ONERA elsA CFD software: input from research and feedback from industry," *Mechanics & Industry*, vol. 14, no. 3, pp. 159–174, 2013. [Online]. Available: https://doi.org/10.1051/meca/2013056

[82] B. Aupoix *et al.*, "Transition and turbulence modeling," *Aerospace Lab*, no. 2, pp. p–1, 2011.

[83] S. Deck, "Zonal-detached-eddy simulation of the flow around a high-lift configuration," *AIAA journal*, vol. 43, no. 11, pp. 2372–2384, 2005.

[84] S. Deck, "Recent improvements in the zonal detached eddy simulation (ZDES) formulation," *Theoretical and Computational Fluid Dynamics*, vol. 26, no. 6, pp. 523–550, 2012.

[85] C. Benoit, S. Péron, and S. Landier, "Cassiopee: a CFD pre-and post-processing tool," *Aerospace Science and Technology*, vol. 45, pp. 272–283, 2015.

[86] J. Brynjarsdóttir and A. O'Hagan, "Learning about physical parameters: The importance of model discrepancy," *Inverse problems*, vol. 30, no. 11, p. 114007, 2014.

[87] M. Arnst, R. Ghanem, and C. Soize, "Identification of Bayesian posteriors for coefficients of chaos expansions," *Journal of Computational Physics*, vol. 229, no. 9, pp. 3134–3154, 2010.

[88] W. Edeling *et al.*, "Bayesian estimates of parameter variability in the k–ε turbulence model," *Journal of Computational Physics*, vol. 258, pp. 73–94, 2014.

[89] N. Metropolis *et al.*, "Equation of state calculations by fast computing machines," *The Journal of Chemical Physics*, vol. 21, no. 6, pp. 1087–1092, Jun. 1953. [Online]. Available: http://aip.scitation.org/doi/10.1063/1.1699114

[90] W. K. Hastings, "Monte Carlo sampling methods using Markov chains and their applications," *Biometrika*, vol. 57, no. 1, pp. 97–109, 1970.

[91] J. Geweke *et al.*, *Evaluating the accuracy of sampling-based approaches to the calculation of posterior moments*. Federal Reserve Bank of Minneapolis, Research Department Minneapolis, MN, 1991, vol. 196.

[92] C. K. Williams and C. E. Rasmussen, *Gaussian processes for machine learning*. MIT press Cambridge, MA, 2006.

[93] F. Pedregosa *et al.*, "Scikit-learn: Machine learning in python," *Journal of Machine Learning Research*, vol. 12, pp. 2825–2830, 2011.

[94] C. Zhu *et al.*, "Algorithm 778: L-bfgs-b: Fortran subroutines for large-scale bound-constrained optimization," *ACM Transactions on Mathematical Software (TOMS)*, vol. 23, no. 4, pp. 550–560, 1997.

[95] E. Jones *et al.*, "Scipy: Open source scientific tools for python," 2001–. [Online]. Available: http://www.scipy.org/

[96] V. R. Joseph, E. Gul, and S. Ba, "Maximum projection designs for computer experiments," *Biometrika*, vol. 102, no. 2, pp. 371–380, 2015.

[97] M. Hoege, A. Guthke, and W. Nowak, "The hydrologist's guide to Bayesian model selection, averaging and combination," *Journal of Hydrology*, vol. 572, pp. 96–107, 2019.

[98] M. de Zordo-Banliat *et al.*, "Bayesian model-scenario averaged predictions of compressor cascade flows under uncertain turbulence models," *Computers & Fluids*, vol. 201, p. 104473, 2020.

[99] D. Xiu and G. E. Karniadakis, "The Wiener-Askey polynomial chaos for stochastic differential equations," *SIAM J. Sci. Comput.*, vol. 24, no. 2, pp. 619–644, 2002, iSBN: 1064827510957197.

[100] L. Sun *et al.*, "Surrogate modeling for fluid flows based on physics-constrained deep learning without simulation data," *Computer Methods in Applied Mechanics and Engineering*, vol. 361, p. 112732, 2020.

[101] K. O. Lye, S. Mishra, and D. Ray, "Deep learning observables in computational fluid dynamics," *Journal of Computational Physics*, vol. 410, p. 109339, 2020.

[102] S. Kline, B. Cantwell, and G. Lilley, *1980-81 AFOSR-HTTM-Stanford Conference on Complex Turbulent Flows.* Thermosciences Division, Stanford University, 1981.

[103] R. Leipold, M. Boese, and L. Fottner, "The influence of technical surface roughness caused by precision forging on the flow around a highly loaded compressor cascade," *Journal of turbomachinery*, vol. 122, no. 3, pp. 416–424, 2000.

[104] J. Iseler, L. Hilgenfeld, and M. Pfitzner, "Investigations of the boundary layer on a highly loaded compressor cascade with wake-induced transition," in *Turbo Expo: Power for Land, Sea, and Air*, 2006.

[105] T. A. Zaki, J. Wissink, and P. A. Rodi, W.and Durbin, "Direct numerical simulations of transition in a compressor cascade: the influence of free-stream turbulence," *Journal of Fluid Mechanics*, vol. 665, pp. 57–98, 2010.

[106] *Investigations of Shock/Boundary-Layer Interaction in a Highly Loaded Compressor Cascade*, ser. ASME Turbo Expo: Power for Land, Sea, and Air, vol. Volume 1: Turbomachinery, 06 1995.

[107] M. de Zordo-Banliat *et al.*, "Estimates of turbulence modeling uncertainties in NACA65 cascade flow predictions by Bayesian Model-Scenario Averaging," *International Journal of Numerical Methods for Heat and Fluid Flow - Accepted for publication*, 2022.

[108] D. I. Papadimitriou and C. Papadimitriou, "Optimal sensor placement for the estimation of turbulence model parameters in CFD," *International Journal for Uncertainty Quantification*, vol. 5, no. 6, 2015.

[109] V. Mons, J. Chassaing, and P. Sagaut, "Optimal sensor placement for variational data assimilation of unsteady flows past a rotationally oscillating cylinder," *Journal of Fluid Mechanics*, vol. 823, pp. 230–277, 2017.

[110] F. Menter, "Zonal two equation kw turbulence models for aerodynamic flows," in *23rd fluid dynamics, plasmadynamics, and lasers conference*, 1993, p. 2906.

[111] L. Breiman *et al.*, "Classification and regression trees," 1984.

[112] S. Russell and P. Norvig, *Artificial Intelligence: a Modern Approach, fourth edition*, 2020.

[113] C. M. Bishop, *Pattern Recognition and Machine Learning*. Springer, 2006.

[114] C. Cortes and V. Vapnik, "Support-vector networks," *Machine learning*, 1995.

[115] L. Breiman, "Bagging predictors," *Machine learning*, 1996.

[116] G. E. Hinton, S. Osindero, and Y.-W. Teh, "A Fast Learning Algorithm for Deep Belief Nets," *Neural Computation*, vol. 18, no. 7, pp. 1527–1554, 2006.

[117] J. Ling, R. Jones, and J. Templeton, "Machine learning strategies for systems with invariance properties," *Journal of Computational Physics*, vol. 318, pp. 22–35, 2016.

[118] R. W. Johnson, *Handbook of fluid dynamics*. CRC Press, 2016.

List of publications

Journal papers

- M. de Zordo-Banliat, X. Merle, G. Dergham, P. Cinnella, *Bayesian model-scenario averaged predictions of compressor cascade flows under uncertain turbulence models*, Computers & Fluids, Volume 201, 2020 - **Published**
- M. de Zordo-Banliat, X. Merle, G. Dergham, P. Cinnella, *Estimates of turbulence modeling uncertainties in NACA*65 *cascade flow predictions by Bayesian Model-Scenario Averaging*, International Journal of Numerical Methods for Heat and Fluid Flow - **Accepted for publication**
- M. de Zordo-Banliat, G. Dergham, X. Merle, P. Cinnella, *Space-dependent multi-model combination: application to the prediction of a compressor cascade*, Journal of Computational Physics - **To be submitted**

Conferences

- *Estimates of turbulence modeling uncertainties in NACA*65 *cascade flows predictions with Bayesian Model-Scenario Averaging*, 55th 3AF International Conference on Applied Aerodynamics, April 12 – 14 2021, Poitiers, France.
- *Space-dependent Bayesian model averaging of turbulence models for compressor cascade flows*, Seminar for Machine Learning and UQ in scientific computing, CWI, February 25 2021, Amsterdam, Netherlands.
- *Space-dependent model combination of RANS turbulence models*, 4th International Conference on Uncertainty Quantification in Computational Sciences and Engineering, June 28 – 30 2021, Athens, Greece.

Appendix A

MAP estimates and posterior model probabilities

We report in the following tables A.1 to A.5 the MAP estimates of the closure coefficients for each of the five models, namely the Spalart–Allmaras, Wilcox' $k-\omega$, Smith's $k-l$, Launder–Sharma $k-\varepsilon$ and the EARSM $k-kL$ turbulence models, for the four compressor cascade scenarios considered in this study. In Table A.6 we report the posterior model probabilities $P(M_i|D_k, S_k)$ for each scenario of chapter 5.

Closure Coeff.	Nominal	S_1	S_2	S_3	S_4
κ	0.41	0.54	0.50	0.46	0.50
C_{w2}	0.3	0.59	0.88	0.89	0.27
C_{w3}	2.0	1.41	2.14	1.02	2.38
C_{v1}	7.1	17.7	17.9	14.2	8.44
C_{b1}	0.1355	0.14	0.14	0.07	0.08
C_{b2}	0.622	0.85	1.48	0.51	0.88
σ	2/3	0.82	0.64	1.46	0.60

Table A.1: Nominal values and MAP estimates of scenarios S_1, S_2, S_3, S_4 for the closure coefficients of the Spalart–Allmaras model.

Closure Coeff.	Nominal	S_1	S_2	S_3	S_4
κ	0.41	0.44	0.50	0.51	0.39
σ_{do}	0.125	0.060	0.138	0.145	0.198
σ^*	0.6	0.68	0.93	0.92	0.41
σ	0.5	0.50	0.27	0.23	0.42
β^*	0.09	0.09	0.15	0.15	0.08
β	0.0708	0.065	0.021	0.020	0.099

Table A.2: Nominal values and MAP estimates of scenarios S_1, S_2, S_3, S_4 for the closure coefficients of the $k-\omega$ model.

Closure Coeff.	Nominal	S_1	S_2	S_3	S_4
$C_{\epsilon 2}$	1.92	2.66	2.01	1.99	1.90
C_μ	0.09	0.11	0.15	0.10	0.08
σ_k	1.00	0.86	0.80	0.82	0.55
κ	0.41	0.57	0.79	0.77	0.35

Table A.3: Nominal values and MAP estimates of scenarios S_1, S_2, S_3, S_4 for the closure coefficients of the $k-\epsilon$ model.

Closure Coeff.	Nominal	S_1	S_2	S_3	S_4
σ_l	1.43	3.56	3.55	3.08	2.13
κ	0.41	0.38	0.36	0.36	0.45
B_1	18.0	1.2	35.1	35.7	35.8
σ_k	1.43	0.20	0.20	0.20	0.63
E_2	1.20	0.01	0.01	0.07	1.38

Table A.4: Nominal values and MAP estimates of scenarios S_1, S_2, S_3, S_4 for the closure coefficients of the $k-l$ model.

Closure Coeff.	Nominal	S_1	S_2	S_3	S_4
C_1'	0.00	0.05	0.29	0.28	0.08
C_1	1.80	2.19	2.13	2.19	2.19
C_2	0.80	0.68	0.83	0.84	0.84
C_3	2.00	1.60	1.62	2.19	2.08
C_4	1.11	1.35	1.33	1.30	1.08
κ	0.41	0.50	0.32	0.43	0.30
$c_{\Phi 1}$	1.00	1.08	1.08	1.04	0.95
$c_{\Phi 2}$	0.58	0.55	0.36	0.31	0.57
C_μ	0.09	0.06	0.11	0.13	0.11
$C_{\Phi k}$	1.53	1.14	1.18	0.84	0.77
$C_{\Phi\Phi}$	-1.38	-1.20	-0.82	-1.19	-1.42
σ_k	0.90	1.00	2.40	2.38	1.09
σ_Φ	1.60	1.12	1.36	1.25	0.75
$c_{\Phi\omega}$	0.0008	0.0010	0.0010	0.0010	0.0010
$c_{\omega 1}$	0.08	0.050	0.047	0.056	0.060

Table A.5: Nominal values and MAP estimates of scenarios S_1, S_2, S_3, S_4 for the closure coefficients of the EARSM $k-kL$ model.

$P(M_i\|\overline{D_k}, S_k)$	S_1	S_2	S_3	S_4
Spalart–Allmaras	$< 10^{-3}$	0.500	0.394	0.378
$k-\omega$	$< 10^{-3}$	0.160	0.170	0.240
$k-\epsilon$	$< 10^{-3}$	0.012	0.144	0.006
$k-l$	$< 10^{-3}$	0.295	0.227	0.249
EARSM $k-kL$	0.996	0.033	0.065	0.127

Table A.6: Posterior model probabilities $P(M_i|\overline{D_k}, S_k)$ under the MAP hypothesis for scenarios S_1, S_2, S_3, S_4.

Maximilien de ZORDO-BANLIAT

Quantification and reduction of turbulence modeling uncertainties in turbomachinery flows using Bayesian multi-model ensembles

Résumé : Les exigences des autorités de certification ainsi que la recherche constante de performances elevées poussent les industriels aéronautiques à maitriser toujours plus finement les incertitudes propres à leurs produits. Pour cette raison, les méthodes de Quantification d'Incertitudes (UQ) sont désormais intégrés dès que possible dans le processus de conception d'une pièce, afin de garantir sa fiabilité ainsi que sa performance. Dans cette thèse, nous nous concentrons sur la simulation numérique d'écoulements dans des turbomachines et nous présentons deux approches pour la quantification et la réduction des incertitudes épistémiques associées aux modèles de turbulence pour la fermeture des équations de Navier-Stokes moyennées à la Reynolds (RANS). Ces incertitudes découlent à la fois de l'inadéquation de la forme du modèle et d'une connaissance imparfaite des paramètres du modèle. Pour réaliser des prédictions robustes des écoulements en présence d'incertitudes de modèle RANS, et pour estimer et réduire les incertitudes sur la solution obtenue, nous étudions des techniques d'ensembles multi-modèles bayésiens et, plus spécifiquement, les mélanges bayésiens de modèles (BMA). Ce derniers utilisent un ensemble de modèles concurrents pour effectuer des prédictions distinctes d'un écoulement turbulent d'intérêt. Ces prédictions sont ensuite moyennées ensemble en utilisant leurs probabilités marginales a posteriori, et le mélange de modèles ainsi obtenu est utilisé pour estimer l'espérance et les intervalles de confiance des propriétés de l'écoulement. La première méthode étudiée, nommée Bayesian Model-Scenario Averaging (BMSA), étend la BMA pour prendre en compte l'incertitude dans le choix des configurations d'écoulement utilisées pour calibrer les paramètres du modèle. La deuxième méthode, nommée BMA spatiale (XBMA), produit des combinaisons de modèles dépendantes de l'espace en tirant parti des informations locales sur l'écoulement. Les deux méthodes possèdent de bonnes propriétés de généralisation lors de la prédiction d'un nouvel écoulement, tout en conservant l'avantage d'être non intrusives, faciles à mettre en œuvre, abordables en termes de coût de calcul et générales. Les exemples numériques portent sur la quantification et la réduction des incertitudes de modélisation de la turbulence pour des écoulements à travers une grille d'aubes de compresseur avec des conditions de fonctionnement variées.

Mots clés : Quantification d'incertitudes, modèles RANS, BMA, écoulements en turbomachines.

Abstract : Certification requirements and the constant pursuit of performance pushes aerospace manufacturers to thoroughly monitor the uncertainties inherent in their products. For this reason, Uncertainty Quantification (UQ) methods must now be integrated as early as possible in the design process, in order to guarantee reliability and performance. In this thesis, we focus on the numerical simulation of turbomachinery flows, and we present two methods for the quantification and reduction of epistemic uncertainties associated with turbulence closure models for the Reynolds Averaged Navier-Stokes (RANS) equations. These arise both from model-form inadequacy and from imperfect knowledge of model parameters. To make robust predictions under RANS model uncertainty, and to estimate and reduce uncertainties on the resulting solution, we investigate Bayesian multi-model ensembles techniques and, more specifically, Bayesian Model Averaging (BMA). This approach consists in using a set of competing model to make separate predictions of a turbulent flow of interest. Such predictions are then averaged together by using their posterior marginal probabilities, and the resulting model mixture is used to estimate expectancy and confidence intervals of the predicted flow properties. The first method, named Bayesian Model-Scenario Averaging (BMSA), extends BMA to account for the uncertainty in the choice of the flow configurations used to calibrate the model parameters. The second method, named space-dependent BMA (XBMA), produces space-dependent combinations of models by leveraging local information about the flow. Both methods demonstrate good generalization properties when predicting an unseen flow, while retaining the benefit of being non-intrusive, easy to implement, computationally affordable and general. Numerical examples focus on the quantification and reduction of turbulence modeling uncertainties for flows through a compressor cascade at various operating conditions.

Keywords : Uncertainty Quantification, RANS models, BMA, turbomachinery flows.